Understanding and Engineering Electronic and Optoelectronic Properties of 2D Materials and Their Interfaces

by
Youngwoo Son

B.S. Chemical Engineering, Seoul National University, 2010

Submitted to the Department of Chemical Engineering
in Partial Fulfillment of the Requirements for the Degree of

Doctor of Philosophy

at the

MASSACHUSETTS INSTITUTE OF TECHNOLOGY

September 2016

Signature redacted

Signature of Author: .....
Department of Chemical Engineering
June 8, 2016

Signature redacted

Certified by: .....
Michael S. Strano
Department of Chemical Engineering
Thesis Supervisor

Signature redacted

Accepted by: .....
Daniel Blankschtein
Herman P. Meissner (1929) Professor of Chemical Engineering, Graduate Officer
Committee for Graduate Students

Understanding and Engineering Electronic and Optoelectronic Properties of 2D Materials and Their Interfaces

By

Youngwoo Son

Submitted to the Department of Chemical Engineering
on June 8, 2016 in Partial Fulfillment of the Requirements for the Degree of
Doctor of Philosophy in Chemical Engineering

ABSTRACT

In the pursuit of further miniaturization beyond Moore's law, tremendous effort has been dedicated to exploring the potential of two-dimensional (2D) materials for nanoscale electronic devices. 2D materials are a group of solid state materials that possess strong in-plane covalent bonds while individual atomic layers are held together by weak van der Waals (vdW) interactions. Hence, their bulk crystals can be exfoliated into few-layer or even atomically thin single-layers via micro-mechanical exfoliation techniques. These materials possess unique and exotic properties due to quantum confinement of importance to future electronics. However, many technical problems need to be solved to realize this goal. For example, as 2D material-based devices become smaller down to the nanometer scale, the electrical contacts must also be reduced in scale which creates different characteristics from those of macroscopic counterparts. In addition, there are issues of reliability and stability with devices comprised of such materials. There is a need to understand the electronic and chemical properties of several interfaces that arise in such materials: metal-2D and 2D-2D junctions, for example. To this end, this thesis focuses on understanding nanoscale metal-2D semiconductor (SC) and 2D SC-2D SC junctions exploring: (1) electronic and optoelectronic behavior at the nanoscale junction of metal-MoS_2 and dependence on the layer number (thickness), (2) realization of voltage selectable photodiodes based on a lateral in-plane MoS_2-WSe_2 heterojunctions, and (3) interfacial properties and (opto)electronic characteristics of a phosphorene-MoS_2 vertical vdW p-n junction.

The first part of this thesis explores the layer number dependent electrical characteristics of the MoS_2–metal nanoscale junction using current imaging of MoS_2 nanosheets consisting of regions of varying different thicknesses using conductive and photoconductive spectral atomic force microscopy (C- and PCS-AFM). The layer number dependence of the effective barrier was measured, by obtaining consecutive current images while changing bias voltages, showing it to be linear. At the same time, spatially resolved two-dimensional (2D) maps of local electrical properties are generated from simultaneously recorded local current-voltage (IV) data. Furthermore, the layer number dependent spectral photoresponse of MoS_2 is investigated, which shows the highest response in single layer (1L) region. The photoresponse decreases for

increasing layer number, but increases again between 4L and 10L due to increased light absorption. The photoresponse is also strongly dependent on the wavelength of the incident light, showing much higher currents for photon energies that are above the optical bandgap. The photoresponse in forward and reverse biases shows barrier symmetry for 1L but asymmetry for 2, 3, and 4L, which further indicates a dominant role of the barrier on carrier transport at the junction.

The second part of this thesis investigates the spatially resolved transverse electrical properties of the monolayer WSe_2-MoS_2 lateral p-n heterostructures at their nanoscale junctions with metals both in the dark and under laser illumination. As in the first part of the thesis, C- and PCS-AFM, versatile tools to conveniently and efficiently interrogate layer-dependent electronic and optoelectronic characteristics in a MoS_2 crystal containing regions of different thicknesses, which enables direct characterization and comparison of the different layer regions without the complexities associated with fabricating and testing of different individual field-effect transistor devices, are used for measurements. By performing current imaging using a PtIr-coated conductive tip on an ultrathin nanosheet that includes homogeneous crystals of WSe_2 and MoS_2, and a lateral junction region in between, many thousands of WSe_2/MoS_2/the junction–metal contact points form during imaging and directly compare their local properties at the same time under identical experimental conditions with the nanoscale spatial resolution.

The third part of this thesis explores a new type of 2D vertical heterostructures that simultaneously possess desirable properties of constituent materials, paving the path for overcoming intrinsic shortcomings of each component material to be used as an active material in nanoelectronic devices. As a first example, a MoS_2-graphene vertical heterostructure is constructed and its charge transfer and photoluminescence (PL) at the interface are investigated. C-AFM and Raman spectroscopy show that there is a significant charge transfer between the two component materials. The PL intensity of monolayer MoS_2 is noticeably quenched when in contact with a single layered graphene in comparison to that of a bare monolayer MoS_2 crystal. Then, with the acquired understanding of the underlying physics at the 2D vdW heterointerfaces, the possibility of a black phosphorus (BP)-MoS_2 vertical heterostructure as an ultrathin channel material for high-performance 2D (opto)electronic devices is studied. CVD-synthesized MoS_2 and micromechanically exfoliated BP crystals are stacked together to form a vertical p-n heterostructure. Optical microscopy, AFM images, and Raman spectroscopy data show that the MoS_2 thin films can be used as a passivation layer, protecting BP from deteriorating in ambient conditions for extended period of time or under an elevated temperature in an Ar environment. The IV characteristics of FET devices based on the vertical heterostuctures exhibit that the MoS_2 layer has limited impact on superior carrier transport properties of the BP in the dark. Upon light illumination, photoconductivity of the BP-MoS_2 heterostructure region increased compared to that of the bare BP region of the same flake, mainly due to the fact that a built-in electric field formed at the BP-MoS_2 interface facilitates the dissociation of electron-hole pairs generated by light absorption.

Thesis Supervisor: Michael S. Strano
Title: Carbon P. Dubbs Professor of Chemical Engineering

Acknowledgements

It has been an incredible five-year journey that I will certainly miss and never forget. Now looking back, closing one of my biggest chapters of my life, I feel extremely blessed that I could spend my critical late twenties surrounded by countless talented, kind, and inspirational people, and that I get to have a chance to express my feelings of deep gratitude towards the following people in particular that have made every moment of this long and arduous journey enjoyable and fulfilling. Without a doubt, the completion of my thesis would not have been possible if it were not for their unconditional support and help.

First and foremost, I would like to thank my advisor, Professor Michael Strano, who has been the single most important person that enabled me to get through a number of difficulties I faced throughout this thesis work. It has long become a cliché in our research group to praise him for his enthusiasm and aspiration in the pursuit of science. I feel tremendously lucky that I have had a chance to learn firsthand the way he leads his research: Never to work on any problem just for the sake of another publication, but to strive incessantly for the new things nobody have ever thought of that can generate far-reaching impact not just inside the scientific community but in our everyday lives. I believe this is one of the greatest lessons he taught me; and whether I work as an academician or an engineer in industry in the future, I will undoubtedly be very successful if I deal with my life the way he does. Beyond as a research advisor he has been a great mentor, giving me enough discretion and waiting for me so I could ponder and come up with my own problems and ideas to solve them; and has always supported and encouraged me with invaluable advice even when the problems I proposed to work on were not as ambitious and creative as his ideas. Also, I remember the moments where he gave me high-fives over the data I showed him, which made me much more excited about what I was working on and gave me plenty of energy with which I could finish the best papers I could write. I will always be thankful for all of these and for allowing me to work in his lab over the course of my graduate studies.

I also thank my committee members, Professor William Tisdale and Professor Tomas Palacios. I feel privileged to be advised by two of the brightest young rising stars at the institute who have always provided me with their critical but constructive insights and suggestions, which have absolutely been a big help in completing my thesis in a much better shape. Though my annual thesis committee meetings never went smoothly because of their incessant sharp and keen questions, those were precious experiences that have made me become tougher-minded engineer ready to jump into an increasingly competitive professional world.

In addition to my committee members, I should definitely express my thanks to the entire SRG lab mates for their support and help both experimentally and, more importantly, emotionally. It was very fortunate that I could have an opportunity to interact with the most talented and kind people from various parts of the globe. Specifically, I would like to give special thanks to

Professor Qing Hua Wang, Professor Chih-Jen Shih, and Professor Kyungsuk Yum who were collaborators and friends who had the most significant impact on the earlier part of my days in the SRG. Qing Hua taught me everything from how to write a research paper to all the experimental techniques that have been a central part in building my thesis. Chih-Jen provided me with his immense knowledge in 2D electronics as well as useful advice that had me keep sight of a bigger picture so I could build the story of my thesis. Kyungsuk spared no efforts to help me settle down in the group and adapt well to the new surroundings.

Finally, I would like to show my thanks to dear friends of mine I met here in Cambridge and my family who have given me endless support that kept me going during the toughest times I have ever experienced. I thank all KSACE members for all the unforgettable moments we shared that I will certainly miss. Especially, I want to give special thanks to my classmates, Jiyoung Ahn and Siwon Choi, who shared not only our highest but also lowest moments supporting each other. I could not have gotten through the notoriously tough ChemE first year and qualifying exams if it were not for their help. Also, my roommates, Dr. Mansoo Park and Dr. Donghun Kim, as well as Dr. Gwanhong Lee and Daniel J. Kim have made MIT, otherwise would have been only a demanding and tedious place, an extremely fun place full of enjoyment and excitement. I wholeheartedly appreciate that and will never forget the fun times we have shared not only here in Cambridge but also in New York, Paris, and Amsterdam. However, above all, I must express my deepest gratitude to my family, my parents and my older brother, Gangdeok, for their endless love and support. They have always been concerned not about my publications or test scores but only about my health and emotional well-being. In good times or bad, they have been always there for me, being proud of me, whereby I was able to finish this thesis. I am so grateful for that and do only hope that I will be able to make up for even a fraction of the love they have given me in my lifetime.

Table of Contents

List of Figures

Figure 3-2: (a) Cartoon of a cross section of MoS_2/C_{60} sample on ITO/glass substrate. (b) AFM topography (c) and corresponding PCS-AFM using Pt/Ir coated tip, at 8V with alternating laser illumination (λ=700nm).

Figure 3-3: Nanoscale visualization of local photo response to different excitation laser wavelengths normalized by laser intensity.

Figure 3-4: (a) Schematic illustration of the contact between the conductive tip and MoS_2 flake surface. (b) Representative force-displacement (*F-D*) curve.

Figure 3-5: A schematic of the photoconductive spectral atomic force microscope (PCS-AFM) instrument.

Figure 3-6: (a) An optical microscope image of a flake of MoS_2 on ITO/glass substrate. (b) Raman spectrum for MoS_2 sample in (a). (c) A spatially resolved Raman map of the frequency.

Figure 3-7: (a)-(c) Current images in reverse bias (a) and forward sample bias (b)-(c) taken by changing the applied sample voltage within the horizontal strips. (d) A current–voltage (*I-V*) curve generated by taking average current values for each bias voltage from the current images.

Figure 3-8: A schematic band diagram of a thin MoS_2–metal tip junction in equilibrium (left panel) and under reverse (middle) and forward (right) sample bias voltages.

Figure 3-9: A semilogarithmic plot of bias voltage as a function of log (current).

Figure 3-10: (a) An optical microscope image of an exfoliated sheet of MoS_2 on ITO/glass substrate consisting of 1-, 2-, 3- and 4-layer regions. (b) A lateral force microscopy (LFM) image for better visualization of the flake shape. (c) Raman map of frequency difference. (d) Representative Raman spectra taken at each thickness region.

Figure 3-11: Current maps generated by conductive AFM measurements in the dark under varying applied sample bias voltages.

Figure 3-12: Additional Raman characterization, optical and C-AFM images in the dark.

Figure 3-13: Averaged *I-V* data from regions of MoS_2 that are 1L, 2L, 3L, 4L, 12L, and 20L thick.

Figure 3-14: A plot of barrier heights as a function of MoS_2 layer number.

Figure 3-15: (a) A plot of the tunneling barrier ($\Phi_B^{3/2}d$) extracted using the FN tunneling model as a function of MoS_2 layer number *n*. (b) Spatially resolved map of local tunneling barrier, $\Phi_B^{3/2}d$, obtained from local *I-V* data recorded.

Figure 3-16: Spectral photoresponse in MoS_2 as a function of layer number.

Figure 3-17: Current images under illumination of varying wavelengths.

Figure 3-18: Additional Raman characterization, optical and C-AFM/PCS-AFM.

Figure 3-19: Spectral photoresponse in MoS_2 as a function of layer number.

Figure 3-20: Plot of photoresponse as a function of MoS_2 layer number generated from the both samples where red and blue data points are extracted from samples in Figure 3-16 (a) and (h), respectively.

Figure 5-1: (a) Optical microscope image, and (b) topographical diagram for a CVD graphene-coated MoS_2 single crystal. (c) AFM topographical height and (d) current profiles using our c-AFM system.

Figure 5-2: Spatial Raman maps for (a) I_{2D}/I_G, (b) ω_G, and (c) the calculated ($E_{Dirac} - E_F$) for the MoS_2–graphene heterostructure considered.

Figure 5-3: (a) Representative PL spectra for the regions of monolayer MoS2 with (red) and without (blue) graphene on top. (b) Spatial PL intensity map for the MoS_2–graphene heterostructure considered.

Figure 5-4: (a) Schematic illustration of BP-MoS_2 vertical heterostructure fabrication process. (b) Optical images taken after the dry transfer of MoS_2 (left), and metal electrodes deposition (right).

Figure 5-5: (a) Schematic illustration of the BP-MoS_2 heterostructure on a SiO_2 (100nm)/Si substrate. (b) Optical microscope image of a BP-MoS_2 heterostructure. (c) AFM height profile of the 2L BP crystal taken along the red line marked in (b). (d) Representative Raman spectra.

Figure 5-6: Representative PL spectra of the exposed (black) and MoS_2-passivated (red) BP.

Figure 5-7: Optical images of a BP-MoS_2 heterostacks acquired upon fabrication (a), after 1 (b) and 3 weeks of exposure to air (c).

Figure 5-8: Representative Raman spectra taken at exposed (bottom) and MoS_2-passivated BP (top) upon preparation and in 3 weeks in air.

Figure 5-9: (a) Optical images of a BP-MoS_2 heterostacks acquired upon fabrication (left) and after annealing under Ar environment at 350°C for 2 hours (right). (b) Representative Raman spectra taken at exposed (bottom) and MoS_2-passivated BP (top) upon preparation and the annealing.

Figure 5-10: Schematic illustration of the FET devices (left) and an optical image of the 13 nm device (right).

Figure 5-11: Transfer characteristics of the MoS_2-passivated BP channels of varying thicknesses.

Figure 5-12: Detailed transport characteristics of the 2L device.

Figure 5-13: A simplified resistor network model that represents carrier transport pathways in the BP-MoS_2 region.

Figure 5-14: Band diagrams under different external conditions: carrier transport in the dark when (i) $V_g > 0$ and (ii) $V_g < 0$

Figure 5-15: Transfer characteristics of the 5, 13, and 20 nm devices.

Figure 5-16: Thickness-dependent photoresponse of the BP-MoS_2 devices.

Figure 5-17: Band diagrams under different external conditions: (i) upon illumination with $V_g < 0$; (ii) conceptual explanation of the observed photo-induced doping effect.

List of Tables

1. Overview

This thesis describes the understanding and engineering of electronic and optoelectronic properties of 2D semiconductor (SC) materials at their interfaces with metals and dissimilar 2D SC layers. The first half part of this thesis focuses on experimental investigations into characteristics of nanoscale metal-2D SC junctions. The latter half of the thesis explores different combinations of 2D SC-2D SC interfaces where charge transfer and formation of an energy barrier can be further exploited to shed light on the development of next-generation ultrathin transparent nanoelectronic devices.

With the advent of experimental isolation of graphene, a tremendous amount of attention has been given to its potential as an active material in nanoelectronic devices due to its unique and remarkable mechanical and electronic properties. However, because of its limitation originating from graphene's gapless, semimetal nature, its adoption as an active channel material in nanoelectronic application has not come to its fruition yet. As an alternative, novel inorganic semiconducting 2D materials—including from transition metal dichalcogenides (TMDs) and, very recently, black phosphorus (BP)—have been risen to a primary focus of the 2D materials community. One of the exquisite features of these materials is the layer number dependence of their electronic and optoelectronic characteristics which arises from quantum confinement.

In chapter 3 of this thesis I describe the layer number dependent electronic and optoelectronic characteristics of the MoS_2–metal nanoscale junction *via* current imaging of MoS_2 nanosheets consisting of regions of varying different thicknesses (1, 2, 3, and 4-layers) using conductive and photoconductive spectral atomic force microscopy (C- and PCS-AFM). The experimental results reveal that the effective Schottky barrier that forms at the junction is dependent upon the layer number of MoS_2. The layer number dependent spectral photoresponse of MoS_2 is also investigated, which shows the highest response in single layer (1L) region. This layer number dependent photoresponse is explained by the competition between carrier collection efficiency, which is determined by carrier transport through the junction, and the amount of light absorption.

In order to validate the assumption made in the data interpretation that the Schottky barrier plays a significant role in carrier transport through the junction, conductive imaging using the identical metal tip on dissimilar 2D SC crystals—with the same thickness but with quite different work function levels so that the energy barriers take quite different form accordingly—can be utilized. One of the advantages of the experimental technique exploited in chapter 3 is, by imaging a crystal consisting of multiple layer thicknesses that can fit within a single image, layer dependent properties can be measured under the same experimental conditions. In chapter 4, I provide the C- and PCS-AFM imaging results performed on a monolayer WSe_2-MoS_2 in-plane heterostructure, where WSe_2 is p-type SC and MoS_2 n-type. As the heterostructure fits within a single AFM image an accurate comparison between WSe_2-metal and MoS_2-metal junctions can be made using the identical experimental conditions. Despite the fact that charge carriers experience the resistance of an atomically thin layer of almost the same thickness (~0.7 nm), an opposite IV trend is observed from WSe_2 and MoS_2, corroborating the interpretation of the carrier transport mechanism proposed in previous chapter. Furthermore, this finding is further exploited to demonstrate a hyper-resolution array of the switchable photodiode pixels, which can be selectively switched on and off by modulating the polarity and magnitude of the applied voltage.

In chapter 5 of this thesis, I study fascinating phenomena, including charge transfer, change of photoluminescence (PL) intensity, and charge carrier transport modulation, that occur at the interface between MoS_2 and graphene. Because of the limitations each 2D material has, it has recently become one of the central focus of the 2D materials community to understand and discover a suited combination of different 2D crystals for specific target applications to compliment weakness of each other and generate a significant synergy effect. C-AFM and Raman spectroscopy are used to show that there is a noticeable charge transfer at the interface. The built-in electric field generated due to the different work functions levels of the component layers leads to the quenching of the PL intensity of a monolayer MoS_2. With this understanding of underlying physics at 2D interfaces, I fabricate field-effect transistor (FET) devices out of the MoS_2–graphene vertical heterojunction that changes their operation types, from NMOS digital to bipolar regimes, upon the modulation of gate and drain bias voltages. Further, I investigate MoS_2-BP vertical van der Waals heterostructures. BP, which typically

shows a p-type characteristic, has lately been garnering an enormous amount of attention thanks to its superior electronic characteristics to TMDCs as well as the direct band gap feature regardless of its thickness. However, BP degrades fairly quickly upon exposure to air, which inhibits its prompt adoption in nanoelectronic applications. I demonstrate that MoS_2 can act as a passivation layer, providing a great protection to BP from degradation, as well as an n-type component of a van der Waals p-n interface that boosts photoresponse of BP photodetectors based on FET device architecture.

In summary, this thesis clearly outlines insights into underlying physics at the important metal-2D SC and 2D SC-2D SC interfaces, and a new experimental technique to accurately and efficiently investigate the potential of this new class of junctions in future nanoelectronics. These results should provide critical information to design and engineer electronic and optoelectronic devices based on quantum confined 2D lateral heterostructures at the nanoscale level.

2. Introduction

Although layered materials have been known in the scientific community for more than 150 years, it was only recently that we have begun to appreciate their enormous potential in atomically thin nanoelectronic applications after the seminar work by two Nobel Laureates, Novoselov and Geim in 2004.[1] The micromechanical exfoliation technique introduced in the paper has provided researchers with a powerful tool that makes the physical limit of these materials—referred to as 2D materials due to their one-atomic-thin nature—readily accessible, giving rise to an explosion of follow-up research from all over the globe. One of the main features that have brought about the tremendous amount of attention is the fact that these layered materials exhibit novel and exquisite properties when thinned down to its ultimate physical limit, which are distinct from that of their bulk counterpart. The most well-known and widely-studied material by far is graphene due to its exceptional electronic, chemical, and mechanical properties. Afterwards, various kinds of 2D materials, ranging from an insulator (hexagonal boron nitride, hBN) to semiconductors (TMDCs, BP, etc.), have also been discovered and thoroughly investigated.[2] A significant advantage these 2D

materials hold over traditional silicon is not only their potential towards drastic miniaturization of electronic devices but the possibility of the realization of flexible and transparent future electronic devices.

2.1 Overview of 2D Materials

In their bulk form, 2D materials exist as stacks of strongly bonded layers—by in-plane chemical bonds—with weak interlayer, van der Waals (vdW) attraction, thereby allowing for exfoliation into the physical limit of a single layer form.[3] Most of the earliest research efforts have been concentrated on graphene, sparked by the pioneering work from Novoselov and Geim in which they demonstrated that exfoliation of graphite into single-layered graphene sheet could easily be performed using an adhesive tape, and experimentally showed the exquisite electronic characteristics of graphene by fabricating field-effect transistors (FETs).[1] Following graphene, theoretical work showed that hBN could induce a bandgap in graphene when graphene was deposited on top of it;[5] and an increase amount of experimental research suggested that hBN may act as an ideally-suited substrate for graphene nanoelectronics.[6] The scope of the 2D materials research has ever expanded to reveal that an inorganic 2D materials family, TMDCs, shows layer number dependent electronic and optical characteristics when thinned down to single- or few-layered forms.[7] Further device fabrication for various electronic and optoelectronic applications ignited an exponential interest in the 2D nanoelectronics community,[8] causing for TMDCs to be now a primary focus of a number of researchers, as evidenced by the number of publications dedicated to this class of materials (Figure 2-1). In addition, there are many layered materials other than TMDs, such as monochalcogenides (GaSe, etc.), and mono-elemental 2D semiconductors (silicene, phosphorene, germanene) (Figure 2-1). One great advantage lies in this diversity of 2D materials with a wide spectrum of materials properties: TMDCs possess metallic, semimetallic, or semiconducting characteristics depending on the coordination and oxidation state of the metal atoms; superconductivity or charge-density wave effects when specific conditions are imposed.[3] Thus, the significant potential of these layered materials may emerge from developing interfaces with any desired combinations among them, creating

novel 3-dimensional (3D) heterostructures with entirely new material properties. Along with these remarkable and extraordinary advances in 2D materials research, much of efforts also have to be devoted to controlling defects, understanding the impact of substrate, and developing means for controlled doping to ultimately realize the wide usage of 2D materials in future technologies.

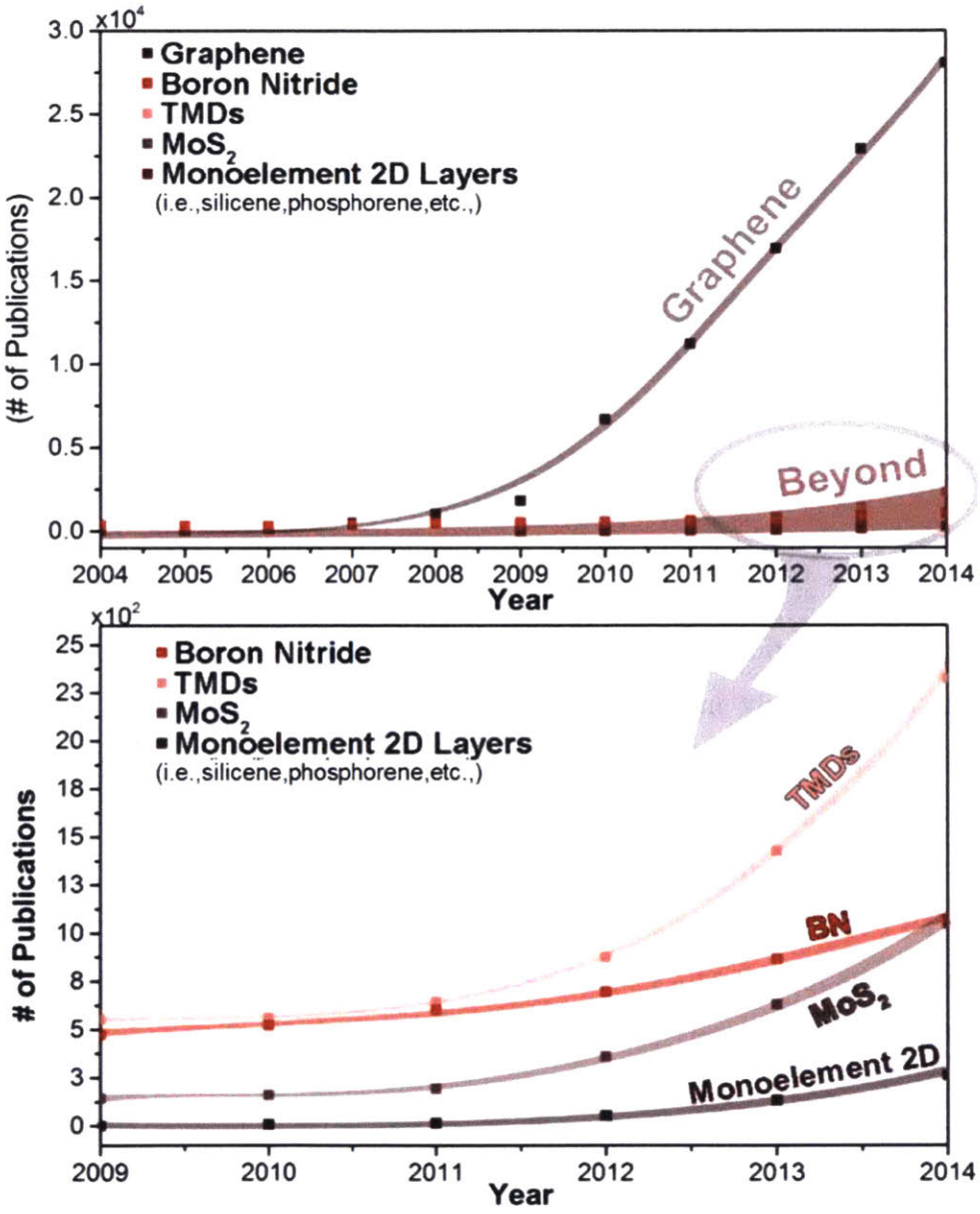

Figure 2-1: Publication trends in 2D materials beyond graphene. Source: Web of Science. Search index: [Title search (x) or title (y) and topic (z), where x = graphene or boron nitride

or transition metal chalcogenides or molybdenum disulfide or monoelements (silicene, germanene, phosphorene, stanene or borophene), y = graphene or BN or TMDs or MoS_2) and z = graphene or boron nitride or transition metal chalcogenides (TMDs: MoS_2, WS_2, $MoSe_2$, WSe_2, TaS_2, $TaSe_2$, NbS_2) or MoS_2 or monoelement 2D: silicene, germanene, stanene, borophene, phosphorene.] Image from Ref[2]

2.2 2D Layered Materials Explored in This Thesis

In this section, a brief introduction to unique properties and their synthetic methods of a few different 2D layered materials explored throughout this thesis will be provided: molybdenum disulfide (section 2.2.1), graphene (section 2.2.2), and black phosphorus (section 2.2.3)

2.2.1 Molybdenum Disulfide (MoS_2)

Among more than 40 different TMDCs—a family of materials that possess the chemical formula MX_2, where M represents a transition metal element (Ti, Zr, Hf, V, Nb or Ta, etc.) and X chalcogen atoms (S, Se, or Te)—Molybdenum disulfide (MoS_2) has been received by far the most attention from the community. MoS_2 is relatively unreactive inorganic compound, not readily influenced by oxygen and dilute acids under ambient conditions. Similar to graphite, molybdenum disulfide exists in bulk form as stacks of strongly bonded layers with weak interlayer vdW attraction, thereby widely used as a solid lubricant owing to its low friction properties and robustness. Due to its weak out-of-plane interactions the bulk crystal can be exfoliated into 2D layers of single unit cell thickness, which form layered structures of the form S-Mo-S, with the sulfur atoms in two hexagonal planes separated by a plane of molybdenum atoms, as shown in Figure 2-2.

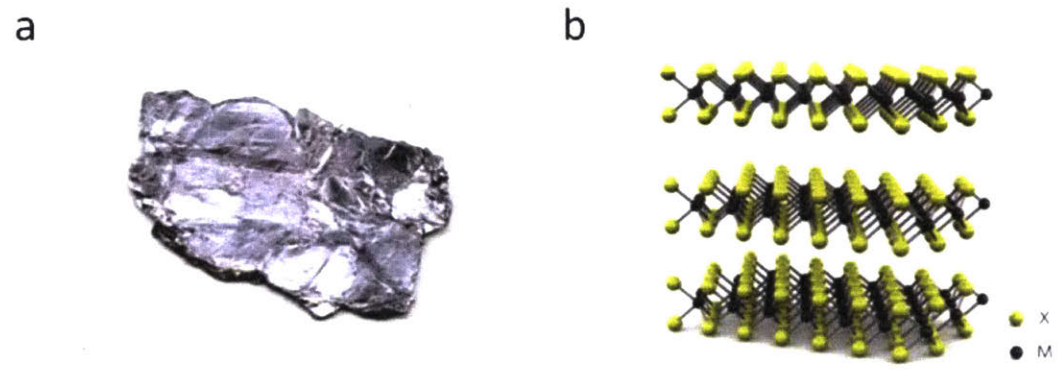

Figure 2-2: Structure of molybdenum disulfide. (a) Photograph of bulk MoS_2 crystal. (b) Three-dimensional schematic representation of a typical MoS_2 structure, with sulfur atoms in yellow and the molybdenum atoms in grey. Image from Ref[4]

Electronic band structures for bulk and single layer MoS_2 are calculated from first principles density functional theory (DFT), as shown in Figure 2-3:[5] the momentum of the minimum energy state of the conduction and the maximum state of the valence band differs from each other in bulk MoS_2; when the material is thinned down to the monolayer its band structure changes allowing the direct excitonic transitions at the K-point in the Brillouin zone, whereas, for its bulk form, the band gap transition is indirect at the Γ-point that corresponds with the origin of the Brillouin zone. The change in the band structure with the number of layers is mainly due to quantum confinement and the subsequent hybridization change in p_z orbitals on S and d orbitals on Mo atoms.[6] In addition, according to DFT calculations, the states in conduction band at the K-point is comparatively unaffected by interlayer coupling because of the fact that they mainly stem from localized *d* orbitals of Mo atoms; but the states near the Γ-point exhibit a rather strong interlayer coupling as the p_z orbitals of S atoms and the *d* orbitals on Mo atoms are involved. Thus, as the layer number decreases the states near the Γ-point show noticeable shifts while that near the K-point remain unaltered.[7]

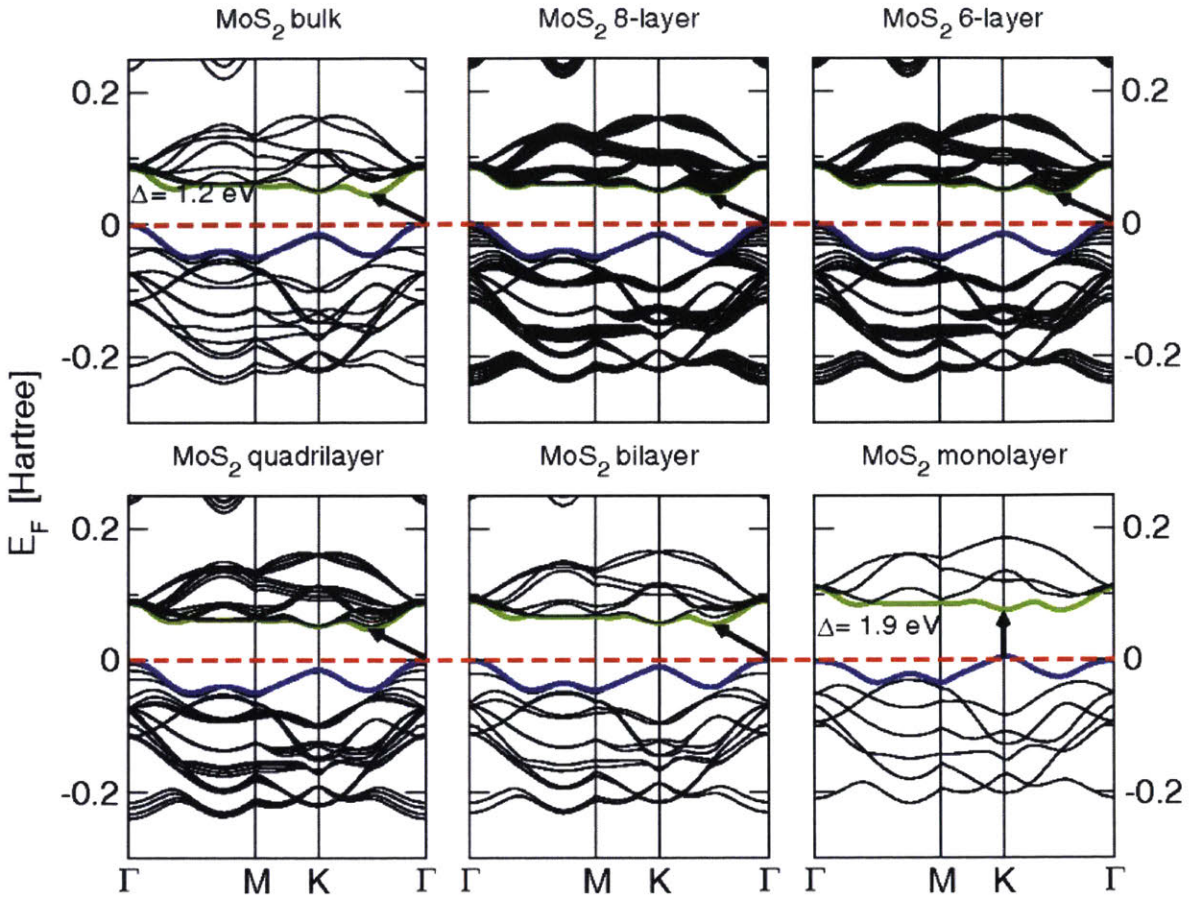

Figure 2-3: Electronic band structure of MoS_2 in terms of its layer number, calculated at the DFT/PBE level. The red horizontal dashed lines indicate the Fermi level. The green and blue lines highlight the bottom of conduction band and the top of valence band, respectively. Image from Ref[5]

The possibility of tuning the band structures by controlling the thickness of MoS_2 flakes makes this material highly attractive for many applications. In particular, the 1.2 eV band gap in the bulk form is comparable to that of silicon (1.1 eV) suggesting the opportunity of MoS_2 being utilized as an active channel material for digital FET devices (Figure 2-4). And achieving a direct band gap characteristic in its monolayer form makes it more desirable in various optoelectronic applications such as photodetectors and photovoltaic devices. Thus, this thesis includes the synthesis of layer number-controlled large area MoS_2 thin films via chemical vapor deposition (CVD) process in order for the material to be used in specific purposes.

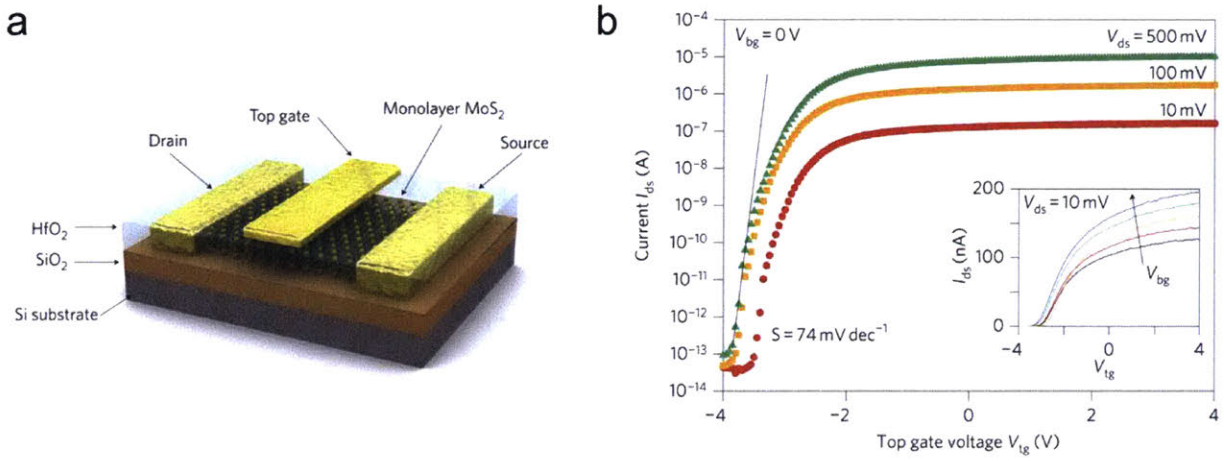

Figure 2-4: Single layer MoS_2 transistor. (a) Schematic of the top gate FET device. (b) Recorded drain-source current (I_{DS}) in regards to top-gate voltage (V_{TG}) ranging from 10 mV to 500 mV. Image from Ref[4]

2.2.2 Graphene

2D Graphene is one-atom thick planar sp^2-bonded carbon atoms constructed in a hexagonal crystal lattice, which can be the building block for other carbon materials of other dimensionalities including C_{60} (0D), single-walled carbon nanotubes (or SWNT, 1D), and graphite (3D), as illustrated in Figure 2-5. While theoretical studies of graphene have been conducted for more than fifty years, this 2D crystal sheet was believed to be thermodynamically unstable to exist in an isolated form. Upon the experimental demonstration of free-standing graphene and the discovery of its remarkable mechanical, electrical, and optical properties including the fact that quasiparticles in graphene are massless Dirac fermions, the material has experienced an explosion of attention from the research community and follow-up research, which eventually resulted in the Nobel Prize in Physics in 2010.[8]

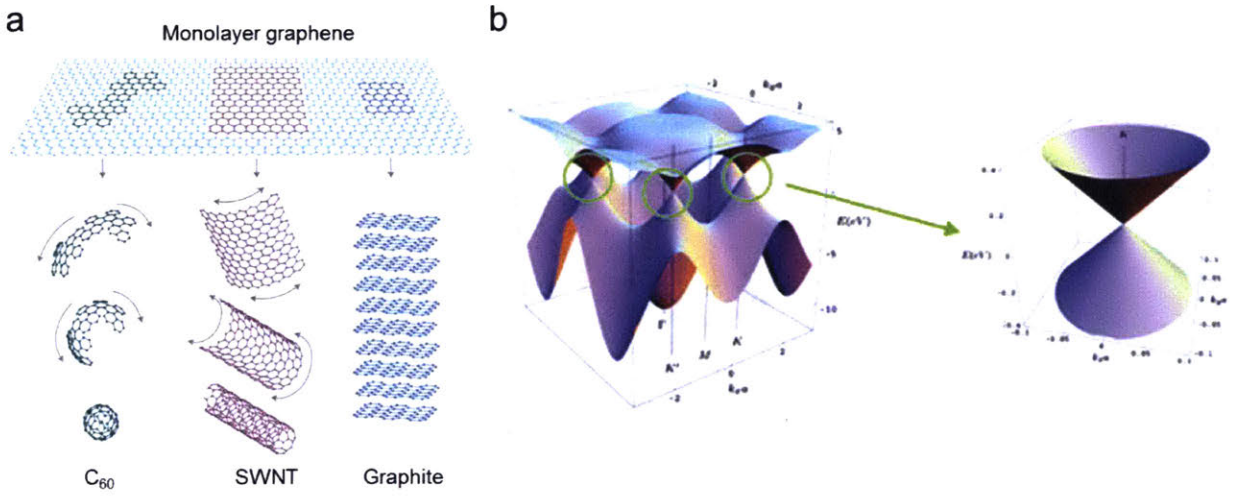

Figure 2-5: Crystal structure and electronic band structure of graphene. (a) A hexagonal crystal lattice of graphene can be wrapped to form a 0D C_{60} or rolled up to form a 1D SWNT. (b) 3D representation of the electronic density of states showing the conduction and valence band cones meet at a single point, in the enlarged panel on the right side. Image from Ref[9, 10]

Thermodynamically, it shows substantially dissimilar properties compared to its bulk form; and from an electronic point of view, it is a semimetal (or a gapless semiconductor) as the conduction and valence band touch each other at six points (K-point) of the Brillouin zone—associated with the Dirac poin—as shown in Figure 2-5 (b), thereby allowing few electronic states near the Fermi level.[10] In Figure 2-6, recorded transfer characteristics of a graphene FET show that, when no electrostatic doping is applied, the Fermi level locates at the Dirac point where no electronic density of states is expected to exist for charge carrier transport. The symmetry observed around this charge neutrality point is due to the linear and symmetric energy-momentum (*E-k*) dispersion around the Dirac point, giving rise to ambipolar transport characteristics. The electron mobility can reach as high as ~ 25,000 $cm^2/(V \cdot s)$ for suspended graphene, ~ 1,000,000 $cm^2/(V \cdot s)$ for graphene supported on hBN, and ~10,000 $cm^2/(V \cdot s)$ for SiO_2.[11, 12]

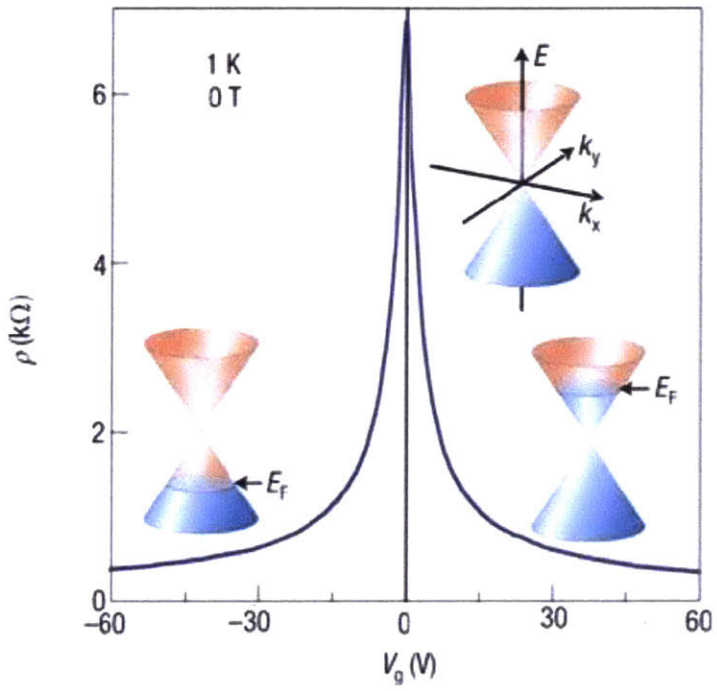

Figure 2-6: Transfer characteristics of graphene FETs showing a symmetric and ambipolar characteristic around the charge neutrality point. Insets illustrate changes of the Fermi level position according to the applied gate voltage. Image from Ref[9]

2.2.3 Black Phosphorus (Phosphorene)

The bulk form of black phosphorus (BP), the most stable allotrope of the phosphorus element, was first synthesized more than a century ago,[13] but it is only recently that it started regaining enormous attention from a wide variety of research fields in the context of a 2D layered material. BP is a single-elemental layered crystalline material, like graphene, consisting of only phosphorus atoms, which possess three crystalline structures—orthorhombic, simple cubic, and rhombohedral. But among the crystalline structures it is the puckered orthorhombic BP that has attracted the most attention because of its semiconducting characteristic, as schematically illustrated in Figure 2-7. Two atomic phosphorus layers form a single layer of BP wherein two kinds of P-P bonds exist: The shorter bond (0.2224 nm) is connected to the nearest P atoms on the same plane, while the longer bond (0.2244 nm) bonds P atoms located on the two atomic layers of a single layer.

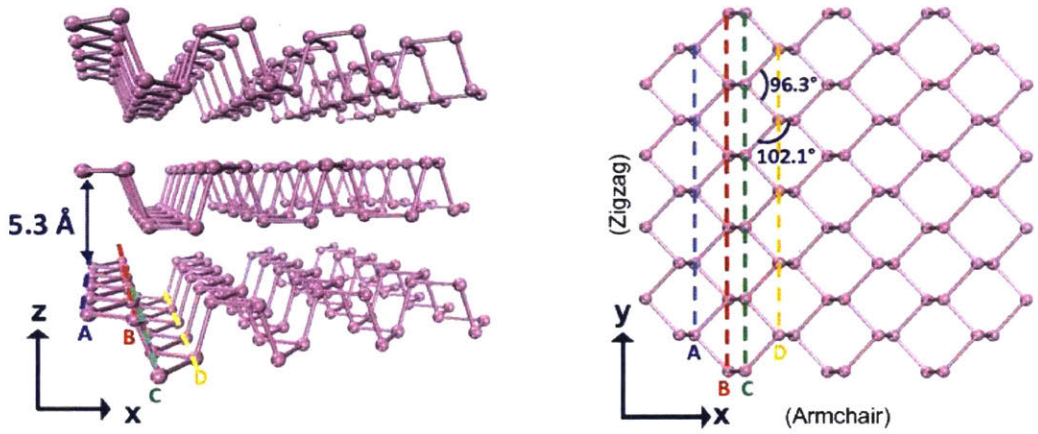

Figure 2-7: Schematic crystal structure of BP. Left panel illustrates a side view of the crystal lattice; Right panel shows a top view. The lattice spacing is 5.3 Å. Image from Ref[14]

First and foremost, one of the fascinating characteristics of BP that excited a number of researchers in nanoelectronics and nanooptoelectronics is the possibility of band gap engineering over a wide range of energy spectrum by controlling the number of layers or strain applied:[15] First principles calculations showed that band gap of single- or few-layer BP is expected to vary from above 2.0 eV in its single layer form down to around 0.3 eV when the crystal thickness is around 4 nm (~8 layers) and thicker, bridging the energy gap between graphene and TMDCs (Figure 2-8). What makes this feature more intriguing is the direct band gap character is maintained regardless of thickness—TMDCs shows the direct gap character only in their monolayer form—which most of optoelectronic applications find valuable. Moreover, strain, both tensile and compressive, results in a noticeable change in the BP electronic band structures in its single- and few-layer forms.[16] Thus, BP interacts strongly with electromagnetic waves over covers a broad energy spectrum—in the visible and mid- to near-IR frequency range—the feature that various applications such as thermal imaging, thermoelectric, telecommunication, and photovoltaics can exploit.

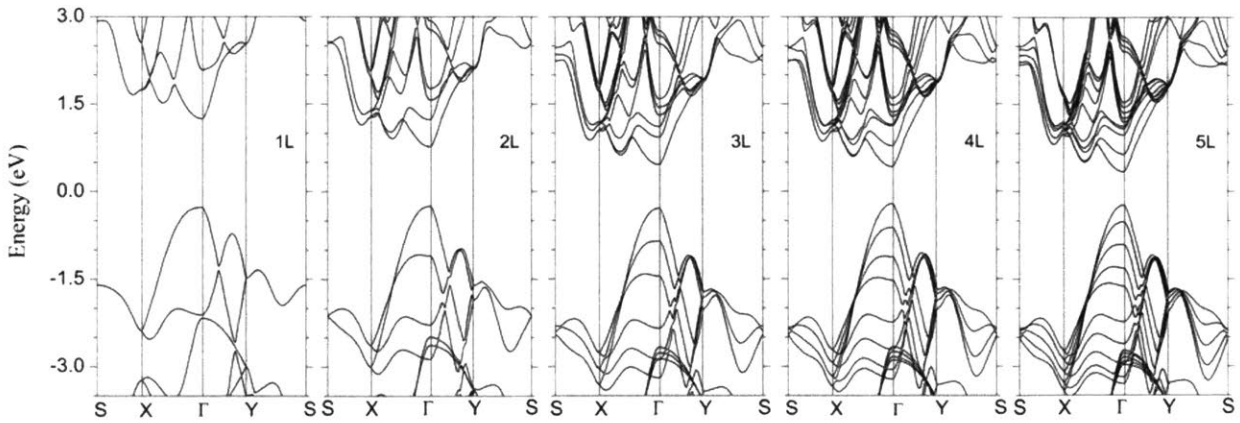

Figure 2-8: Calculated electronic band structures for 1-5 layer BP crystals. Note that the direct band gap character is expected regardless of the layer number which renders BP more beneficial for various optoelectronic applications. Image from Ref[15]

Taking advantage of all the expertise accumulated in advance in the 2D materials research community with graphene and TMDCs, a number of sophisticated, advanced nanoscale devices have quickly been fabricated out of BP and characterized in all sorts of different ways to test its potential as an active material in various domains of nanoscale electronics and optoelectronics. The transport characteristics of a 5-nm-thick BP field-effect transistor (FET) back-gated device fabricated on a silicon substrate with 90 nm SiO_2 at room temperature is shown in Figure 2-9,[17] in which the device exhibits an ambipolar characteristic (a slight turn-on on the electron side is observed), whereas Kim et al.[18] have reported that BP FETs show a characteristic p-type behavior without a passivation layer on top of it. The devices reported so far have shown that their hole mobility can reach up to more than 1,000 $cm^2V^{-1}s^{-2}$ at 300 K while current on-off ratios in the range of 10^2-10^4,[17, 19, 20] which are key features for devices constituting high-speed logic circuits. From the overall device performance perspective, 4-10-nm-thick BP crystals may provide the most desirable trade-offs between carrier mobility and current on-off ratio for developing nanodevices that operate in the multi-gigahertz frequency range and beyond.

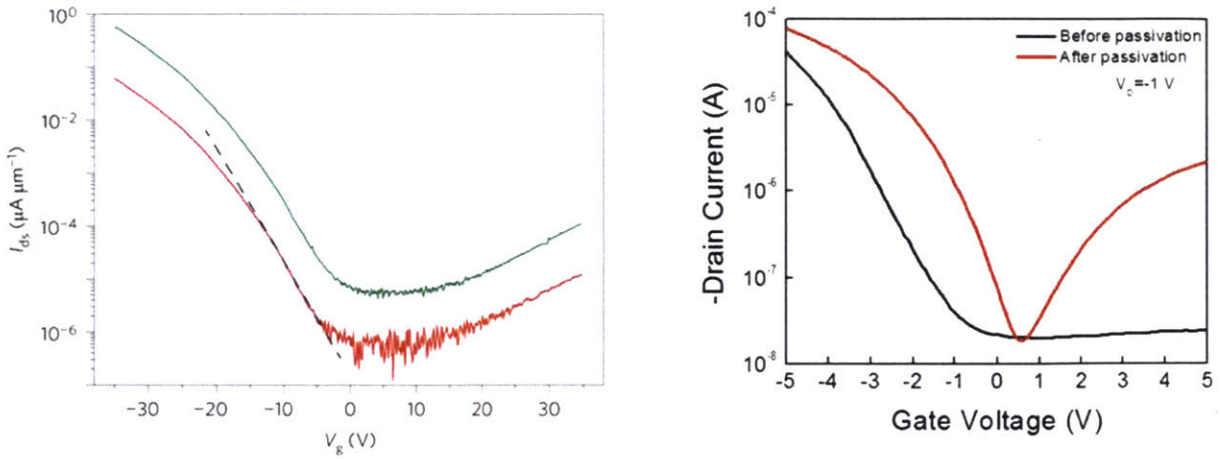

Figure 2-9: Transport characteristics of few-layer BP FETs. Left panel: a 5-nm-thick BP device that shows an ambipolar behavior though p-type characteristic is more significant. Image from Ref[17] Right panel: before Al_2O_3 passivation, the device exhibits characteristic p-type behavior. Image from Ref[15]

In addition to these advantageous device performances compared with graphene and TMDC devices, the in-plane anisotropy of BP that stems from its puckered orthorhombic crystal structure may offer another interesting degree of freedom in developing a new type of nanodevices that cannot be possible with other 2D materials discovered so far.[21, 22] The effective mass of charge carriers along the zigzag direction is ~10 times heavier than along the armchair direction, resulting in noticeable anisotropy in its intrinsic optical, phonon, and electronic properties, as shown in Figure 2-10.[21, 22]

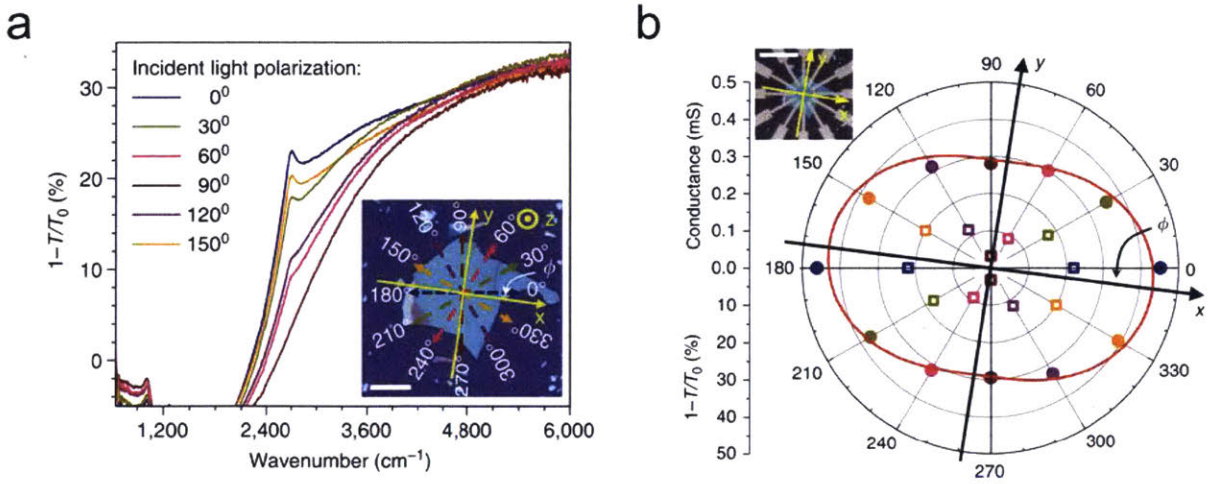

Figure 2-10: In-plane anisotropy of BP crystals. (a) Polarization-resolved infrared relative extinction spectra with the light illumination polarized along the six directions noted in the inset. (b) DC conductivity and IR relative extinction recorded with respect to the same six angles as (a) on the same BP crystal. Image from Ref[21]

A major challenge that needs to be overcome for BP crystals to realize its potential to the fullest is instability when exposed to the water and air: single- or few-layer BP crystals suffer severe degradation within a matter of hours while bulk BP crystals may remain relatively stable under ambient conditions for up to several months.[23] XPS characterization and FT-IR measurements performed by Wood et al. revealed that the crystal degradation originates from the formation of the oxidized phosphorus species.[24] But when passivated by Al_2O_3 on top, the BP crystals are shown to be relatively stable for weeks in an ambient condition.

2.3 Synthetic Methods for 2D Materials

Here, the basics of the three major synthetic routes will be introduced: micromechanical exfoliation (the scotch-tape method, section 2.3.1) for high quality crystals, liquid phase exfoliation (section 2.3.2) for large quantity production, and chemical vapor deposition process (section 2.3.3) for large area, thickness controlled synthesis.

2.3.1 Micromechanical Exfoliation

Micromechanical exfoliation, also well-known as the scotch-tape method, is the easiest way to obtain 2D materials in their single- or few-layer forms. The exfoliation is performed by mechanically peeling off the layers of the parent bulk materials, yielding few-layer-thick thin films to the ultimate limit of single-layered 2D crystalline flakes while retaining the intrinsic crystal structure and properties. When the adhesion of the bottom layer (the layer in touch with the substrate) to the target substrate is sufficiently strong to overcome the interlayer interactions, a layer of 2D material can be transferred onto the substrate, producing extremely high-quality 2D crystals. This mechanism suggests that when the 2D material considered has a stronger interlayer interaction (or higher surface tension), it becomes more difficult to

obtain monolayer sheets using this method. Consequently, monolayer MoS2 sheets are generally more difficult to be obtained than graphene sheets using the Scotch-tape method. This process is enabled by strong interaction between the bottommost layer of the material and the target substrate, which overcome that between interlayers and gives rise to transfer of atomically thin 2D flakes. Thus, the success rate of this method hinges on the competition between the two interactions, which varies from material to material in consideration.

While this method has contributed considerably to numerous scientific studies of 2D materials that explore their intrinsic properties, it has its limits in that it is not only scalable and suitable for mass production on a larger industrial scale, but almost impossible to control thickness or size of the flakes on demand.

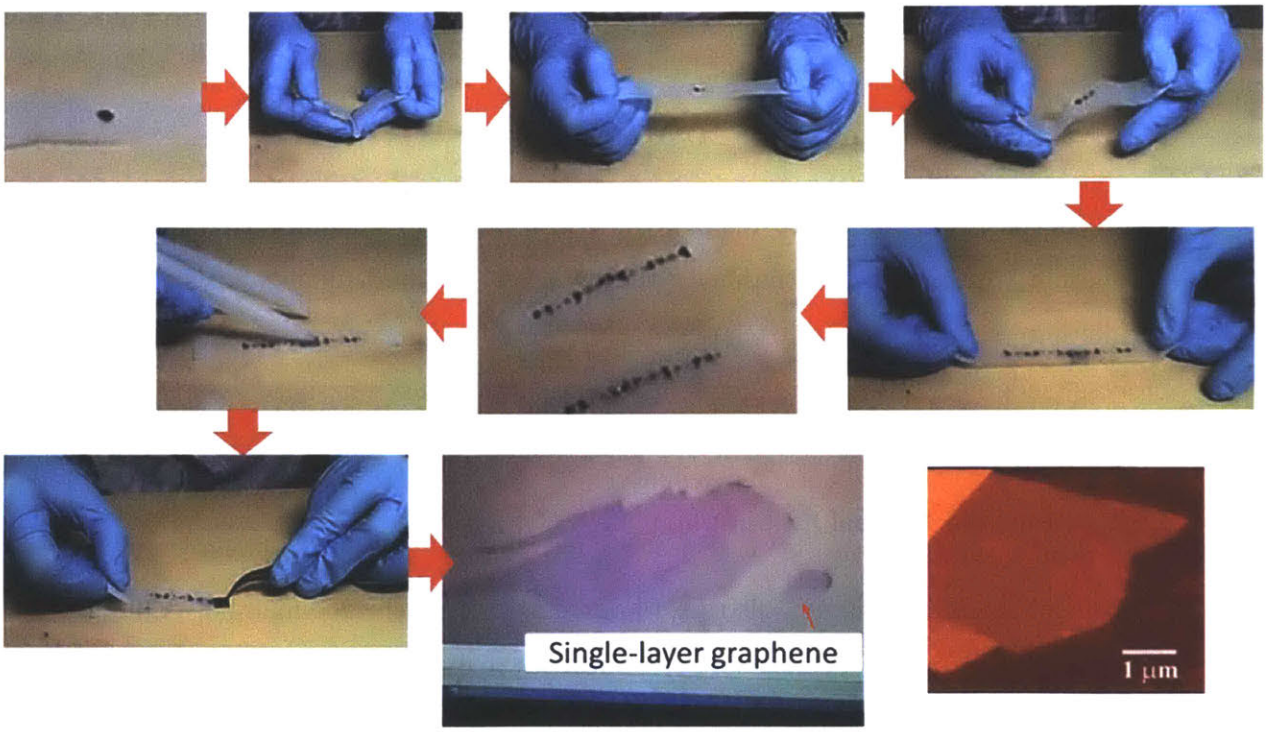

Figure 2-11: An experimental procedure of the micromechanical exfoliation of highly oriented pyrolytic graphite (HOPG): The bottom center image is an optical microscope image of the produced graphene flakes where different colors represent varying thickness due to optical contrast; the bottom right image shows an atomic force microscopic image of the flake which is widely used for layer number identification. Image from Ref[25]

2.3.2 Liquid Phase Exfoliation

Another possible route that may enable mass production of 2D materials is sonication-assisted liquid phase exfoliation of bulk layered materials, resulting in large quantities of 2D nanosheets dispersed in a liquid phase such as organic solvents or surfactant solutions. In this strategy, strong ultrasonic waves are applied to bulk layered materials in organic solvents or surfactant solutions, which leads to the formation of the liquid cavitation as schematically illustrated in Figure 2-12. When these cavitation bubbles collapse into microjets of high energy and consequently the surfaces of the material are exposed to shock waves, compressive stress waves propagate through the material that breaks apart the layered crystallites into thin 2D flakes with a varying size and thickness depending on the experimental conditions.

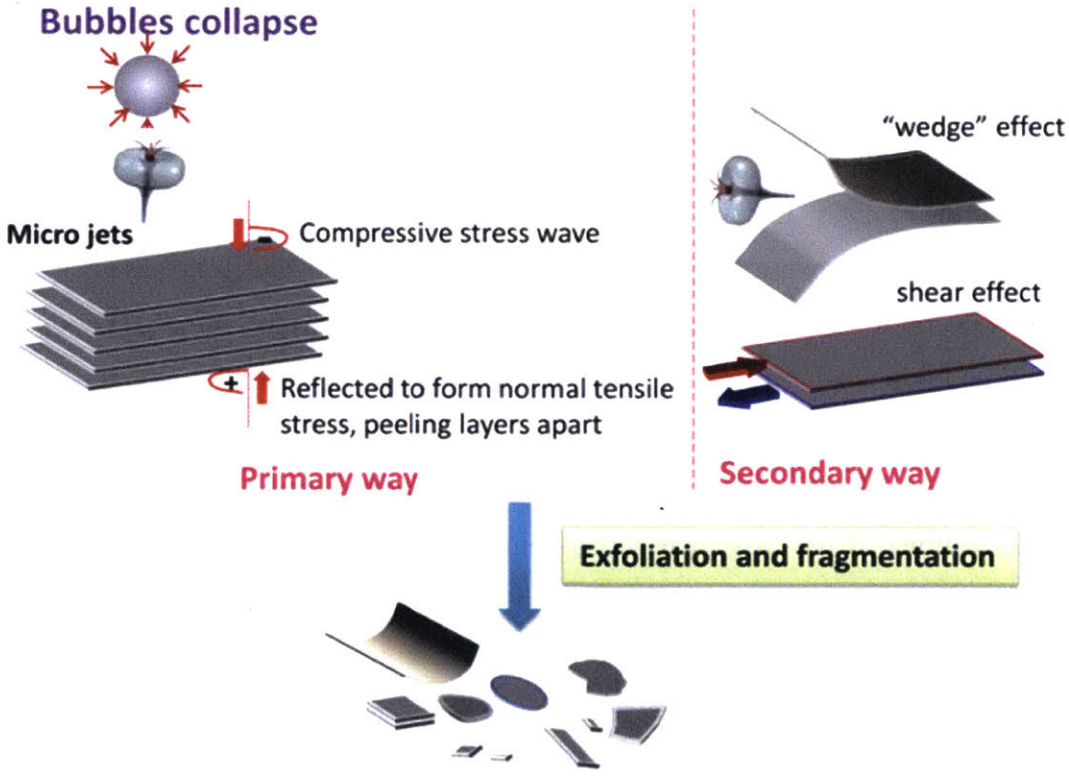

Figure 2-12: A schematic illustration of the mechanical process of the sonication-assisted liquid phase exfoliation. Image from Ref[25]

However, it is challenging to produce dispersion solutions of 2D flakes with large area as well as few-layer thin thickness using this method, which is of significance for this synthetic

route to be widely adopted for nanoelectronic device applications. In most cases, the difficulty originates from high interfacial tension that forms at the interfaces between 2D layers and solvents, thereby rendering increasing surface area in the liquid phase undesirable thermodynamically. In order to reduce the high interfacial tension, various types of surfactant molecules may be introduced to the solution that can bridge between the 2D surfaces and solvent molecules.

2.3.3 Chemical Vapor Deposition (CVD)

Chemical vapor deposition (CVD), or vapor-phase growth process, is a chemical synthesis process that has been widely and extensively investigated since the advent of graphene to synthesize various types of 2D materials, such as semiconductors, metals and insulators. Most of the early efforts had been focused on graphene growth, where catalytic reactions of methane and hydrogen occur on the surface of copper or nickel at around 1000°C—dissolved carbon atoms precipitates when cooled down or directly dissociates methane on the surface of the metal support.[26, 27] Similarly, this synthetic approach has also been explored for the synthesis of TMDCs. In this thesis, uniform large-area MoS_2 thin films are grown by the CVD process, as shown in Figure 2-13,[28] where solid S and $MoCl_5$ are used as precursors to grow MoS_2 on a SiO_2/Si or sapphire substrate in a vacuum tube furnace. By optimizing the growth conditions—temperature, total pressure, etc.—and the initial amounts of precursors, uniform layers of one, two, or multiple layers of MoS_2 are successfully achieved. The Raman and photoluminescence (PL) spectra in Figure 2-13 (d-e) show monolayer MoS_2. Once the growth is finished the as-grown MoS_2 films can also be transferred from the SiO_2/Si (or sapphire) growth substrate into arbitrary substrates by the transfer process shown in Figure 2-14, where PMMA is used to coat the MoS_2 as a protective mediator, and KOH solution is used to release the film from the substrate. Finally, additional characterization of the film after transfer to a transparent substrate is shown in Figure 2-15.

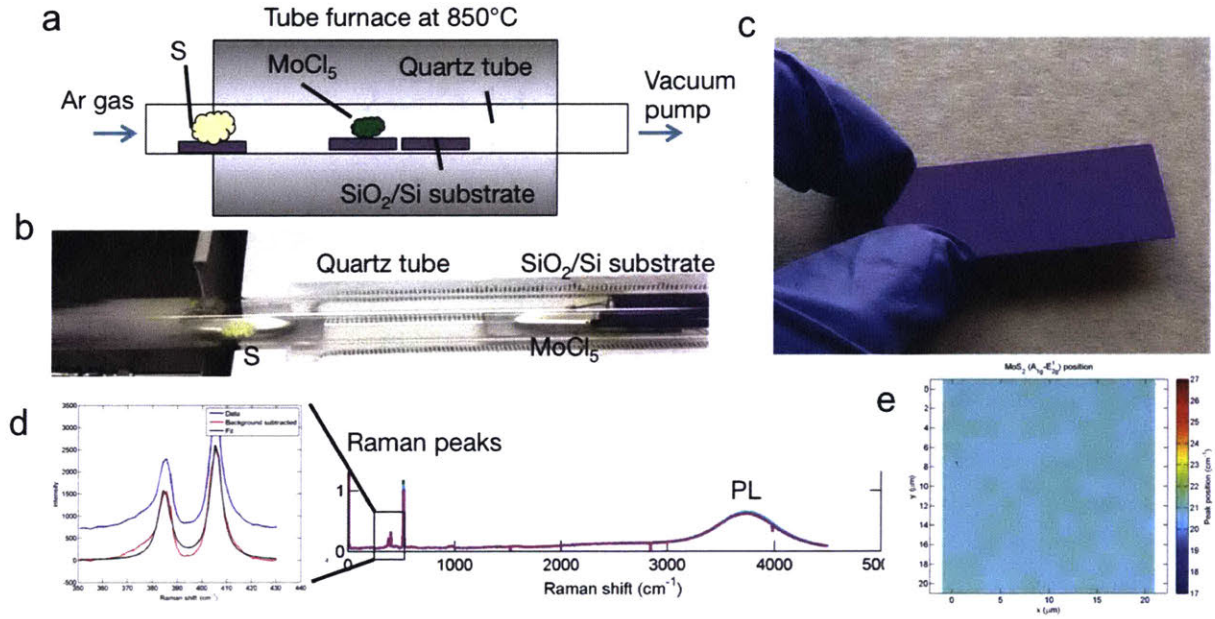

Figure 2-13: (a) Schematic of chemical vapor deposition growth of MoS_2 on SiO_2/Si substrates from S and $MoCl_5$ precursors. (b) Photograph of CVD furnace implementation. (c) Photograph of SiO_2/Si wafer covered in MoS_2 monolayer film. Scratches in the film reveal SiO_2 below. (d) Raman and photoluminescence (PL) peaks. (e) Spatial map of the difference between Raman peaks indicating film uniformity.

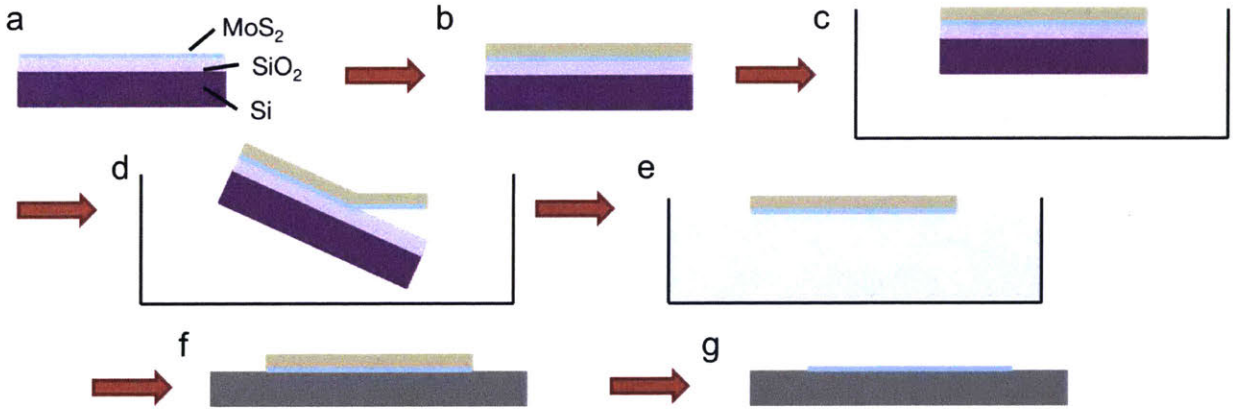

Figure 2-14: Transfer process to move MoS_2 from original growth substrate to arbitrary substrates. (a) MoS_2 grown by CVD on SiO_2/Si substrate. (b) MoS_2 is covered in PMMA film by spin coating. (c) PMMA/MoS_2/SiO_2/Si stack is floated onto surface of a warm bath of 1 M aqueous KOH solution. (d) The KOH etches the SiO_2/Si, allowing the PMMA/MoS_2

film to be released. (e) The PMMA/MoS_2 is scooped out and floated onto DI water for rinsing. (f) Any arbitrary substrate can be used to scoop up the PMMA/MoS_2 film. (g) After drying, the PMMA is removed by acetone. MoS_2 is now on arbitrary substrate.

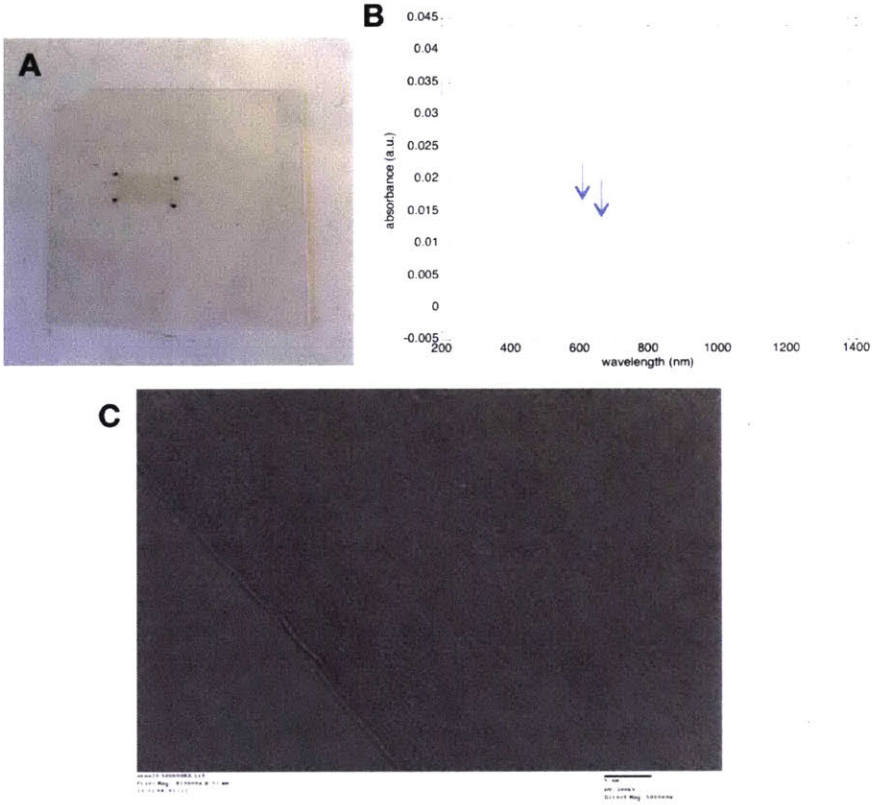

Figure 2-15: Additional characterization of MoS_2 CVD films. (A) Photograph of a 5mm x 2mm MoS_2 bilayer film transferred to a quartz slide. (B) Absorbance spectrum of the transparent film in (A), with the arrows indicating excitonic peaks. (C) TEM image of bilayer MoS_2.

Further characterization on the CVD-grown MoS_2 trilayer have been performed by AFM, XPS, and contact angle measurements. Figure 2-16 shows AFM topographic images of as-grown trilayer MoS_2 ultrathin film over a 1μm x 1μm area on SiO_2 substrate. It is clear that the film covers the entire area without any noticeable patches or cracks, while it has some level of roughness observed which might be due to roughness of the substrate or remaining residues after reaction.

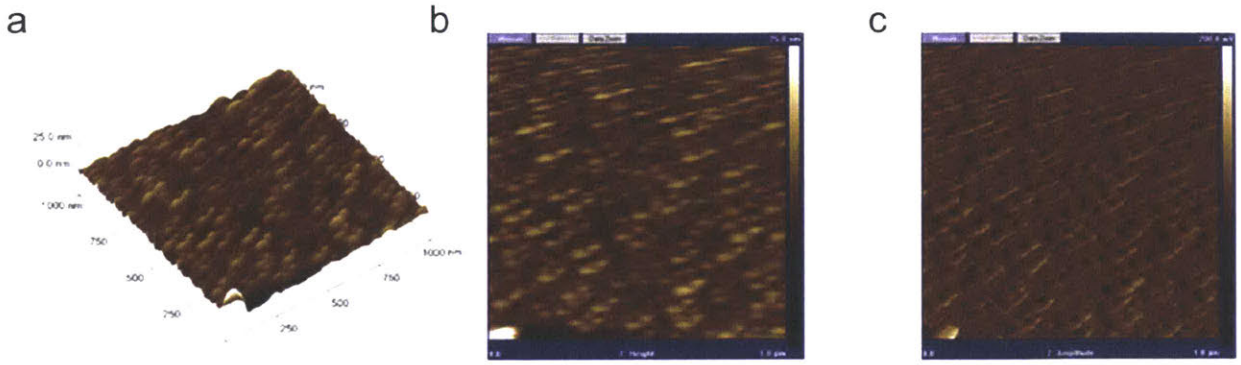

Figure 2-16: AFM characterization of MoS_2 CVD films. (a) 3D height, (b) 2D height, and (c) amplitude profiles of trilayer MoS_2. All obtained under tapping mode measurements.

X-ray photoelectron spectroscopy (XPS) surface elemental analysis was conducted using a ThermoFisher ESCA Lab 250xi equipped with MgKα radiation (1253 eV) and operated at 23 kV and 13 mA. The binding energy was referenced to C1s line at 284.76 eV for calibration. The chemical composition of the surface was obtained by comparing the peak areas of their spectra. Table 1 shows the results with and without deconvolution (using the software package PeakFit v. 4 from AISN Software Inc., USA). As can be seen in Figure 2-17, it is very clear that MoS_2 is obtained on SiO_2 considering the binding energy matching the expected for MoS_2 and SiO_2 (the atomic percentage of S is double that of Mo and that of O is double that of Si). The results also confirm that the MoS_2 film is very thin since the very surface active XPS techniques were able to penetrate the film and obtain signal of SiO_2 substrate. The carbon is always detected and it is possibly from the pump rather than from the sample.

(Table 1-a)

Name	Peak BE	Height Counts	FWHM eV	At. %	Q
C1s	284.59	22764.2	1.17	24.18	1
Mo3d5	229.7	35717.58	0.8	3.67	1
O1s	532.95	93654.51	1.34	43.66	1
S2p	162.52	12827.42	0.83	6.74	1
Si2p	103.63	17893.4	1.44	21.75	1

(Table 1-b)

Name	Peak BE	Height Counts	FWHM eV	At. %	Q
C1s	284.58	21100.25	1.09	15.97	1
C1s A	285.76	2978.04	2.67	5.58	1
Mo3d5	229.7	35717.58	0.8	3.3	1
Mo3d3	232.86	26011.96	1.02	4.51	1
O1s	532.95	94299.46	1.29	34.29	1
O1s A	531.21	11417.99	1.59	4.99	1
S2p3	162.51	12879.65	0.83	6.28	1
S2p1	163.71	6597.42	0.74	5.51	1
Si2p	103.63	17893.4	1.44	19.56	1

Table 1: X-ray photoelectron spectroscopy (XPS) surface elemental analysis: The chemical composition of the surface was obtained by comparing the peak areas of their spectra. The results are reported (a) with and (b) without deconvolution using the PeakFit software.

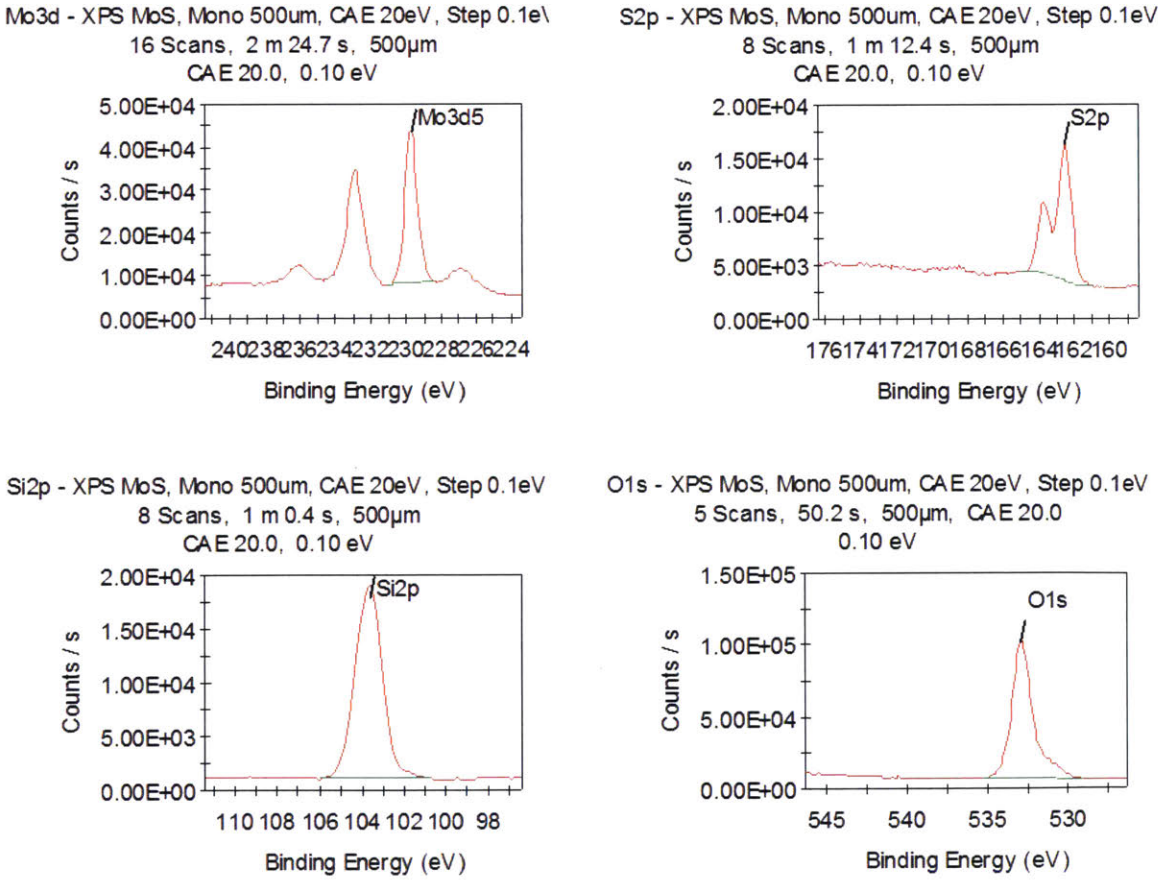

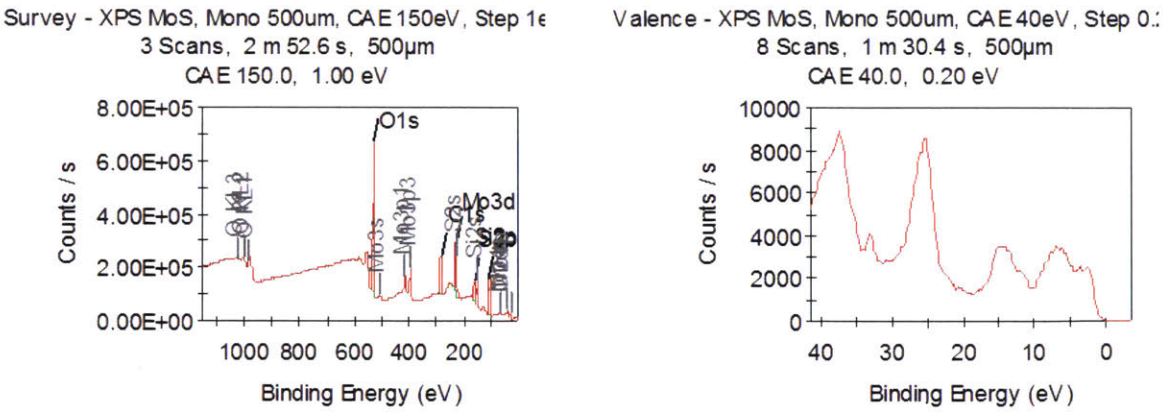

Figure 2-17: X-ray photoelectron spectroscopy (XPS) surface elemental analysis: MoS_2 is obtained on SiO_2 considering the binding energy matching the expected for MoS_2 and SiO_2 (the atomic percentage of S is double that of Mo and that of O is double that of Si).

Contact angle measurements have been performed as shown in Figure 2-18 and the Laplace-Young equation (Static contact angle of a sessile drop) is adopted for analysis. The contact angle was found to be 77.8° and the interfacial tension (determined using the image scale and the difference between water and air densities) is 84.7 mNm^{-1}.

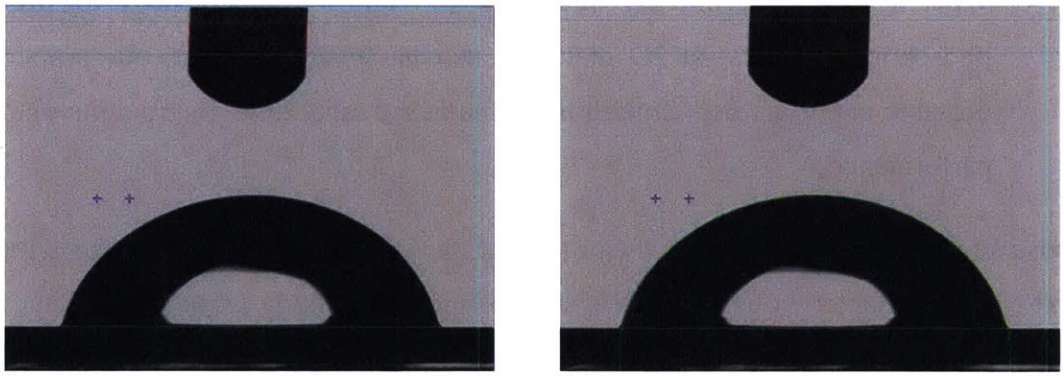

Figure 2-18: Contact angle measurements on two different CVD MoS_2 films.

2.4 Outline of Thesis

The focus of this thesis is on the exploration of unique electronic and optoelectronic properties of a few 2D materials, underlying physics at their junctions with metals or dissimilar 2D crystalline layers, and on developing high-performance nanoelectronic devices exploiting these junctions.

The following questions on 2D materials considered are addressed via this thesis:

- What is the mechanism that dominates the charge carrier transport phenomena at the nanoscale interface between an ultrathin 2D crystalline layer and a metal? How does the layer number of the 2D materials play a role in this process?
- How does the transport mechanism revealed in the dark lead to a peculiar layer number dependent photoresponse of MoS_2, one of the 2D materials?
- What interfacial phenomena occur when two dissimilar 2d materials are brought into contact? And how the phenomena can be taken advantage of to build a nanoelectronic device with an advanced performance that is otherwise impossible to achieve?
- What is the experimental strategy that can be implemented to protect black phosphorus crystals—a 2D materials that has many advantageous properties but is unstable under ambient conditions—and at the same time, improve its optoelectronic performance?

These questions are addressed in the order that they are raised above. The thesis begins in the next chapter (chapter 3) by building a state-of-the-art scanning probe instrument, which is a single experimental platform capable of simultaneous characterization of morphological, electronic, and optoelectronic properties of pre-assembled devices.

I then use this equipment to investigate the layer number dependence of MoS_2 properties, a unique phenomenon that can be found in 2D materials that makes them extremely attractive. Dark current measurements in both forward and reverse bias on a bilayer MoS_2 flake reveal that the charge carrier transport at the nanoscale junctions with the metal tip is largely dominated by tunneling events, and the energy barrier height is extracted. Furthermore, by taking a series of current images, prominent dependence of transverse conductivity on the

layer number of MoS_2 is clearly observed and a dominant charge carrier transport mechanism is discussed in detail. Under laser illumination, spectral response of different thickness regions varies, which may originate from the thickness-dependent electronic band structures of quantum confined 2D materials. Interestingly, the photocurrent response rebounds after gradual decrease up to 4 layers and I interpret this taking into account the competition between light absorption by the material and photocarrier collection processes.

With the deep and comprehensive understanding of the charge carrier transport and photophysical processes that govern the experimental platform, in chapter 4 I measure a more complicated, but at the same time, more interesting system—a WSe_2-MoS_2 in-plane p-n heterostructure. In consecutive current images taken with varying bias voltages, WSe_2 and MoS_2 show an opposite trend due to their distinct work functions that lead to different shapes of the Schottky barrier that forms at the junction with the metal tip. Also, measurements under laser illumination show the photoresponse that has a strong dependence on the applied bias voltage. By modulating the polarity and magnitude of the voltage, the photoresponse pixels in part of the heterostructure were selectively switched on and off, demonstrating a hyper-resolution switchable photodiode array.

I then take the insights gained one step further and explore the interfaces between dissimilar 2D materials. The chapter 5 starts with characterizing junctions formed between single layer graphene and single- and few-layer MoS_2: Raman spectroscopy, photoluminescence, and conductive-AFM measurements are performed. The Raman spectroscopy and conductive AFM results point to there is a noticeable charge transfer between the two materials. A significant reduction in photoluminescence intensity of monolayer MoS_2 upon making contact with graphene reveals the existence of a built-in electric field that splits the excitons at the junction, rendering a recombination process less efficient. Taking advantage of this understanding of the heterojunction, field-effect transistors (FETs) are fabricated whose operation can be tuned by modulating the junction properties. Finally, in the later part of the chapter 5, a black phosphorus-MoS_2 junction is investigated. It is demonstrated that CVD-grown monolayer MoS_2 can function as a passivation layer while maintaining transport characteristics and even enhancing photoresponse intensities.

3. Layer Number Dependence of MoS_2 Photoconductivity Using Photocurrent Spectral Atomic Force Microscopic

3.1 Introduction

MoS_2 is a layered semiconducting transition metal dichalcogenide material whose single and few layer nanosheet forms are recently receiving significant interest as promising materials for electronic and optoelectronic devices. They have unique electronic and optical properties originating from 2D quantum confinement:[29-35] when MoS_2 is thinned to atomically thin sheets from the bulk, the optical bandgap increases and transitions from indirect to direct.[3] While MoS_2 has recently been demonstrated as the active material in a wide range of electronic[36, 37] and optoelectronic[35, 38-41] applications in addition to conventional field-effect transistors (FETs)[4], many questions remain about the spatial uniformity of properties across MoS_2 layers, as well as the layer number dependence of optoelectronic properties. In this work, we perform photocurrent spectral atomic force microscopy (PCS-AFM) for the first time to analyze the nanoscale junction between a conductive metal tip and MoS_2 samples varying in thickness from one (1L) to twenty layers (20L) to answer these important questions.

The layer number dependent electronic and optical properties of MoS_2 provide many interesting and important opportunities for applications in optoelectronics. When MoS_2 is isolated as a single layer, quantum confinement induces a transformation from an indirect bandgap of 1.3 eV for bulk MoS_2 to a direct bandgap of 1.8 eV, as has been experimentally shown, resulting in significant photoluminescence for its 1L form.[6] This behavior makes MoS_2 an intriguing candidate material in a wide variety of electronic and optoelectronic applications.[42-44] Atomically thin MoS_2 has been successfully used in digital electronic components[4, 34, 45-51] and circuits[37] because its sizeable bandgap enables a low current in the off state, so that high on/off current ratios[4, 52, 53] are possible. As electronic and optoelectronic devices become smaller and smaller, the electrical contacts must also be reduced in scale.

However, reducing MoS_2–metal contacts to nanometer size can produce different properties from those of the macroscopic counterparts. Moreover, the interfaces between atomically thin MoS_2 and contact and dielectric materials may differ from those with bulk MoS_2, and may have a substantial impact on the performance of devices.[54-56] Therefore, a thorough investigation of the underlying physics of the interfaces between atomically thin MoS_2 sheets of varying layer numbers and metal contacts is essential for controlling and tuning their performance.

However, there have been few studies to date that investigate charge transport behavior in the vertical direction at the nanoscale MoS_2–metal interface.[57] Thus, in this work we focus on the transverse electrical properties of nanoscale MoS_2–metal junction in the dark and under illumination of varying wavelengths using conductive and photoconductive spectral atomic force microscopy (C-AFM and PCS-AFM) measurements. By performing current imaging using a PtIr-coated conductive tip on an ultrathin MoS_2 nanosheet that contains regions of different layer thicknesses, we can form many thousands of MoS_2–metal contact points during imaging and directly compare layer-number dependent properties at the same time under the same experimental conditions with high spatial resolution. In contrast, studying these properties by the fabrication and testing of individual FET devices introduces significant complexity due to lithographic and metal deposition processes that can damage the MoS_2 sheets or change the intrinsic character of the junctions, and does not allow for spatial variations to be examined.

Li *et al.* [57] have performed a C-AFM study of multilayer MoS_2 on a Pt substrate using a CoCr conductive tip, showing that the resulting diode characteristic can be explained by the thermionic emission and the Fowler-Nordheim (FN) tunneling models for the forward and reverse tip bias regimes, respectively. However, this earlier study is not conducted on 1L and 2L MoS_2 and is limited to dark currents, leaving the influence of photoexcitation and the interesting bandgap transition unanswered. Moreover, the use of single point *I-V* curves makes this study unable to answer questions of local spatial variations at the micro- and nanoscale.

In this chapter, we study for the first time the layer number dependent electrical characteristics of the MoS_2–metal nanoscale junction using current imaging of MoS_2 nanosheets consisting of regions of different thicknesses from 1L to up to 20L in both forward and reverse bias regimes using C- and PCS-AFM. By taking consecutive current images while changing bias voltages, we measure the layer number dependence of the effective barrier, showing it to be linear. We also obtain spatially resolved two-dimensional (2D) maps of local electrical properties from simultaneously recorded local *I–V* data. In addition, we investigate the layer number dependent spectral photoresponse of MoS_2, which showed the highest response in 1L. The photoresponse decreases for increasing layer number, but increases again between 4L and 10L due to increased light absorption. The photoresponse is also strongly dependent on the wavelength of the incident light, showing much higher currents for photon energies that are above the optical bandgap. The photoresponse in forward and reverse biases shows barrier symmetry for 1L but asymmetry for 2, 3, and 4L, which further indicates a dominant role of the barrier on carrier transport at the junction. This insight into the physical carrier transport mechanisms in MoS_2 provides critical information for further engineering MoS_2 electronic and optoelectronic devices with tuned electrical characteristics at the nanoscale level.

3.2 Experimental Methods

3.2.1 Instrumental Setup: Photoconductive Spectral Atomic Force Microscopy (PCS-AFM)

The photoconductive spectral atomic force microscopy (PCS-AFM) that we have built is a state-of-the-art, first of its kind, single experimental platform for characterizing morphological, optical, and electronic properties of pre-assembled devices, and in particular, atomically thin 2D nanomaterials (Figure 3-1). We have built the instrument based on a typical atomic force microscope (AFM) setup with an inverted optical microscope at the bottom side for laser illumination. The instrument is equipped with three optical filter wheels to select 14 wavelengths of laser illumination from a supercontinuum broadband laser source (The band pass filters range from 350 to 1000 nm in steps of 50 nm, each with a bandwidth

of 10 nm). The filters can be replaced with a monocromator to fine-tune the wavelength of laser excitation, which will allow more detailed exploration of the optoelectronic properties of the materials under investigation.

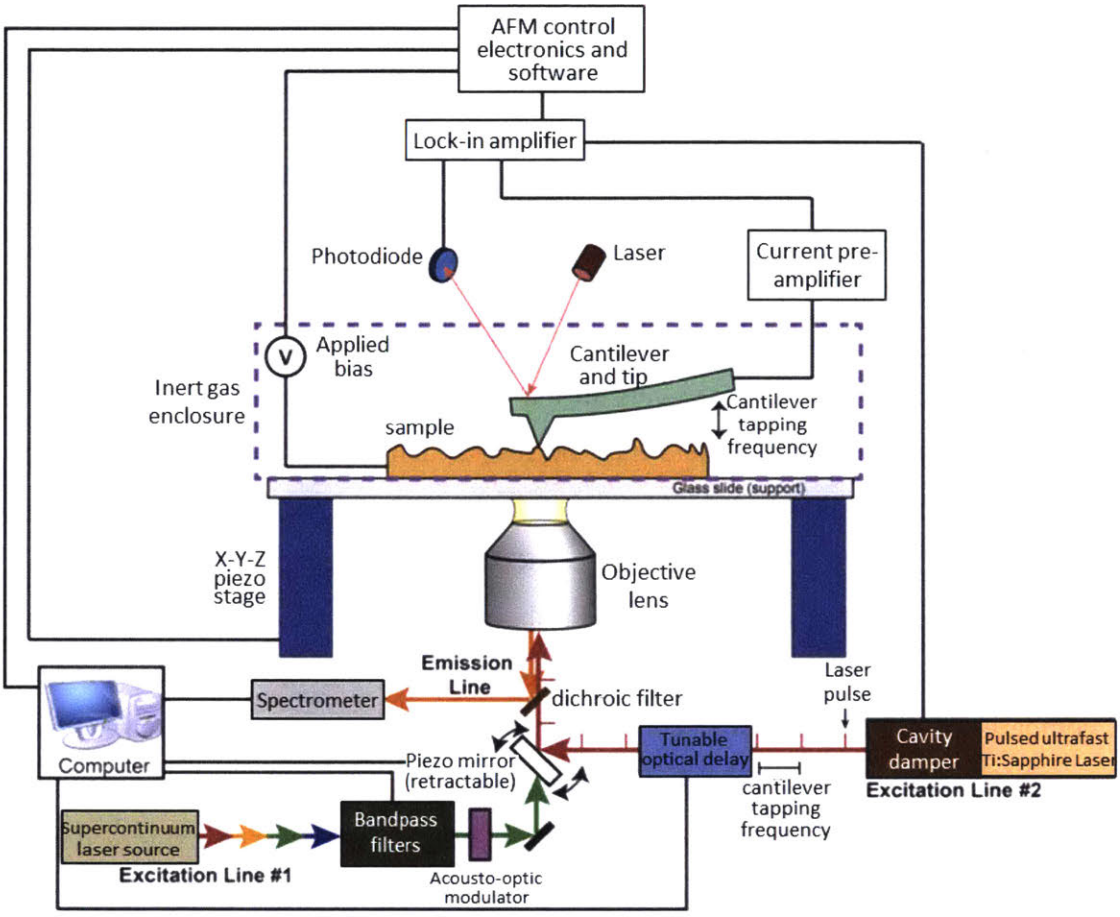

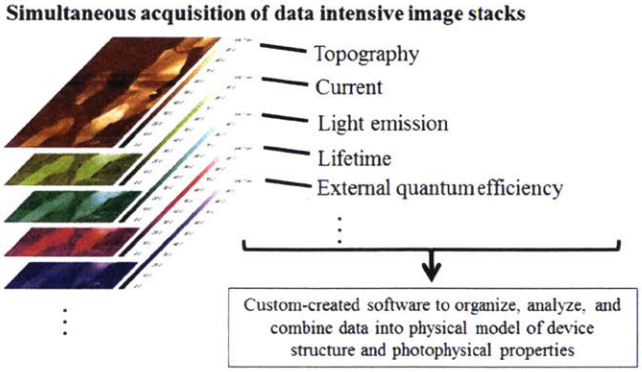

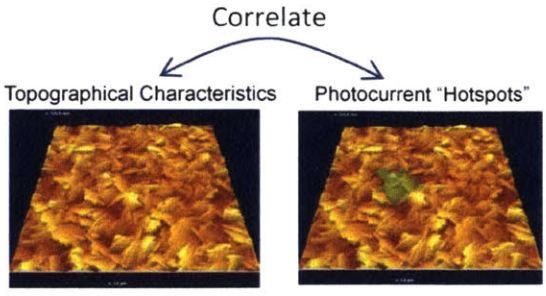

Figure 3-1: A schematic of the PCS-AFM setup: simultaneous image stacks varying devices parameters that can be deconvoluted from a single-platform measurement, enabling correlation between materials reactivity hotspots and nanoscale morphological features.

The most significant advantage of the instrument is that it enables a correlation between topography and current (or photocurrent), and emission images at the nanometer-scale level. Previously, investigation of spatially-resolved photoresponse of 2D materials has been attempted using different experimental setup including scanning photocurrent microscopy, which is based upon the typical FET device architecture.[58] However, this technique does not provide morphological information of materials being inspected, which makes it difficult to study underlying physics that causes spatial variation. Moreover, separated photoexcited charge carriers have to make travels all the way to the electrodes through the entire channel region during which the carriers may be lost at defects and various trap sites, making the detection of subtle local variations difficult. In contrast, the PCS-AFM has higher carrier collection efficiency by collecting the carriers in the vertical direction through the tip that is in contact with the material surface. Furthermore, since all data points in each image are generated simultaneously with the identical experiment condition, accurate and reliable comparisons can be made with confidence. If a specific optoelectronic activity is pronounced at a nanoscale feature (e.g. photoconductivity hotspot), we can confidently correlate the activity with local nanoscale morphology of the hotspot, and can explore the fundamental concepts behind this phenomenon (Figure 3-1). These novel correlations of the performance hotspot with a specific morphological feature will guide us on the optimization of materials design (morphology, structural features) to improve the overall device performance for target applications.

3.2.2 Example Data Sets of PCS-AFM Mesurements

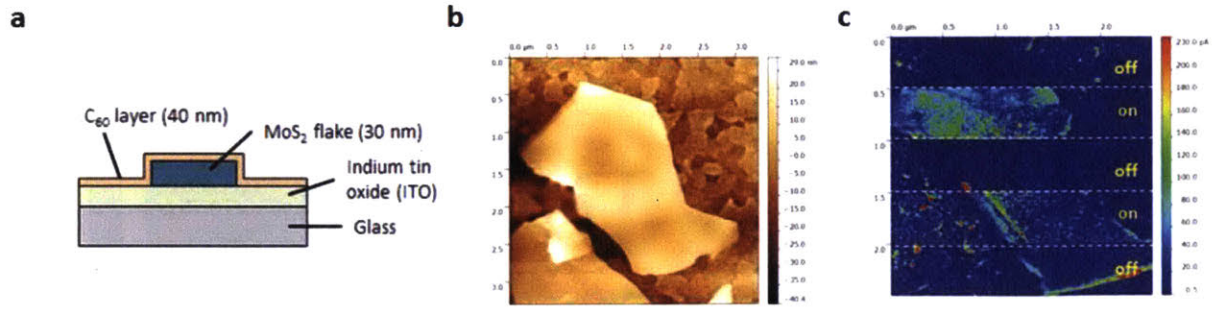

Figure 3-2: (a) Cartoon of a cross section of MoS_2/C_{60} sample on ITO/glass substrate. (b) AFM topography (c) and corresponding PCS-AFM using Pt/Ir coated tip, at 8V with alternating laser illumination (λ=700nm).

In order to test spectral photocurrent responses using the PCS-AFM setup, in this section, a molybdenum disulfide (MoS_2):C_{60} heterostructure is selected: MoS_2 is a semiconductor classified as the transition metal dichalcogenides that can be exfoliated from the bulk form into atomically thin layers as graphene. MoS_2 exhibits an indirect band gap of 1.3eV in the bulk, but transitions to a direct band gap of 1.8eV when thinned down to a single layer[1]. Considering energy level alignment of the conduction and valence band of MoS_2 and HOMO and LUMO of C_{60}, this MoS_2:C_{60} heterostructure can be a possible candidate for a donor:acceptor material for photovoltaic devices. Therefore, simultaneous nanoscale measurement of spatial topography, photocurrent and consequent quantum efficiency of the heterostructure on ITO substrate can generate valuable information on its potential for use in photovoltaics.

To prepare the sample, bulk MoS_2 crystal was micromechanically exfoliated onto an ITO-coated glass substrate, followed by deposition of C_{60} layer using thermal evaporation (Figure 3-2(a)). After locating specific MoS_2 nanosheets by optical microscopy, PCS-AFM measurements were conducted using Pt/Ir coated AFM tip, with the laser illumination focused on the tip-sample contact area. Figure 3-2 (b) and (c) show spatial topology of the MoS_2 nanosheets and the current profile under alternating on/off illumination of 700nm laser at fixed sample bias voltage of 8.5V. It is noteworthy that noticeable current enhancement was detected under laser illumination compared to in dark, and the alternating on/off regions emphasizing the stability of the instrument in photocurrent measurements.

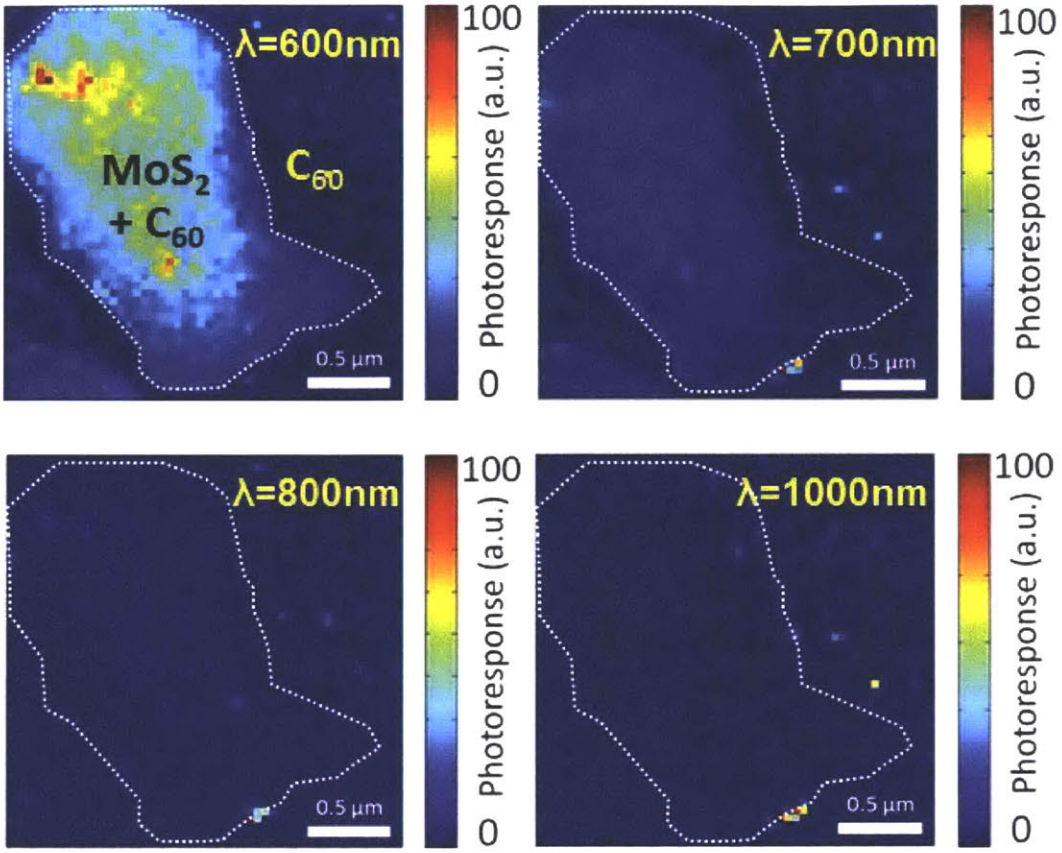

Figure 3-3: Nanoscale visualization of local photo response to different excitation laser wavelengths normalized by laser intensity. Pixels come from averaging over neighboring data points.

To further investigate nanoscale spectral photoresponse, PCS-AFM current maps were obtained at constant 8 V sample bias using the same MoS_2 flake as in Figure 3-2 with laser illumination of varying wavelengths (Figure 3-3). The current images acquired under illumination and in the dark are subtracted and then normalized by the optical intensity at each wavelength. The figures clearly show higher photoresponse with decreasing wavelength of laser excitation, as expected, with minimal current enhancement with 1000nm and 800nm laser used: Incident photons with energy higher than the band gaps of MoS_2 and C_{60} will excite electrons, thereby contributing to the enhanced current upon illumination. In addition, extra energy given to the hot carriers from photons with shorter wavelengths helps hot carriers have higher chances of overcoming energy barriers formed at the contacts between ITO substrate, MoS_2, C_{60}, conductive tip, and metal wires to actually contribute to the current enhancement. In this way, nanoscale local quantum efficiency mapping under a number of

different excitation wavelengths will be possible with simultaneous topographic characterization using the PCS-AFM setup. Therefore, a variety of complex candidate photovoltaic active layer materials and others may be able to take advantage of the instrument for nanoscale understanding and morphological optimization.

3.2.3 Sample Preparation and PCS-AFM Imaging

MoS_2 single crystal nanosheets were deposited onto ITO-coated glass substrates (Sigma Aldrich) by micromechanical exfoliation[59], followed by annealing in argon at atmospheric pressure at 250°C for 1 h in order to remove tape residues and improve the contact quality between the sample and the substrate surface. Prior to micromechanical exfoliation, the ITO/glass substrates were cleaned by sonication in acetone, then isopropanol, and blown dry by ultrapure nitrogen before cleaning in an oxygen plasma chamber (Glow Research). Atomically thin MoS_2 nanosheets were first identified by optical microscopy, followed by Raman spectroscopy to identify the number of layers by the difference (Δ) between the two signature Raman peaks of MoS_2: the in-plane vibrational E^1_{2G} and the out-of-plane vibrational A_{1G} peaks, as reported by C. Lee *et al.*[60] Raman spectroscopy was performed on a Horiba Jobin Yvon LabRAM HR800 system with 532nm laser excitation whose output power was reduced using neutral density filters to prevent damaging the MoS_2 samples.

The C-AFM and PCS-AFM measurements were conducted on an Asylum MFP-3D system in ambient conditions, as illustrated in Figure 1a. Conductive imaging used the ORCA conductive module from Asylum and PtIr-coated probes from Bruker. Current and topographic images were obtained simultaneously so that topography and local currents can be directly compared. Most images were 512×512 pixels. For PCS-AFM, the instrument is mounted on an inverted optical microscope (Zeiss) with a 50X objective to focus light through the glass substrate at the tip-sample junction. The illumination source was a supercontinuum laser (SuperK Extreme from NKT Photonics), filtered by bandpass filters (FWHM = 10nm; Thorlabs, Inc.) to illuminate the sample at selected wavelengths. During certain measurements, neutral density filters were used to modulate the laser intensity. AFM

images were analyzed and plotted using the Gwyddion software package,[61] which was also used to calculate the 2D fast Fourier transforms and root mean square roughness values.

3.2.4 Estimation of Effect Contact Area

During C-AFM and PCS-AFM imaging, determining the tip loading force and estimating the effective current emission area are necessary for high spatial resolution and proper analysis of experimentally obtained *I-V* characteristics while not damaging the sample under investigation. In our C-AFM experimental setup the nanoscale contacts are formed between the conductive tip and MoS_2 nanosheet. We used the Hertz contact theory[62-64] to estimate the effective contact area. The tip is assumed to be an elastic sphere and the underlying sample surface is assumed to be flat to describe the contact formed between the tip and MoS_2 nanosheets, as schematically illustrated in Figure 3-4. We assume that the carrier injection is concentrated in this region where the tip and substrate are in contact, and the field contribution from the side part diverges at MoS_2 surface. The contact area radius, a, is calculated by:

$$a = \left[\frac{3RF}{4} \left(\frac{1-\nu_1^2}{E_1} + \frac{1-\nu_2^2}{E_2} \right) \right]^{1/3} \qquad (1)$$

where R denotes the tip radius, F the contact force, $\nu_{1,2}$ the Poisson ratios, and $E_{1,2}$ the elastic moduli of MoS_2 flakes and the conductive tip.

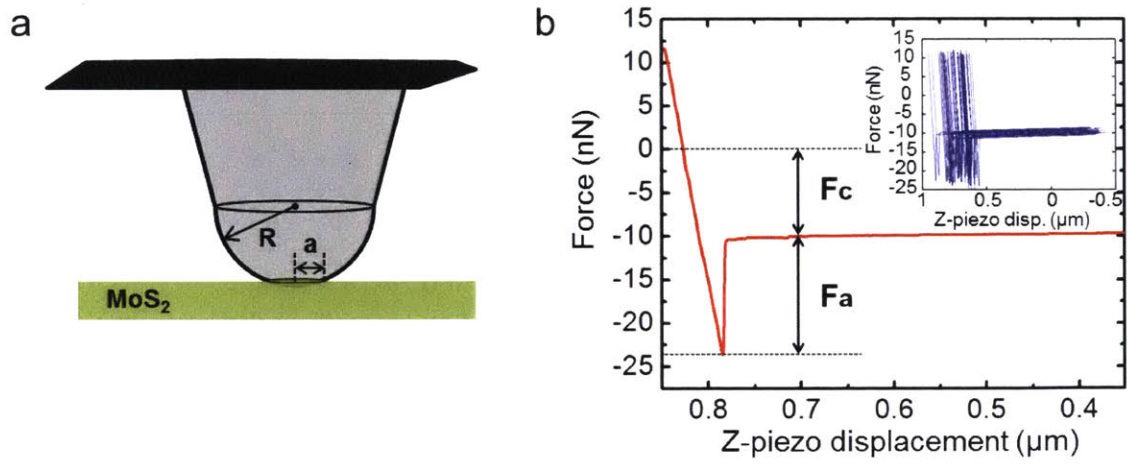

Figure 3-4: (a) Schematic illustration of the contact between the conductive tip and MoS_2 flake surface. R denotes the tip radius and a the contact area radius. (b) Representative force-displacement (F-D) curve in which F_c represents the instrumental deflection set-point force and F_a the additional force between the tip and the sample surface. Inset shows a series of F-D curves taken before and after each of the current images.

Figure 3-4(b) shows a representative force-displacement (F-D) curve of the measurements where retraction force is presented in this figure for clarity. The contact force, F, is the sum of the instrument deflection set point force (F_c) and additional adhesive force (F_a) between the tip and the flake, which was maintained at around moderate value of 20 nN to ensure reliable current measurements while not physically damaging the sample surface or tip coating and preserving high spatial resolution during imaging in order to obtain nanoscale local electronic properties.[65] The inset in Figure 3-4(b) shows a series of F-D curves that were measured before and after each of about 20 image scans. No noticeable change in the physical interaction between the tip and the sample was observed throughout all the experiments, which suggests the C-AFM measurements were reliable and not deteriorated by tip degradation or oxidation. Previously reported elastic moduli and Poisson ratios of platinum, iridium[66] and MoS_2[67, 68] are provided in Table 2 and were used to calculate the effective contact area, $A_e = \pi a^2$, which ranges from 3.88nm^2 to 6.43nm^2.

Table 2: Elastic moduli, Poisson ratios and calculated effective contact area

Material	Elastic modulus (GPa)	Poisson ratio	A_e (F=20-25nN) (nm^2)
MoS_2	350	0.125	3.88 – 6.43
Platinum	170	0.39	
Iridium	528	0.26	

3.3 Experimental Results

3.3.1 Dark Carrier Transport Mechanism

While the electronic properties of materials can be obtained by taking *I-V* curves at fixed positions of interest using C-AFM,[69-74] additional spatially resolved measurement is needed for studying spatial inhomogeneity in local charge distributions, local defects, sample edges, and local tip-sample interactions. Thus, in this section we measure the current through the C-AFM tip while imaging and varying the applied sample bias. We then average the current values across thousands of pixels or data points to obtain spatially resolved *I-V* characteristics of MoS_2 nanosheets.

In order to study carrier transport in the dark, MoS_2 crystals were micromechanically exfoliated onto a conductive indium tin oxide (ITO)-coated glass substrate. The crystals were first identified by optical contrast and then their layer numbers were verified using Raman spectroscopy. The C-AFM and PCS-AFM measurements were conducted using PtIr-coated conductive probes in contact mode. During the measurements, the conductive tip is held at ground while the bias voltage was applied to the ITO substrate as the other electrode. Throughout this work, we refer to forward (reverse) bias when the ITO electrode is positively (negatively) biased relative to the grounded conductive tip. The experimental setup for our C-AFM and PCS-AFM measurements is shown in Figure 3-5.

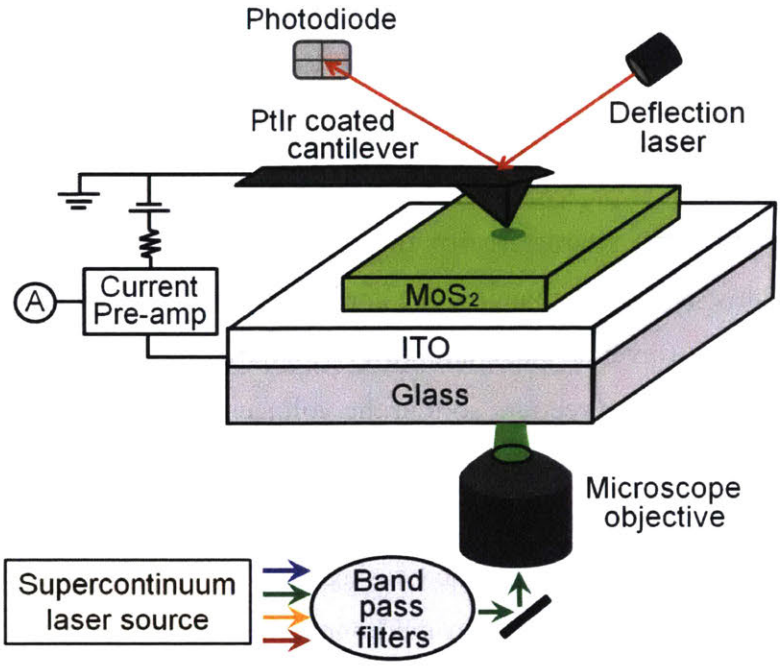

Figure 3-5: A schematic of the photoconductive spectral atomic force microscope (PCS-AFM) instrument.

We identified the thickness of this flake by its Raman spectrum, where the two signature Raman peaks of MoS_2, the E^1_{2G} and A_{1G} peaks, are prominently observed, confirming that the flake is a bilayer MoS_2 crystal based on the frequency difference (Δ) of 21.5 cm^{-1},[60] as shown in Figure 3-6. The spatial Raman map of Δ (Figure 3-6 (c)) confirms that the entire flake is uniformly two layers thick, so that we can average spatial data across the flake and be assured that we are interrogating the same thickness of material.

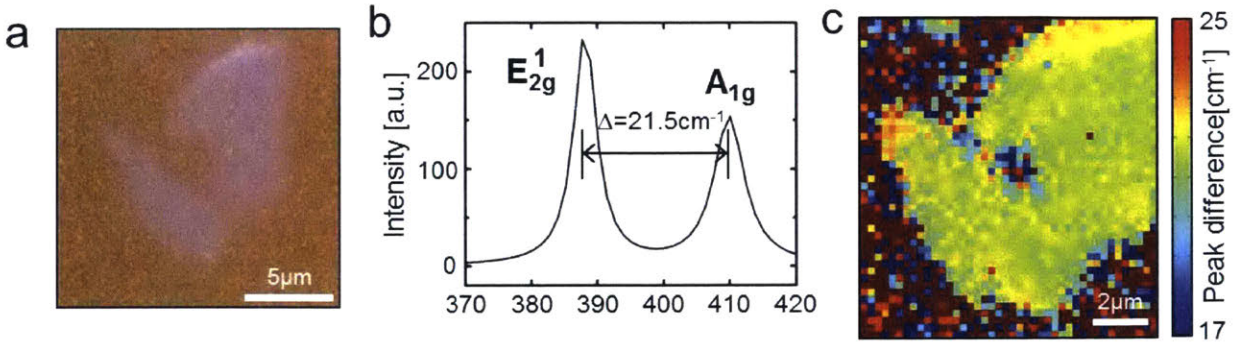

Figure 3-6: (a) An optical microscope image of a flake of MoS_2 on ITO/glass substrate. (The contrast in the image has been enhanced to allow the flake to be more clearly seen.) (b)

Raman spectrum for MoS_2 sample in (a) where the frequency difference of 21.5 cm^{-1} between E^1_{2G} and A_{1G} peaks indicates bilayer MoS_2. (c) A spatially resolved Raman map of the frequency difference shows the uniformity of MoS_2 thickness over the entire sample except for the slightly thicker region at the top edge.

In order to obtain *I-V* characteristics of the MoS_2-metal junction, current imaging was performed on this sample by changing the applied bias voltage in horizontal stripes, as shown in Figures 3-7 (a) (reverse bias) and (b-c) (forward bias). We note that the horizontal direction is the fast scan direction, so that the voltage is being changed approximately every 30 to 40 scan lines. In Figures 3-7 (a), (b-c), the dashed lines denote the points where the bias voltage is changed and the numbers within each stripe indicates the sign and magnitude of the applied voltages. We then obtained a single *I-V* curve by averaging the current values within each voltage stripe and within the boundaries of the MoS_2 crystal, as shown by the black data points in Figure 3-7 (d), where the error bars indicate the standard deviations from all the pixels within the current images at each given voltage. Because we have shown that the flake is uniform in thickness (Figure 3-6 (c)), averaging over thousands of data points for each voltage in this way allows us to obtain a reliable *I-V* curve.

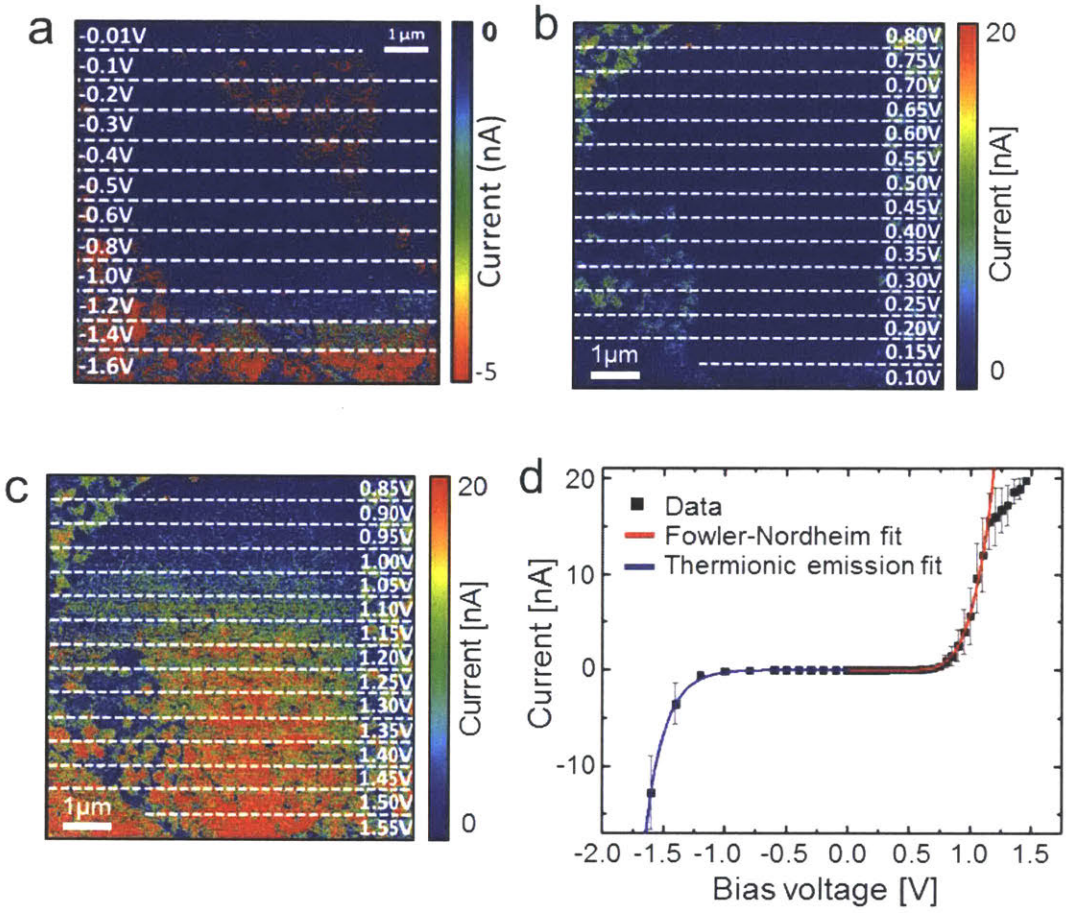

Figure 3-7: (a)-(c) Current images in reverse bias (a) and forward sample bias (b)-(c) taken by changing the applied sample voltage within the horizontal strips. Here the bare ITO surface shows high conductivity while a noticeable nonlinear characteristic is observed in the MoS_2 flake. (d) A current–voltage (*I-V*) curve generated by taking average current values for each bias voltage from the current images where nearly insulating behavior and an abrupt nonlinear increase are observed at low and high bias voltages, respectively. The reverse bias region is fit by a thermionic emission model (blue line) while the forward bias region is fit by a Fowler-Nordheim (FN) tunneling model (red line).

In contrast to the bare ITO surface showing high conductivity, the MoS_2 nanosheet introduces additional resistance against current flow, exhibiting noticeable nonlinear behaviour as a function of applied voltage. This response suggests the formation of an energy barrier at the nanoscale junction between the metal tip and the semiconducting MoS_2 crystal in both forward and reverse bias regimes (Figures 3-7 (a) and (b-c)). The *I-V* curve in Figure 3-7 (d) shows nearly insulating behavior at low bias voltages and abrupt nonlinear increases

in current at high bias voltages. Schematic illustrations in Figure 3-8 show the band structures of the PtIr/MoS_2/ITO system at equilibrium and under applied biases. When the metal tip is brought into contact with a thin MoS_2 crystal, the difference between its work function (Φ_{PtIr} = 5.4 eV[75]) and the electron affinity of MoS_2 (λ_{MoS2} = 4.5 eV[76] for 1L to 4.0 eV[77] for bulk), based on the Schottky-Mott theory,[78] causes a Schottky barrier to form at the interface with an estimated height of about $\Phi_B = \Phi_{PtIr} - \lambda_{MoS2}$ = 0.9 eV for monolayer up to 1.4 eV for bulk. The ITO substrate used in this work is a heavily n-doped with a work function of $\Phi_{ITO} \sim 4.7$ eV, resulting in a nearly ohmic contact with the atomically thin MoS_2 of $\Phi_{MoS2,\,1L} \sim 4.7$ eV.[4, 40, 59] The equilibrium case of the Schottky barrier between PtIr and MoS_2 and the ohmic contact between MoS_2 and ITO is shown in the left panel of Figure 3-8. The reverse bias (V<0) and forward bias (V>0) band diagrams are shown in the middle and right panels of Figure 3-8, respectively. In the forward bias regime, where the barrier height and direction of charge injection suppress thermionic emission to its lowest saturation, the barrier thickness is reduced with higher applied voltage (Figure 3-8), resulting in an enhanced probability of field emission tunneling through the barrier.

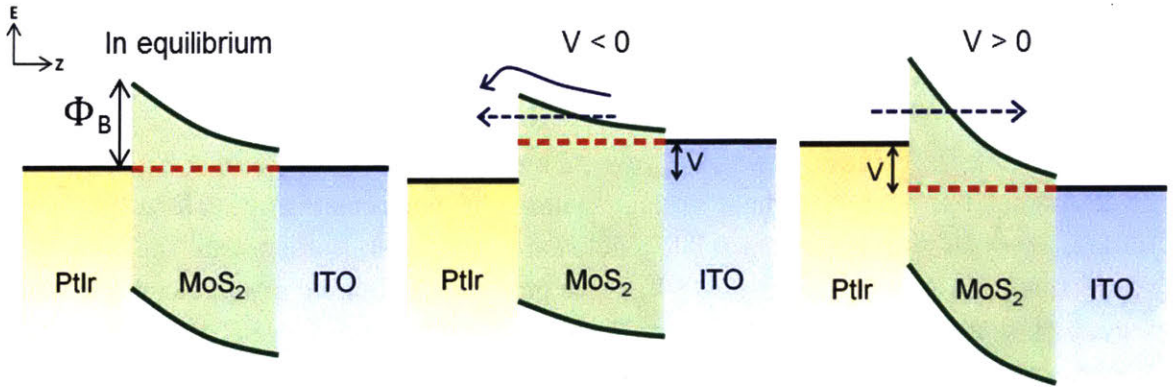

Figure 3-8: A schematic band diagram of a thin MoS_2–metal tip junction in equilibrium (left panel) and under reverse (middle) and forward (right) sample bias voltages. The formation of a Schottky barrier impacts the carrier transport.

We use the Fowler-Nordheim (FN) tunneling theory, which is widely adopted as a model for describing electrons tunneling from the Fermi level of a metal to an adjacent material through a junction barrier, with the current *I* described by:[79]

$$I(V) = \frac{A_e q^3 m V^2}{8\pi h \Phi_B d^2 m^*} \exp\left[\frac{-8\pi\sqrt{2m^*}\Phi_B^{3/2} d}{3hqV}\right] \quad (2)$$

where A_e denotes the effective contact area, q the electronic charge, V the applied bias voltage, h Planck's constant, Φ_B the barrier height, d the distance between the electrodes, and m^*/m ~ 0.35 (for 1L)[42] to 0.53 (for bulk).[57]

The experimental *I–V* data (black squares) in Figure 3-7 (d) are fit to the FN tunneling model in equation (2) (solid red line). We see that the FN model agrees well with the data, except for the deviation at higher applied biases due to the preamplifier's current limit of 20 nA. The effective barrier height formed at 2L MoS_2–metal tip junction, Φ_B, can be extracted from the fitting to the FN tunneling model to be 0.64 eV, which is lower than the value estimated by the Schottky-Mott limit. We attribute this barrier lowering to partial Fermi level pinning arising from the formation of an interfacial dipole and gap states originating from interface charge redistribution and interface hybridizations, leading to a decreased metal work function as theoretically predicted recently by Gong *et al.*[80] A small contribution may also come from defect-induced gap states due to sample imperfections.

In the reverse bias regime, we use thermionic emission to model the charge transport, which was also used earlier by Li *et al.* to explain transport at the junction between a CoCr metal tip and MoS_2 samples of 3, 4, 7 and 20 layers.[57] The thermionic emission model in the reverse bias regime gives the current I and saturation current I_0 as:[81]

$$I = I_0\left[\exp\left(\frac{qV}{\eta k_B T}\right) - 1\right] \quad (3)$$

where $$I_0 = A_e A^* T^2 \exp\left(-\frac{q\Phi_B}{k_B T}\right)$$

and where k_B denotes the Boltzmann constant, q the electronic charge, η the ideality factor, A^* the Richardson constant and V the applied voltage.

The fit to the thermionic emission model of equation (3) is shown as the solid blue line in Figure 3-7 (d). The ideality factor η and the barrier height Φ_B can be calculated from the slope of the linear region and the saturation current I_0 as:

$$\frac{1}{\eta} = \frac{k_B T}{q} \frac{d(\ln I)}{dV} \quad (4)$$

$$\Phi_B = \frac{k_B T}{q} \ln\left(\frac{A^* A T^2}{I_0}\right) \quad (5)$$

The barrier height Φ_B can be calculated from the saturation current I_0 (5.7×10^{-13} A) that was obtained by fitting the data in the reverse bias regime to the thermionic emission model.[81] The Richardson constant (A^*) is expressed as follows:

$$A^* = \frac{4\pi q m k_B^2}{h^3} \quad (6)$$

where k_B denotes the Boltzmann constant, q the electronic charge, m the electron mass, and h the Planck constant. The barrier height can then be calculated as

$$\Phi_B = \frac{k_B T}{q} \ln\left(\frac{A^* A T^2}{I_0}\right) = 1.2\text{eV}$$

The ideality factor η can be calculated from the slope of the linear region shown in Figure 3-9.

$$\eta = \frac{q}{k_B T} \frac{dV}{d(\ln I)} = 5.6$$

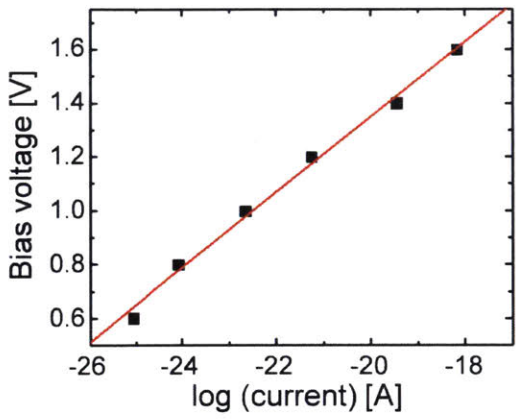

Figure 3-9: A semilogarithmic plot of bias voltage as a function of log (current). A red straight line indicates a linear fit to the data.

The calculated the effective barrier height Φ_B of 0.12 eV is significantly smaller than that extracted in the forward voltage regime using the FN tunneling model. The ideality factor η, which is typically used to assess the deviation of current transport from the ideal thermal emission, has a value of 5.6 here, suggesting that the electron transport in the reverse regime is not fully supported simply by the conventional thermionic emission theory alone. We attribute the origin of this low Φ_B and high η to the increased probability of additional tunneling through the junction barrier, which is not considered in the conventional thermionic emission theory, as the width of the barrier for atomically thin MoS_2 is much thinner than would be expected in conventional junctions. In addition, it has been previously observed that the current behavior is increasingly dominated by tunneling as the nanoscale Schottky diode junction area becomes smaller than the depletion width.[82, 83] Therefore, the conventional thermionic emission theory could underestimate Φ_B and produce a higher η than the real value, suggesting that the current transport in this bias regime has significant contributions from both tunneling through the barrier and thermionic emission.

3.3.2 Layer-dependent Transport Behavior

Since the transport of charge carriers at the nanoscale MoS_2-metal interface is determined by the barrier height and thickness, modulation of the barrier by varying the number of MoS_2

layers introduces new mechanisms for controlling the performance of electronic devices. We used a single nanosheet of MoS_2 with regions of 1, 2, 3, and 4 layers to investigate the electronic characteristics as a function of layer number. Because the same nanosheet has multiple layer thicknesses within a small area that can fit within a single AFM image, we can obtain a series of C-AFM images with varying applied biases under the same experimental conditions. Figure 3-10 (a) shows an optical microscope image of the MoS_2 flake and Figure 3-10 (b) is lateral force microscopy (LFM) image to more clearly show its shape. Raman spectra were taken for thickness identification (Figure 3-10 (d)) where the signature peak difference (Δ) was obtained to be 18.5, 21.5, 22.5, and 23.6 cm^{-1} for 1L, 2L, 3L, and 4L, respectively. The Raman map of Δ in Figure 3-10 (c) shows that the four regions are uniform in their thicknesses of 1L, 2L, 3L, and 4L.

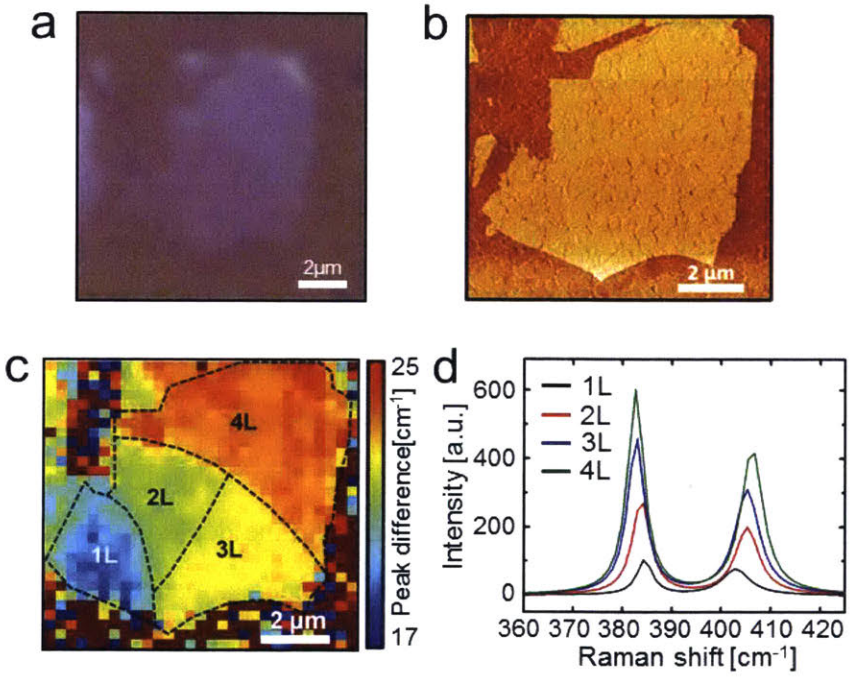

Figure 3-10: (a) An optical microscope image of an exfoliated sheet of MoS_2 on ITO/glass substrate consisting of 1-, 2-, 3- and 4-layer regions. (The contrast in the image has been enhanced to allow the flake to be more clearly seen.) (b) A lateral force microscopy (LFM) image for better visualization of the flake shape. We note that the LFM contrast does not allow the flake thicknesses to be clearly distinguished, but the roughness of the underlying ITO substrate is visible through the flake. (c) Raman map of Δ confirms that thickness of the nanosheet is uniform within each of the regions. (d) Representative Raman spectra taken at

each region where the signature peak difference (Δ) was obtained to be 18.5, 21.5, 22.5, and 23.6 cm^{-1} indicating 1L, 2L, 3L, and 4L, respectively.

The C-AFM images for this sample under forward bias are shown in Figures 3-11.

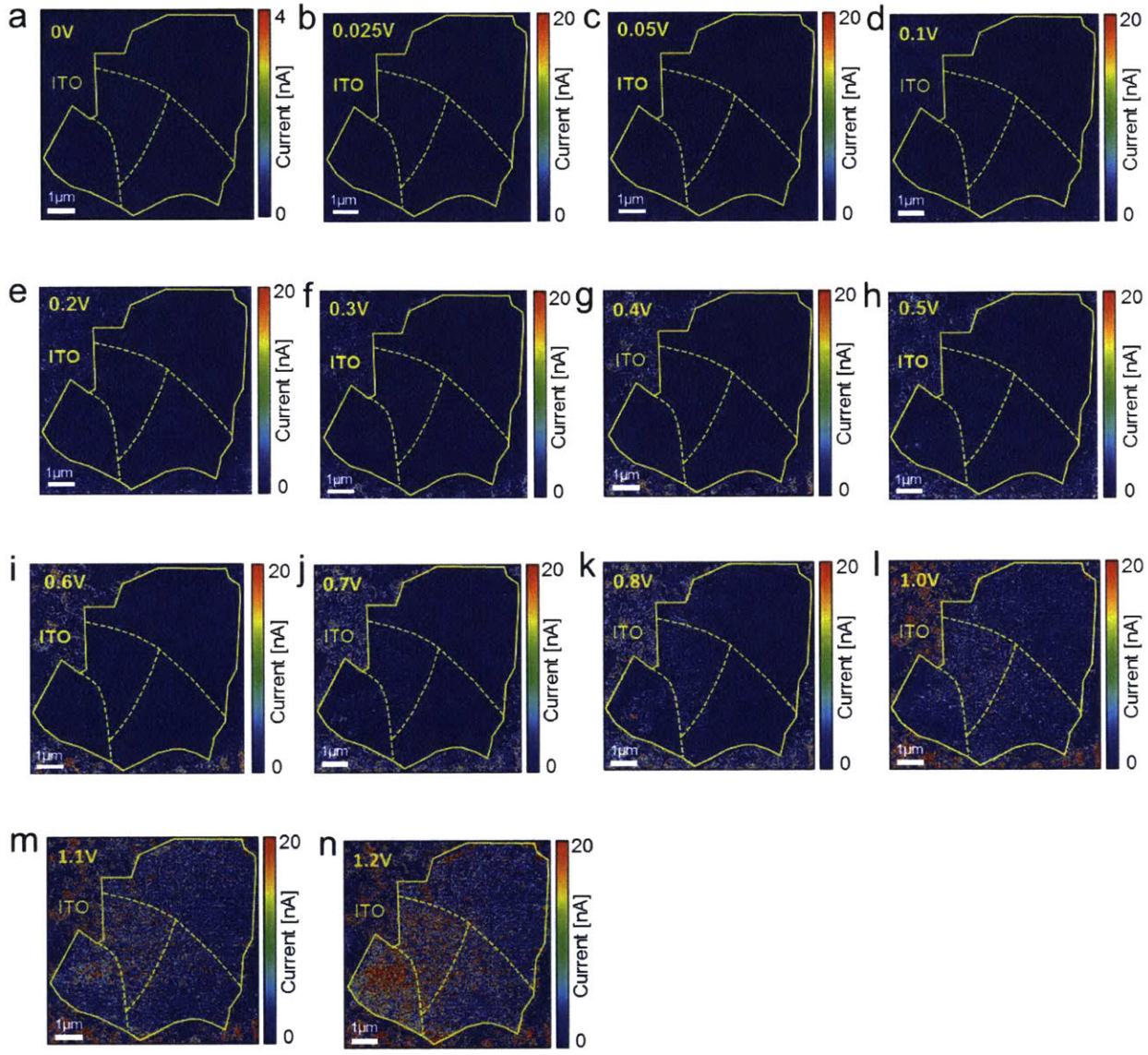

Figure 3-11: Current maps generated by conductive AFM measurements in the dark under applied sample bias voltages of (a) 0 V, (b) 0.025 V, (c) 0.05 V, (d) 0.1 V, (e) 0.2 V, (f) 0.3 V, (g) 0.4 V, (h 0.5 V, (i) 0.6 V, (j) 0.7 V, (k) 0.8 V, (l) 1.0 V, (m) 1.1 V, and (n) 1.2 V. The current increases more rapidly in regions with fewer layers of MoS_2 as the applied voltage is raised.

Just as was seen in Figure 3-7, additional resistance is introduced in the MoS_2-covered region compared to the bare ITO region. The current also increases more rapidly in the regions with thinner MoS_2 as the voltage is increased.

Additional detailed characterization and C-AFM images for different sample considered are performed as follows.

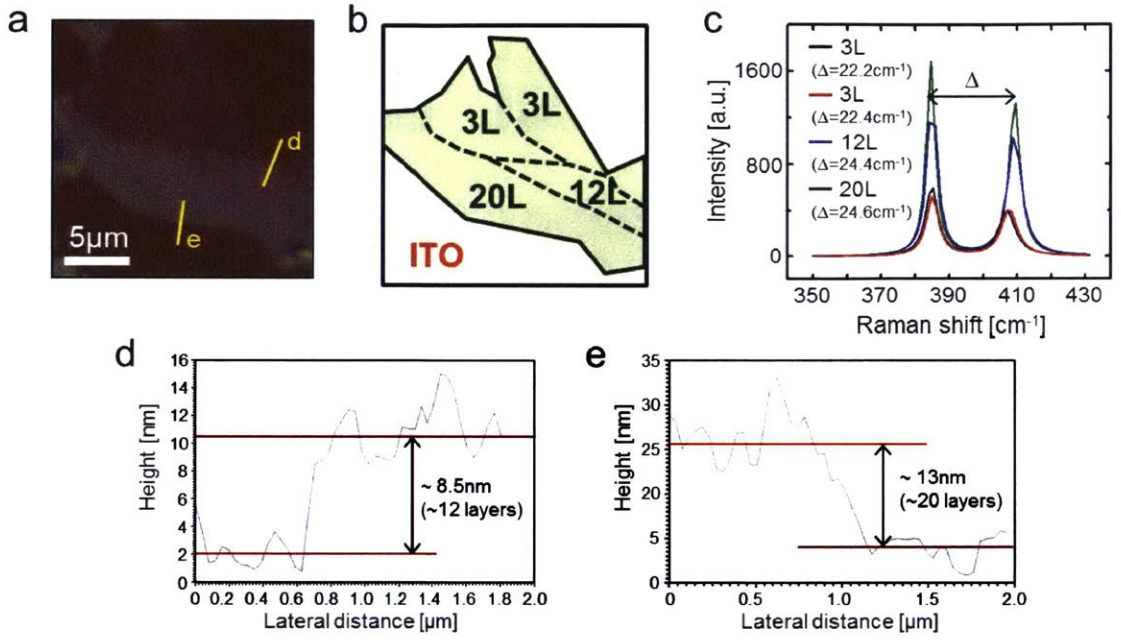

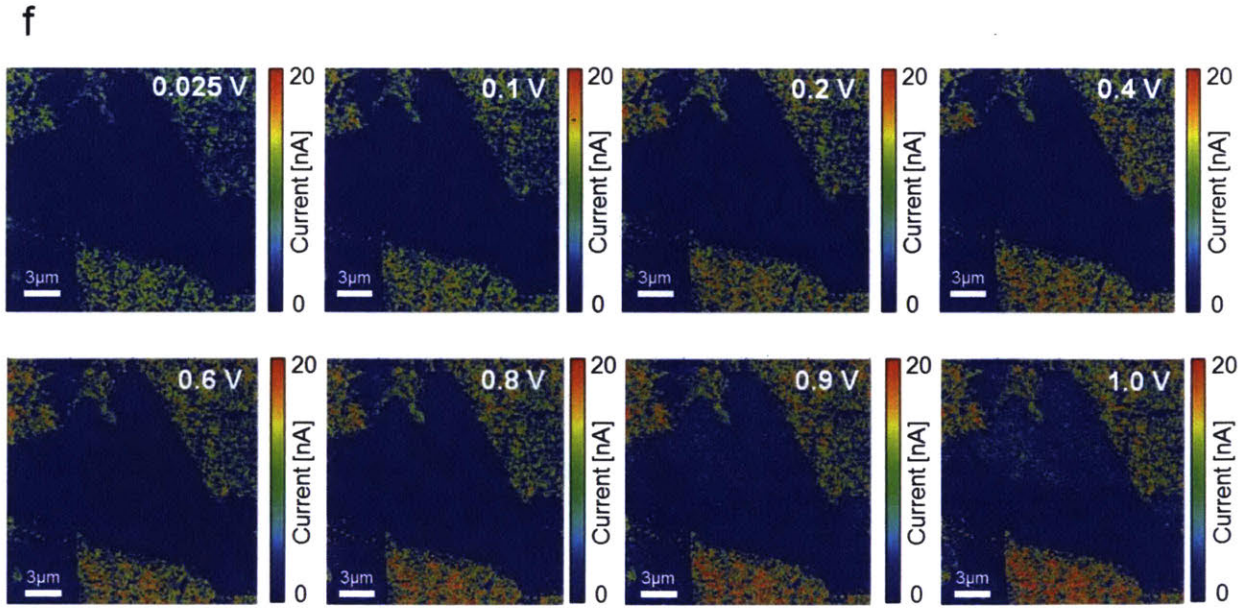

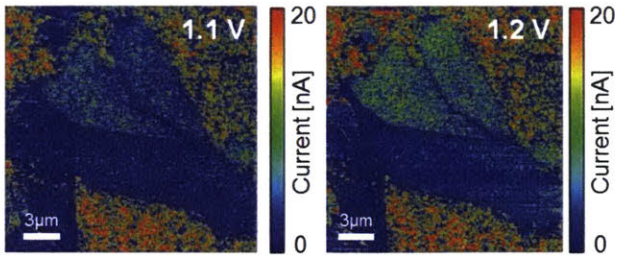

Figure 3-12: Additional Raman characterization, optical and C-AFM images in the dark. (a) An optical image of a MoS_2 crystal that consists of 3, 12 and 20-layer subregions deposited on ITO surface. (b) Schematic illustration of the MoS_2 nanosheet, indicating the regions of different layer numbers. (c) Representative Raman spectra taken at each region where the signature peak difference (Δ) was obtained to be 22.2, 22.4, 24.8 and 25.0 cm^{-1} for 3L, 3L, 12L and 20L, respectively. (d, e) A cross-sectional plot along the yellow line in (b) labelled as d and e, respectively. (f) Current maps taken by conductive AFM measurements under applied sample bias voltages of (b) 0.025V, 0.1V, 0.2V, 0.4V, 0.6V, 0.8V, 0.9V, 1.0V, 1.1V, and 1.2V.

We then produced quantitative *I-V* curves by taking averaged currents from each region with different thicknesses for all applied bias voltages (Figure 3-13), where the solid lines are fits to the FN tunneling model. The open blue triangles, purple squares and red circles indicate data points acquired from a different MoS_2 flake with 3L, 12L, and 20L regions under the same experimental conditions. Nonlinear *I-V* behaviour is obtained for all the regions, except 12L and 20L where weak or almost no current was recorded in the voltage range of our measurements.

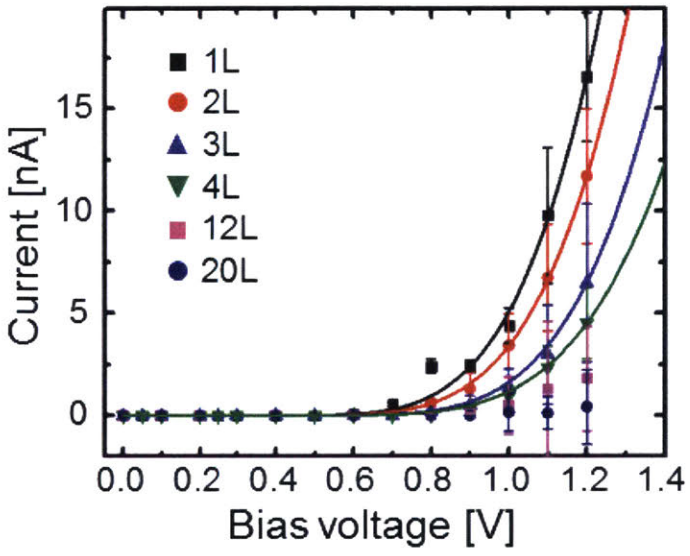

Figure 3-13: Averaged *I-V* data from regions of MoS_2 that are 1L, 2L, 3L, 4L, 12L, and 20L thick. The data for 1L to 4L are fit to the FN tunnelling model (solid lines). We note that the 12L and 20L regions are not from this particular MoS_2 nanoflake and were from another sample.

Figure 3-14 shows the extracted barrier heights (Φ_B) by fitting to the FN-tunneling model as a function of layer number from the MoS_2 flake shown in Figure 3-13. As layer number increases from 1L to 4L Φ_B increases gradually from 0.61 eV to 0.69 eV in a nonlinear fashion where the rate of increase is slowed that Φ_B of 3L reached close to that of 4L.

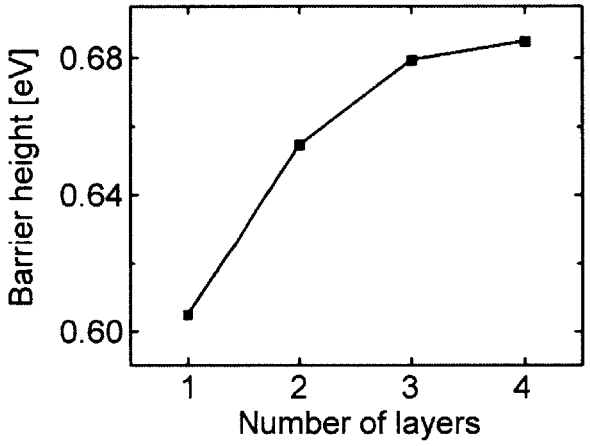

Figure 3-14: A plot of barrier heights as a function of MoS_2 layer number.

Figure 3-15 (a) shows the extracted tunneling barrier term, $\Phi_B^{3/2}d$, which includes contributions from both barrier height Φ_B and barrier width d by fitting to the FN tunneling model as a function of MoS_2 layer number. The scaling is well described by

$$\Phi_B^{3/2}d = an + b \qquad (7)$$

with $a = 0.26$ $eV^{3/2}$·nm and $b = 0.63$ $eV^{3/2}$·nm. As the layer number increases from 1L to 4L, $\Phi_B^{3/2}d$ increases in a linear fashion so that tunneling current is almost suppressed when MoS_2 becomes as thick as 20L.

Spatial variations in the electronic properties can be studied along with the topography of the sample because we have recorded local *I–V* characteristics across the material. Figure 3-15 (b) shows the spatially resolved map of local tunneling barrier, $\Phi_B^{3/2}d$, generated by fitting the recorded local *I-V* information to the FN tunneling model. The general increasing trend with layer number is clearly seen in this map, showing that our model is able to capture the layer-dependent transport behavior. We note that there is some small degree of spatial inhomogeneity that may result from variations in local barrier heights arising from impurities, defects, and fluctuations in tip-sample contact.

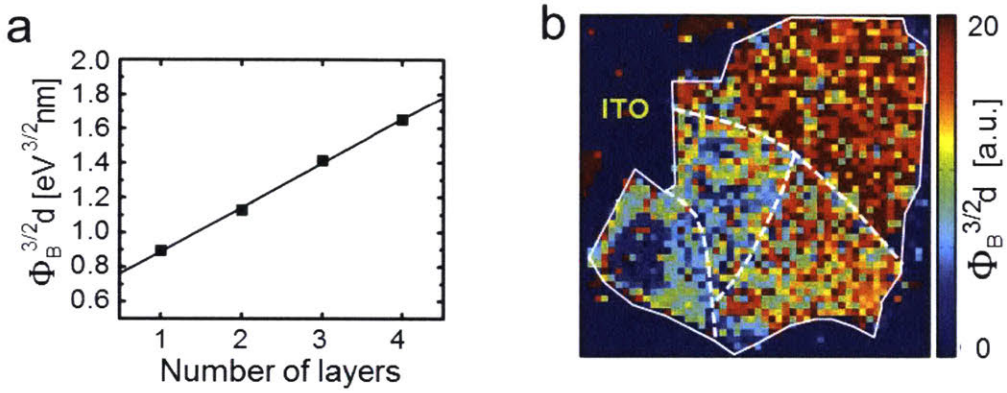

Figure 3-15: (a) A plot of the tunneling barrier ($\Phi_B^{3/2}d$) extracted using the FN tunneling model as a function of MoS_2 layer number *n*. There is a linear dependence of effective barrier on layer number. (b) Spatially resolved map of local tunneling barrier, $\Phi_B^{3/2}d$, obtained from local *I-V* data recorded where some degree of spatial variation is observed over the sample, but is relatively uniform within each layer thickness. The layer number dependence is again clearly seen.

In order to exclude the possibilities of tip degradation affecting the current measurements, a series of force–distance curves were measured directly before and after each of the 20 images appearing in Figure 3-11, as shown in the inset in Figure 3-4 (b). No noticeable change in the interaction between the tip and the sample was observed throughout the whole experiment, with the images staying stable and sharp, suggesting that the measurements were reliable and not deteriorated by tip degradation.

3.3.3 Layer-dependent Spectral Photoresponse of MoS_2

The layer-dependent optoelectronic properties of atomically thin MoS_2 have attracted increasing interest, and so we also explore the spectral response of photoconductivity as a function of MoS_2 layer number. We use the same MoS_2 nanosheet that was featured in Figure 3-10 for these optoelectronic measurements in order to directly compare the results to the dark current behavior. Figure 3-16 (a) shows a schematic illustration of the 1L, 2L, 3L, and 4L regions of this sample. Figures 3-16 (b-g) are spatially resolved maps of local photoresponse under λ= 550, 600, 650, 700, 750, and 800 nm laser illumination, where the photoresponse is defined as the difference between photocurrent (I_L) and dark current (I_D) normalized by illumination power:

$$\text{photoresponse} = \frac{(I_L - I_D)/q}{P_{inc}/hv} \qquad (8)$$

here q is electronic charge, P_{inc} the incident power, and hv the photon energy. These photoresponse maps are generated by subtracting a photocurrent map under illumination from a dark current map, and normalized by the incident laser power at each wavelength. All current images in both light and dark are shown in the Figure 3-17. A moderate bias of -0.6 V is applied throughout all the measurements to efficiently separate photoexcited charge carriers. In the photoresponse maps, a much stronger response is observed in the 1L region than in the 2L, 3L, and 4L regions as the illumination wavelength decreases from λ = 700 nm to 650 nm and below. In general, the photoresponse increases nonlinearly in all the regions with decreasing incident laser wavelength (increasing incident photon energy).

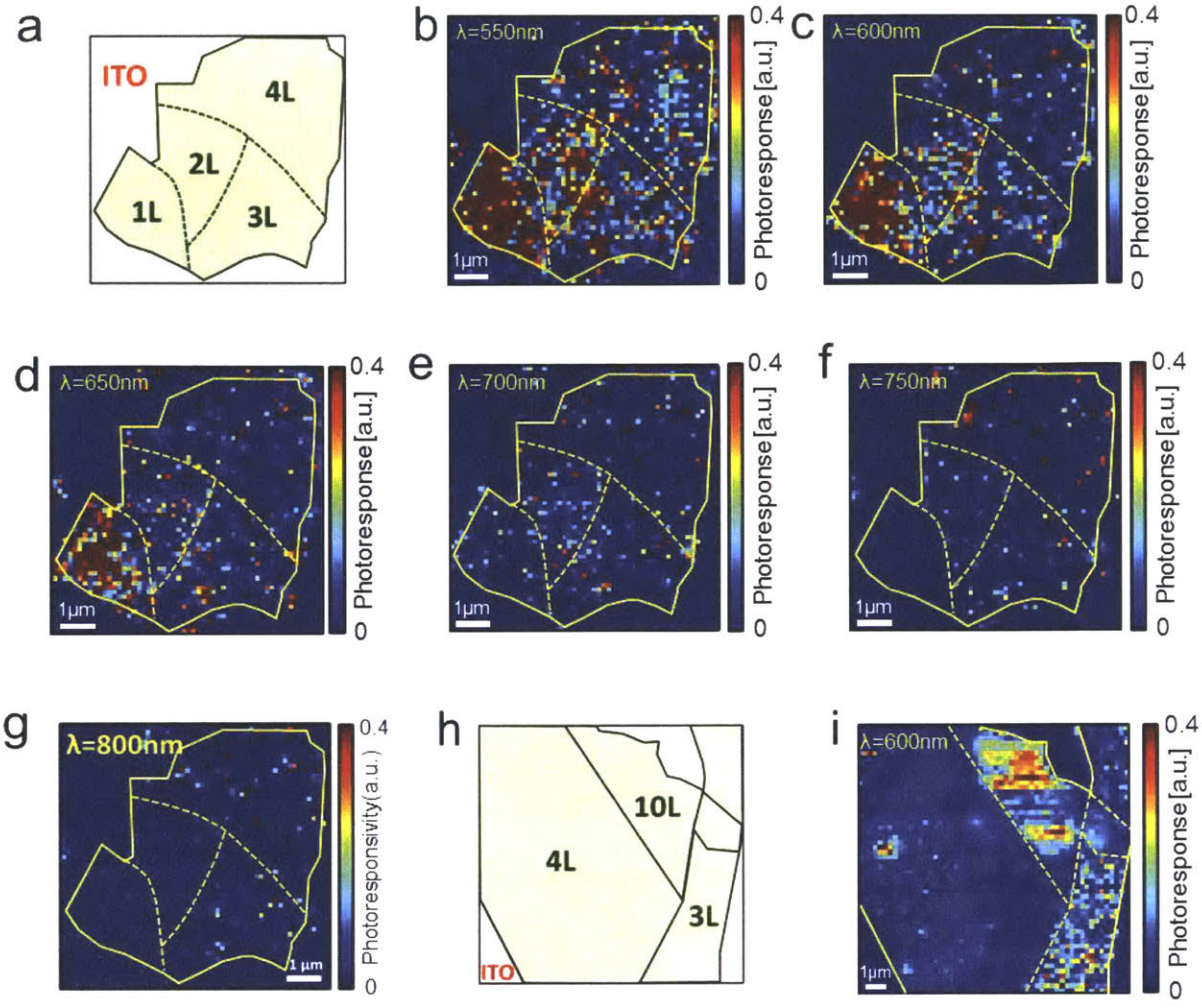

Figure 3-16: Spectral photoresponse in MoS_2 as a function of layer number. (a) Schematic illustration of the same MoS_2 nanosheet as shown in Figure 3-10, indicating the regions of different layer numbers. (b)-(g) Spatially resolved maps of local photoresponse obtained under laser illumination of (b) λ = 550 nm, (c) 600 nm, (d) 650 nm, (e) 700 nm, (f) 750 nm, and (g) 800 nm. Photoresponse was obtained by subtracting dark current images from illuminated current images and normalized by the incident laser power. (h) Schematic illustration of another MoS_2 flake that consists of 3L, 4L, and 10L regions. (i) Photoresponse map of the MoS_2 flake in (h) with applied bias of -0.6 V under laser illumination of λ = 600 nm.

The following are current maps in the dark and with illumination that were used to generate the spectral photoresponse maps presented in Figures 3-16.

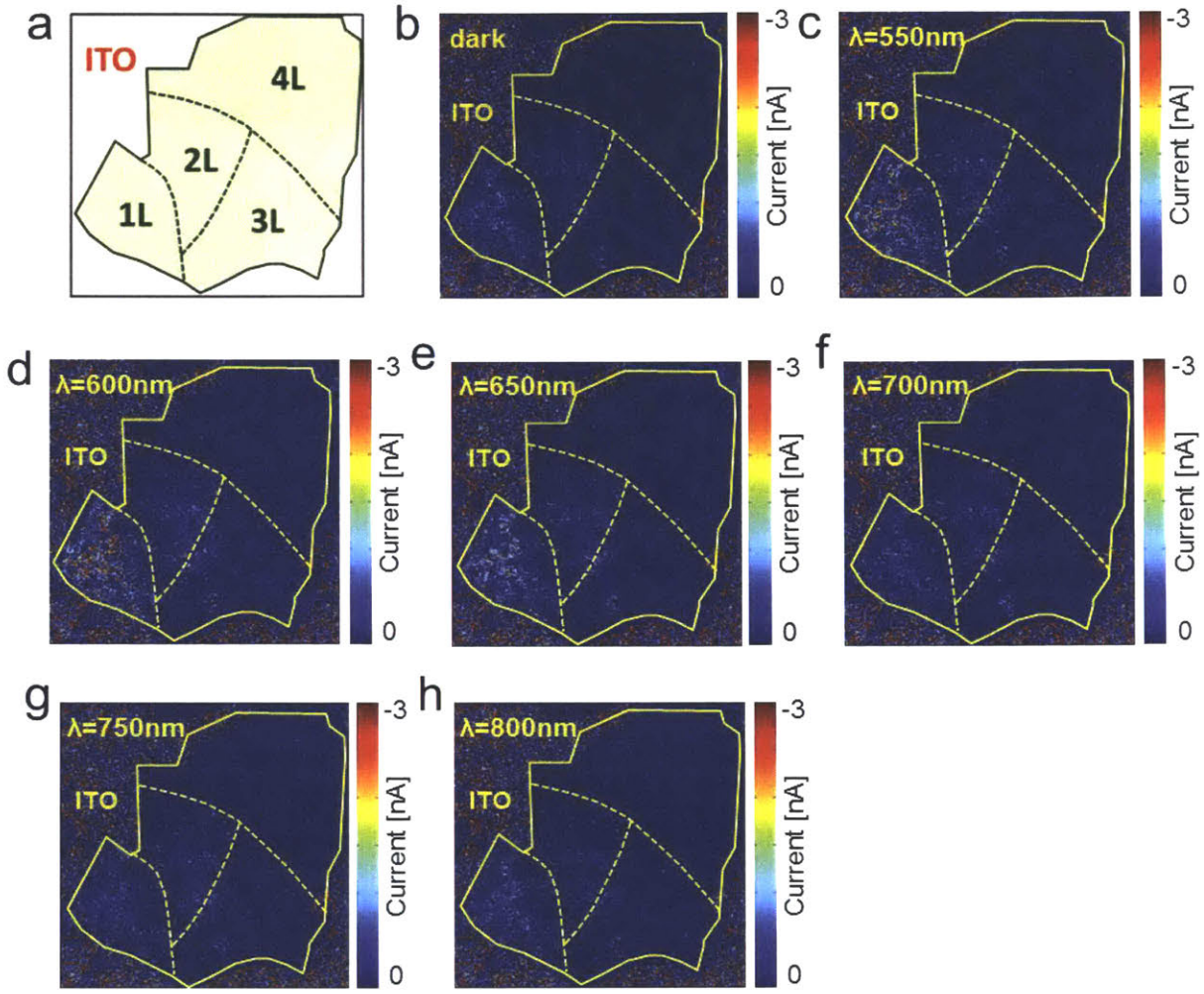

Figure 3-17: Current images under illumination. (a) Schematic illustration of the MoS_2 nanosheet, indicating the regions of different layer numbers. (b)-(h) Current maps generated by conductive AFM measurements (b) in the dark and under laser illumination of (c) λ = 550 nm, (d) 600 nm, (e) 650 nm, (f) 700 nm, (g) 740nm, and (h) 800 nm with an applied sample bias voltage of -0.6 V.

The below are characterizations and PCS-AFM and C-AFM images that were used to generate the spectral photoresponse map presented in Figure 3-16 (i).

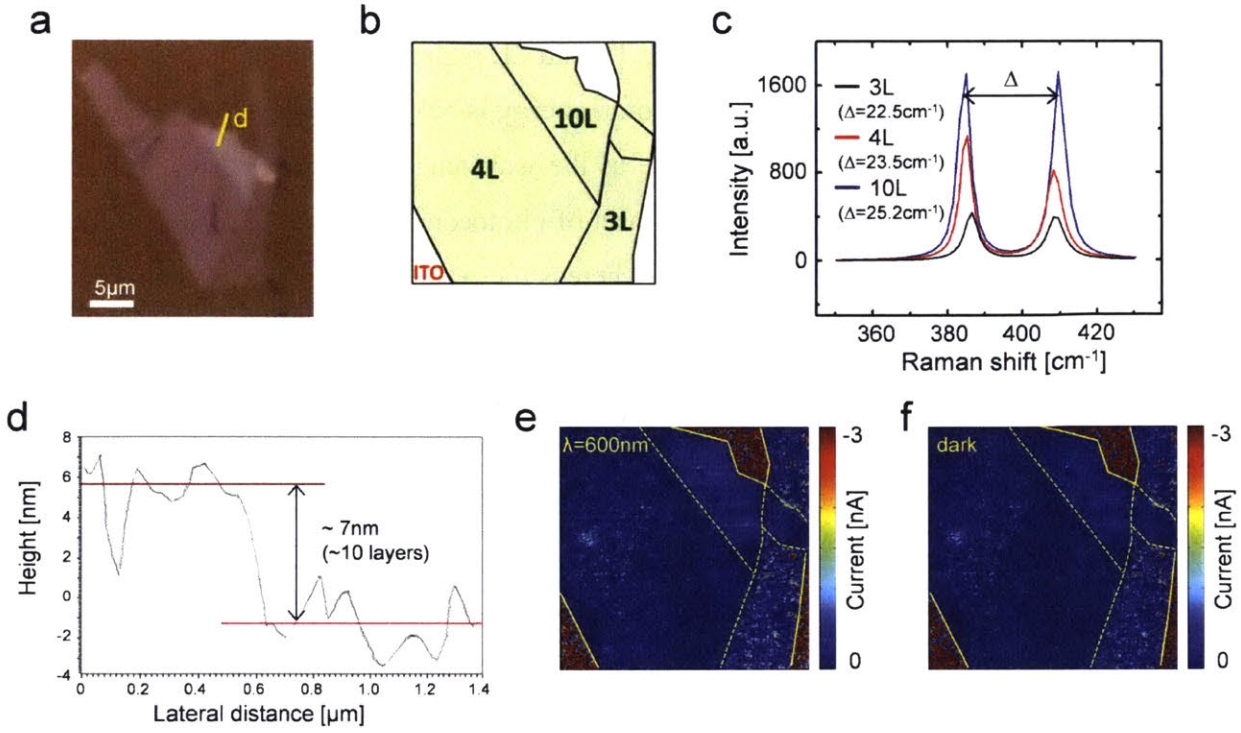

Figure 3-18: Additional Raman characterization, optical and C-AFM/PCS-AFM. (a) An optical image of an MoS_2 crystal that consists of 3, 4 and 10-layer subregions deposited on ITO surface. (b) Schematic illustration of the MoS_2, indicating the regions of different layer numbers. (c) Representative Raman spectra taken at each region where the signature peak difference (Δ) was obtained to be 22.5, 23.5 and 25.2 cm^{-1} for 3L, 4L, and 10L, respectively. (d) A cross-sectional plot along the yellow line in (a) labelled as d. (e-f) Current maps generated by conductive AFM measurements (e) under laser illumination of (c) λ = 600 nm and (f) in the dark with an applied sample bias voltage of -0.6 V that were used for generating the photoresponse map presented in Figure 3-15 (i).

The spectral photoresponse as a function of incident light wavelength was plotted by taking the average photoresponse over each thickness region, as shown in Figure 3-19 where error bars indicate the standard deviation. The inset of Figure 3-19 shows a magnification of the low photoresponse range. These spectral photoresponse curves demonstrate clear onsets of photoresponse at different wavelengths for each thickness, indicating the important role of the thickness-dependent band structures and tunneling barriers, which affect the photoexcitation and photocarrier collection efficiencies, respectively.

The 3L and 4L regions demonstrate weak photoresponse at λ = 800 nm (hv = 1.55 eV) while there is nearly no photoresponse in the 1L and 2L regions because they have very low levels of light absorption and because the photon energy is below the bandgap. The 2L curve shows a prominent increase in photoresponse as the wavelength is decreased to λ = 750 nm (hv = 1.65 eV) which agrees well with the onset of photoconductivity for 2L-MoS_2 reported in the literature occurring at about 1.6 eV,[44] whereas the response in 1L still remains at a very low level. However, as the illumination wavelength decreases further to λ = 650 nm (hv = 1.91 eV), now coinciding with bandgap of 1L MoS_2, the photoresponse dramatically rises by a factor of about 55. At that energy above the bandgap of all the layer numbers, the 1L still has markedly the highest photoresponse because it has a direct bandgap rather than an indirect one, making the photoexcitation process much more efficient.

The decreasing trend of photoresponse with the layer number can also be explained by increasing tunneling barrier lowering the carrier collection efficiency. Despite having the weakest light absorption, monolayer MoS_2 has the highest photoresponse because its effective tunneling barrier ($\Phi_B^{3/2}d$) at the metal–MoS_2 junction is the lowest, allowing for more efficient collection of photoexcited charge carriers via tunneling. The decreasing trend of spectral photoresponse with illumination wavelength can also be explained using the band diagram at the junction between MoS_2 and the metal tip shown earlier in Figure 3-8. In the reverse bias regime, excess energy is required for photoexcited charge carriers to overcome the barrier (solid arrow) or tunnel (dashed arrow) through the barrier formed at the junction in order to contribute to the photocurrent. Hence an incident photon with higher energy (*i.e.* shorter wavelength) can induce higher photoconductivity by transferring more excess energy to hot carriers, which then enhances the probability of overcoming or tunneling through the barrier. This picture of layer-dependent barrier changes is in accordance with the continued photoresponse enhancement we see in Figure 3-19 as the light wavelength decreases further from λ = 650 nm (hv = 1.91 eV) to 550 nm (2.25 eV), so that the photon energy is above the optical bandgap for all thicknesses.

The photoresponse appears to increase even further with the wavelength of illumination changing to λ = 550 nm from λ = 600 nm, which may be ascribed to a specific effective barrier height remaining at an applied bias of -0.6 V. In other words, Φ_B under applied bias

voltage of -0.6 V is close to the amount of excess energy that incident photons of λ = 550 nm can transfer to the hot carriers such that the probability for the carriers to surmount the barrier is substantially increased at this point. It is also important to note that the wavelength dependence of photoconductivity strongly suggests the enhanced current under illumination is predominantly due to interband photoexcitation in MoS_2 rather than absorption or heating effects in the metal tip.

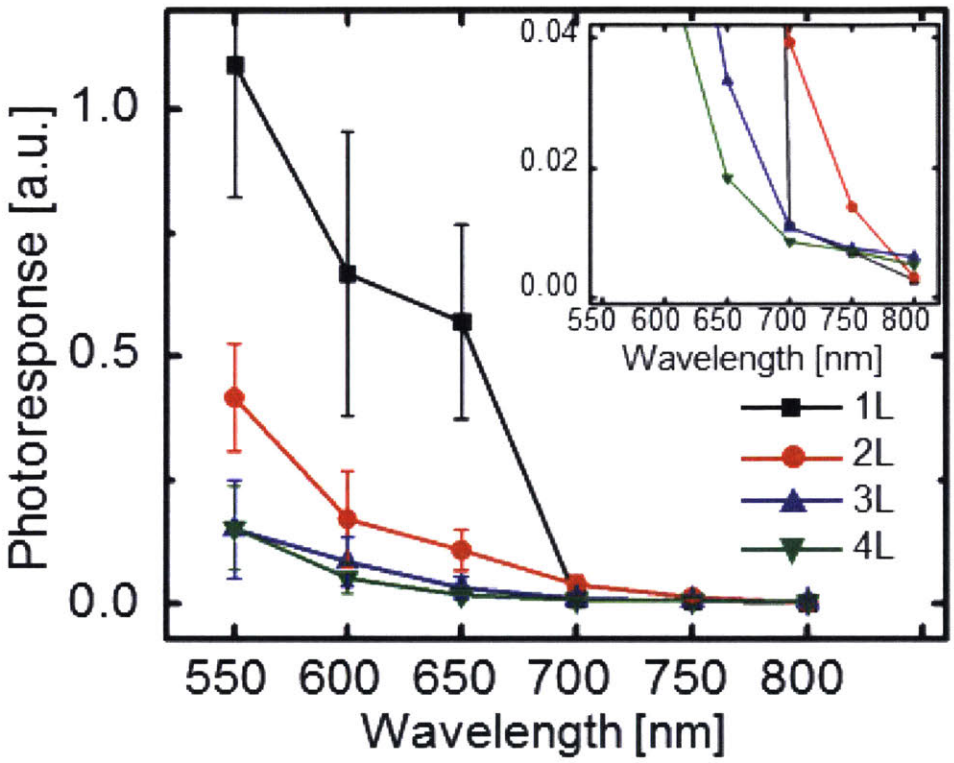

Figure 3-19: Spectral photoresponse in MoS_2 as a function of layer number: Plot of averaged photoresponse as a function of incident laser wavelength, showing prominent layer number dependence. Error bars indicate standard deviations. The inset shows the low photoresponse range, where 3L and 4L show weak photoresponse upon illumination at λ = 800 nm while nearly no response is observed in both 1L and 2L.

Additionally, an interesting increase in the photoresponse is observed as the thickness of MoS_2 increases from 4L to 10L. Figure 3-18 (b) shows a schematic of another MoS_2 crystal containing regions of 3L, 4L, and 10L. Figure 3-16 (i) shows the photoresponse map of this flake with applied bias of -0.6 V under laser illumination of λ = 600 nm. Detailed optical

microscopy, AFM topography and Raman analysis for layer number identification for this sample are provided in the Figure 3-18. The plot of photoresponse as a function of layer number in Figure 3-20 is generated from the samples in Figures 3-16 (a) and (h) (red and blue data points, respectively). The photoresponse decreases sharply from 1L, but then increases again at 10 L. The photoreponse ratio, normalized to the lowest measured value for 4L, is about 15 : 4 : 2 : 1 : 4 for thicknesses 1L : 2L : 3L : 4L : 10L. Zhang *et al.*[84] and Tsai *et al.*[85] studied photoresponse of single layer and few-layer MoS_2, respectively, using similar phototransistor device architecture where the photoresponse from single layer MoS_2-based device is observed to be higher than that from few-layer MoS_2, which is dissimilar from our observation due to the different junction characteristics and experimental conditions. However, a direct and accurate comparison between two separately fabricated devices across two full publications may hardly be made, illustrating the conventional difficulty in extracting authentic layer number properties for 2D materials when one must rely on device fabrication and operation. The layer number dependence that we show for MoS_2 in our current work corresponds to the 2D material studied under identical conditions on the same substrate, varying only the layer number systematically through n = 10.

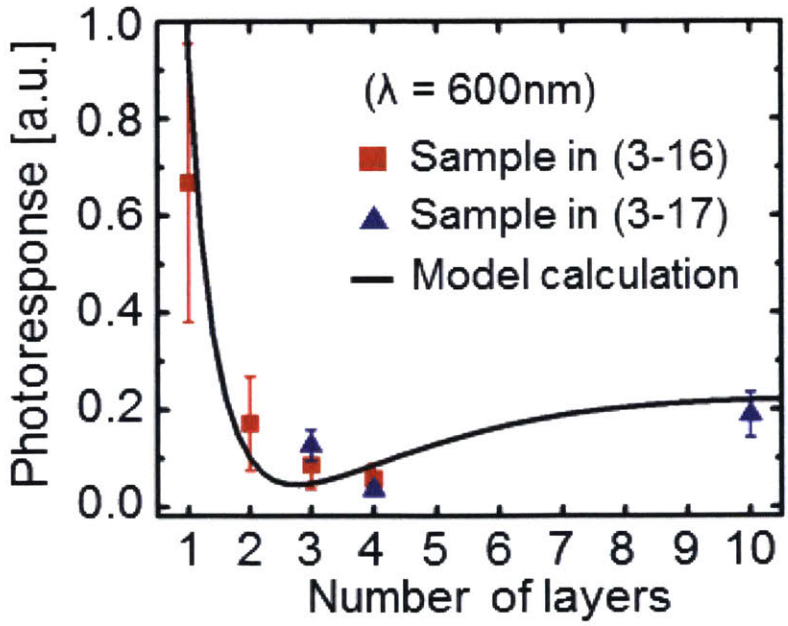

Figure 3-20: Plot of photoresponse as a function of MoS_2 layer number generated from the both samples where red and blue data points are extracted from samples in Figure 3-16 (a)

and (h), respectively. The photoresponse shows evident increase in 10L after experiencing continued decrease with layer number to the lowest in 4L. We model this behavior as the effect of changing effective barrier height and optical absorption as a function of layer number (solid line).

3.3.4 Competitive Photoresponse Model

We ascribe this non-monotonic photoresponse curve to the competition between carrier transport and light absorption contributions to the photocurrent. As the MoS_2 thickness increases, the tunneling barrier increases and causes the probability of excited charge carrier collection to decrease. At the same time, the amount of light absorption increases because there are more layers of material to absorb light, resulting in more carriers being photoexcited. Between 4L and 10L, enough additional hot carriers are created to lead to a rebound in the photoconductivity despite the larger tunneling barrier. We assume that light absorption is approximately proportional to layer number and that the photoexcited carriers increase the electrostatic potential of MoS_2 at the junction to provide an additional voltage, the effective bias voltage under illumination can be expressed as:

$$V_{\text{eff}} = V + n\alpha \tag{9}$$

where V denotes the applied bias, n the layer number and α the additional voltage generated due to photoexcitation of carriers in a single layer of MoS_2. We also allow for the fact that the effective barrier height may be altered under photoexcitation between the single particle (dark) and two particle (illuminated) experiments.

According to the FN tunneling model, the amount of current with and without illumination are

$$I_L = \gamma_L \frac{(V+\alpha n)^2}{n^2} \exp\left[-\beta_L n/(V+\alpha n)\right] \tag{10}$$

and

$$I_D = \gamma_D \frac{V^2}{n^2} \exp\left[-\beta_D n/V\right] \quad (11)$$

respectively, where we also define the variables γ and β with and without illumination as functions of the barrier height Φ_B as:

$$\gamma_{L/D} = (A_e q^3 m)/(8\pi h m^* \Phi_{B,L/D}) \quad (12)$$

$$\beta_{L/D} = (8\pi\sqrt{2m^*}\Phi_{B,L/D}^{3/2})/3hq \quad (13)$$

The photoresponse is then calculated as

$$\begin{aligned} \Delta I' &= \frac{I_L - I_D}{\gamma_L V^2} \\ &= \frac{(1+\alpha' n)^2}{n^2} \exp\left[-\frac{\beta'_L n}{1+\alpha' n}\right] - \frac{\gamma'}{n^2} \exp\left[-\frac{\beta'_L n}{\gamma'^{3/2}}\right] \end{aligned} \quad (14)$$

where we also define the terms $\gamma' = \gamma_D/\gamma_L \left(= \Phi_{B,L}/\Phi_{B,D}\right)$, $\alpha' = \alpha/V$, and $\beta'_{L/D} = \beta_{L/D}/V$.

The photoresponse calculated by this model is shown as the black curve in Figure 3-20 as a fit to the experimental data (with fitting parameters $\gamma' = 1.5$, $\beta'_L = 0.2$ and $\alpha' = 0.5$). The fit supports our model that photoresponse plummets with increasing layer number due to increased tunneling barrier up to about 3L, but rebounds as the layer number further increases because of increased light absorption. For higher values of n, the photoresponse saturates at a constant value. The results suggest an FN tunneling barrier that increases 50% upon illumination, but in a device that otherwise behaves the same in the dark state. Possible origins for this 50% increase may be photothermal, since absorption of the incident energy can result in a lattice deformation that can increase the tunneling distance (d) and increase the effective barrier.

3.3.5 Photoresponse Dependence on an Applied Bias Voltage

This analysis can be expanded to interpret the strong dependence of the photocurrent on the applied voltage. Figures 3-21 show the photoresponse maps of the sample shown in Figure 3-16 (a), in both forward (a-f) and reverse voltage regimes (g-i). The bias voltages are varied while the illumination is maintained at λ = 600 nm.

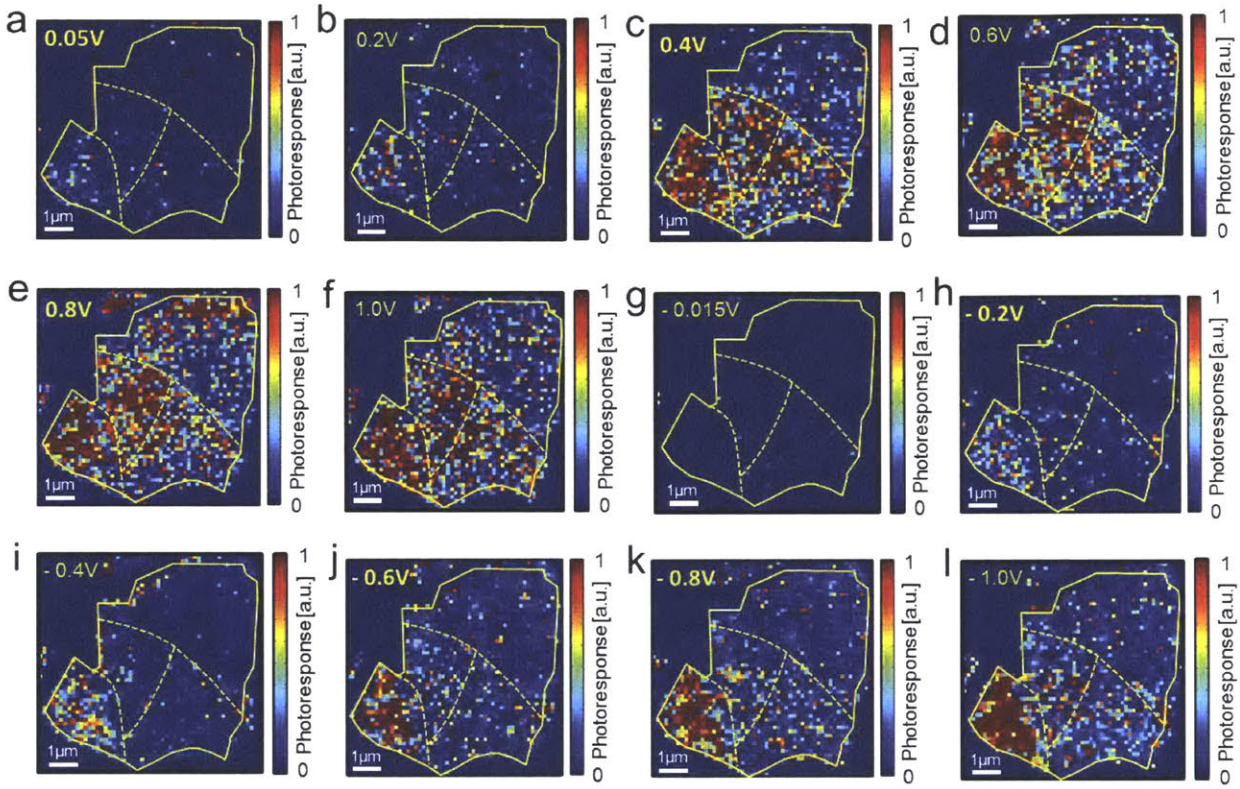

Figure 3-21: Dependence of photoconductivity on bias voltage. Photoresponse maps of the flake at forward bias voltages of (a) 0.05 V, (b) 0.2 V, (c) 0.4 V, (d) 0.6 V, (e) 0.8 V, and (f) 1.0 V, and reverse bias voltages of (g) -0.015 V, (h) -0.2 V, (i) -0.4 V, (j) -0.6 V, (k) -0.8 V, and (g) -1.0 V under illumination of λ = 600 nm.

Additional current images in dark and light that are used to generate photoresponse maps are shown in Figure 3-22.

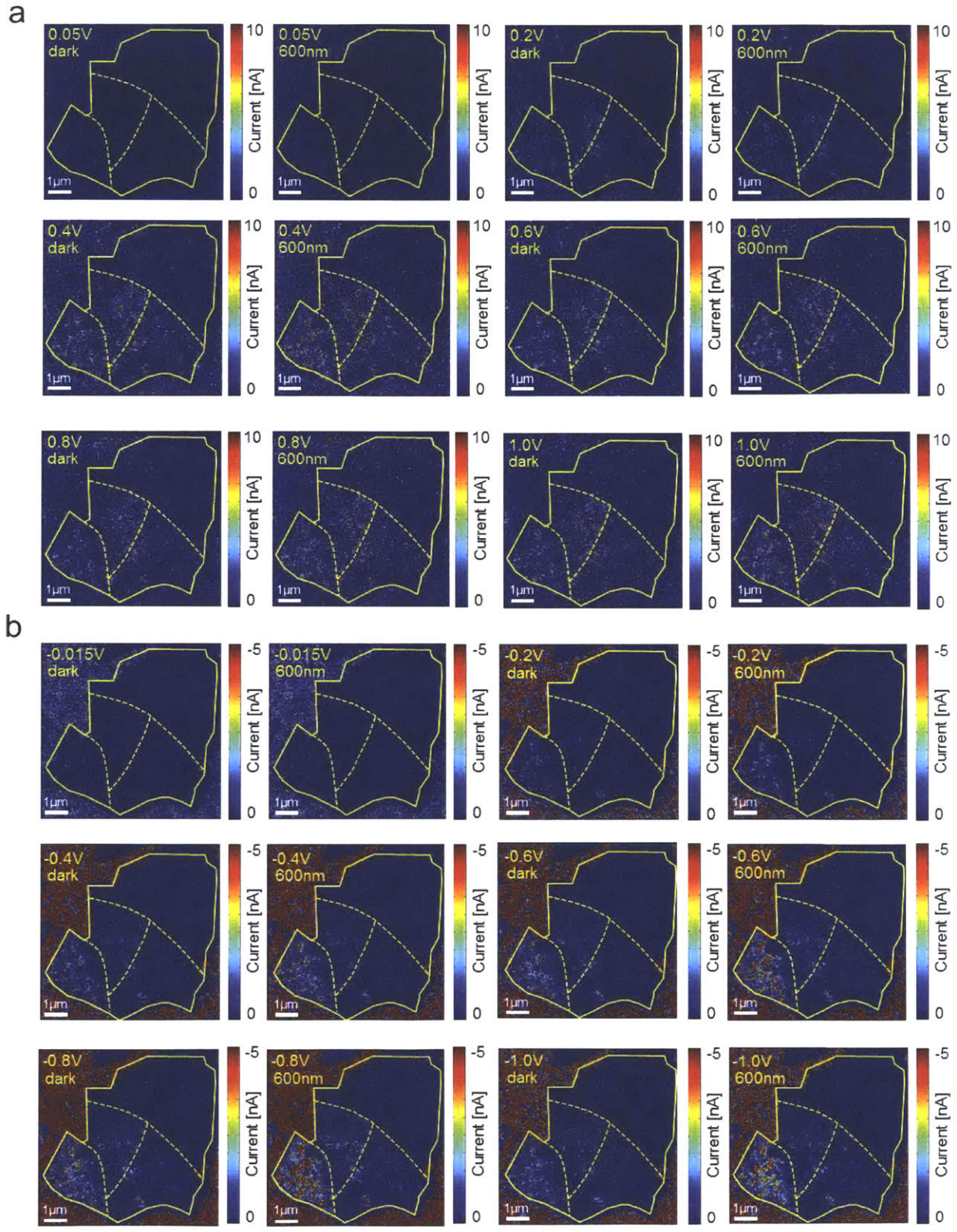
a
0.05V dark
0.05V 600nm
0.2V dark
0.2V 600nm
0.4V dark
0.4V 600nm
0.6V dark
0.6V 600nm
0.8V dark
0.8V 600nm
1.0V dark
1.0V 600nm
b
-0.015V dark
-0.015V 600nm
-0.2V dark
-0.2V 600nm
-0.4V dark
-0.4V 600nm
-0.6V dark
-0.6V 600nm
-0.8V dark
-0.8V 600nm
-1.0V dark
-1.0V 600nm
Current [nA]
10
0
-5
1μm

Figure 3-22: Dependence of photoconductivity on bias voltage. Current maps generated by PCS-AFM measurements under laser illumination of λ = 600 nm and in the dark with an applied (a) forward and (b) reverse bias voltage applied that were used to generate the photoresponse maps presented in Figure 3-21.

The plot of photoresponse as a function of voltage is shown in Figure 3-23 with the error bars indicating standard deviations. We note that the photoresponse in forward and reverse bias regimes shows barrier symmetry for 1L but noticeable asymmetry is observed for 2L, 3L, and 4L.

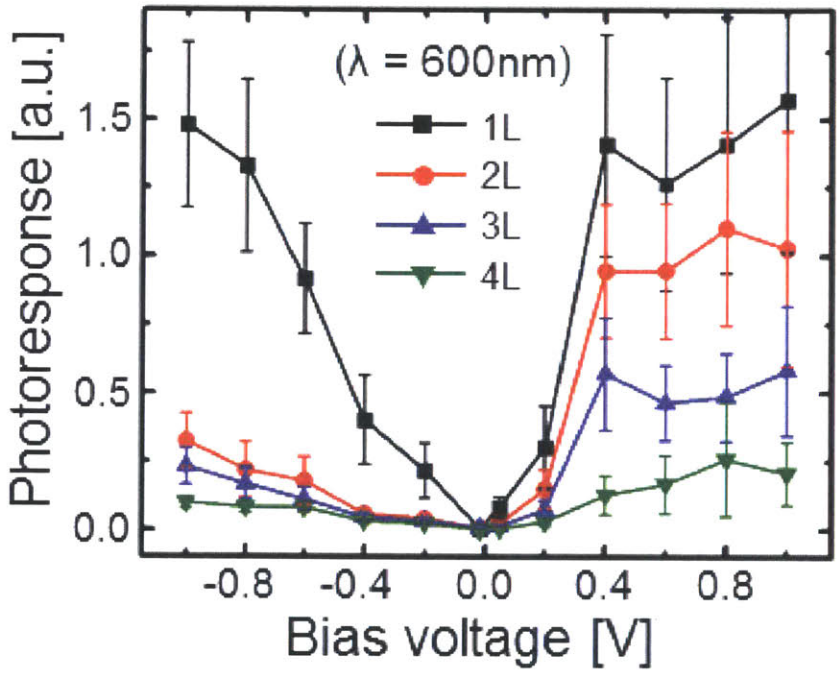

Figure 3-23: Dependence of photoconductivity on bias voltage and incident laser power: Plot of photoresponse *versus* voltage with the error bars indicating standard deviations. We observe barrier symmetry for 1L regions but significant asymmetry is observed for 2L, 3L, and 4L regions.

In general, the photoresponse is stronger in forward than in reverse bias, which is likely attributed to the different barriers that form at the MoS_2–metal tip and MoS_2–ITO junction. By applying forward bias, as depicted in Figure 3-8, no appreciable barrier forms at MoS_2–ITO junction, thereby enabling efficient electron collection at the ITO electrode while a large barrier forms towards the opposite direction from MoS_2 to the metal tip. The photoresponse

rises sharply with voltage until around 0.4 V and becomes relatively flat, without showing notable increase afterwards in all the regions. It may be because the 0.4 V bias voltage provides enough energy to separate and collect most of the photoexcited charge carriers. In reverse bias, however, separated charge carriers face a barrier at the MoS_2–metal tip junction that needs to be thermally overcome or tunneled through, and the barrier that remains in the voltage range of our experiment can lead to the observed forward-reverse asymmetry. As the applied voltage becomes more negative, enhanced thermal emission because of the reduced barrier height competes with the lowered tunneling probability caused by the widened barrier. However, because the 1L MoS_2 is so thin, the impact of bias on the tunneling probability is minimal such that at around -0.8 V the photoresponse reaches close to the saturation level of the forward bias. In contrast, the 2L, 3L, and 4L photoresponses remain below their forward bias values due to the increased barrier thickness.

3.3.6 The Effect of Illumination Power: Photocarrier Dynamics

The influence of illumination power on photoresponse is shown in the photoresponse maps of Figure 3-24 and the plot in Figure 3-25. The laser power was varied for a constant wavelength of λ = 550 nm and applied bias of -0.6 V. In general, we observe a clear increasing trend in photoconductivity for all MoS_2 thickness regions as the power increases, although some degrees of spatial irregularities exist due to local variability of electrical properties of the junction.

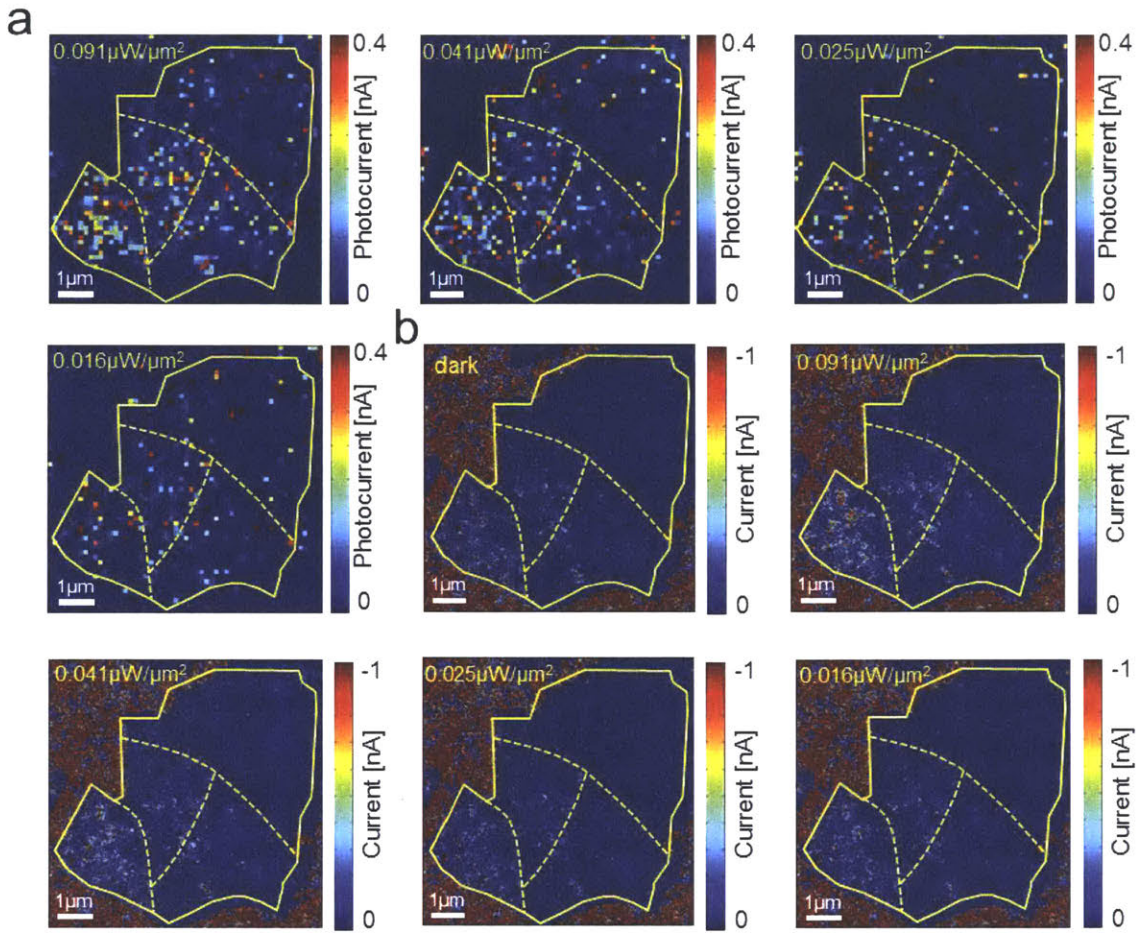

Figure 3-24: Dependence of photoconductivity on incident laser power. (a) Photocurrent maps under varying incident laser power density of 0.091μW/ μm^2, 0.041μW/ μm^2, 0.025μW/ μm^2, and 0.016μW/ μm^2 (λ = 550 nm). (b) Current maps generated by PCS-AFM under varying incident laser power density of 0.091μW/ μm^2, 0.041μW/ μm^2, 0.025μW/ μm^2, and 0.016μW/ μm^2 with an applied bias of -0.6V that were used to generate the photocurrent maps shown in (a).

The photocurrent shows a sublinear dependence on the incident laser intensity, where power exponents range from 0.56 to 0.67 (see Figure 3-25).

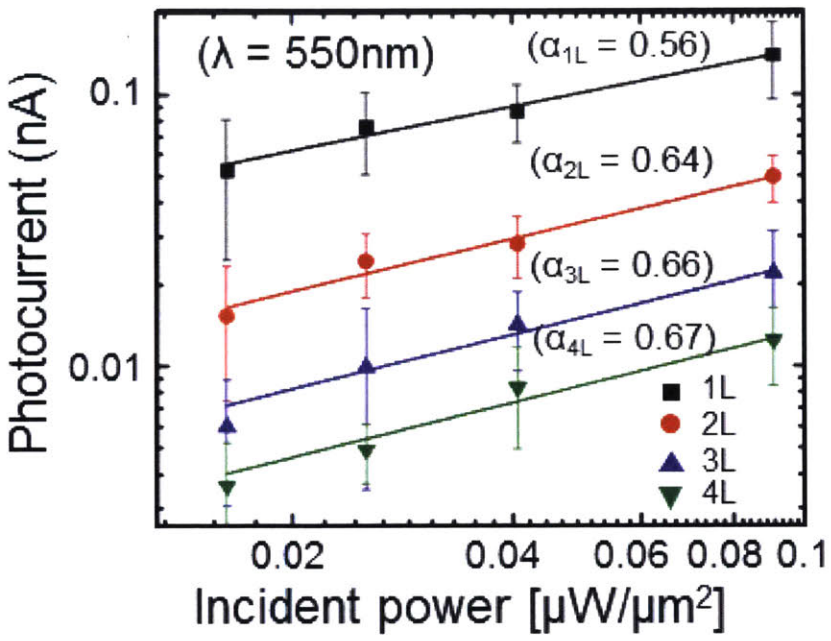

Figure 3-24: Dependence of photoconductivity on incident laser power: Log-log plot of photocurrent as a function of incident laser power density where straight lines are fit to the power law. A sublinear dependence on the incident laser intensity is observed, where power exponents range from 0.56 to 0.67.

We assign this nonlinear scaling of the photocurrent to the recently identified rapid exciton-exciton annihilation (EEA) in atomically thin MoS_2 crystals.[86] The exciton density can be expressed with loss terms by the EEA and exciton dissociation, and a generation term which is dependent on the laser power and the layer number:

$$\frac{dN}{dt} = -k_1 N^2 - k_2 N + G \qquad (15)$$

$$I_{pc} = k_2 N \qquad (16)$$

Where k_1 is the EEA rate constant, k_2 is the free carrier generation rate (dissociation of exciton), and I_{pc} denotes photocurrent. At steady-state from (15):

$$N = -\frac{1}{2}\frac{k_2}{k_1} + \sqrt{\frac{1}{4}\left(\frac{k_2}{k_1}\right)^2 + \frac{G}{k_1}} \qquad (17)$$

Where $G = I_0 \varepsilon(n) \Delta dn$ where I_0 denotes the incident power, $\varepsilon(n)$ $(= \varepsilon_0 n^{-4})$ the layer dependent extinction coefficient at 550 nm which demonstrates this -4 scaling for near band edge absorption, n is the number of layers, and Δd the thickness of a single layer. This model including the EEA effects generates a successful fit to the sublinear laser power-dependent photocurrent data, as represented by solid lines in the Figure 3-25, where ε scales as $1/n^4$. Adopting an EEA rate constant of $k_1 = 4.3 \times 10^{-2} \text{cm}^2\text{s}^{-1}$ from Sun *et al.*,[86] k_2 and ε_0 are extracted to be $3.3(\pm 0.2) \times 10^{1} \text{s}^{-1}$ and $1.3(\pm 0.2) \times 10^{2} \text{nm}^{-1}$, respectively. The tight confidence intervals serve to experimentally validate the exciton population balance.

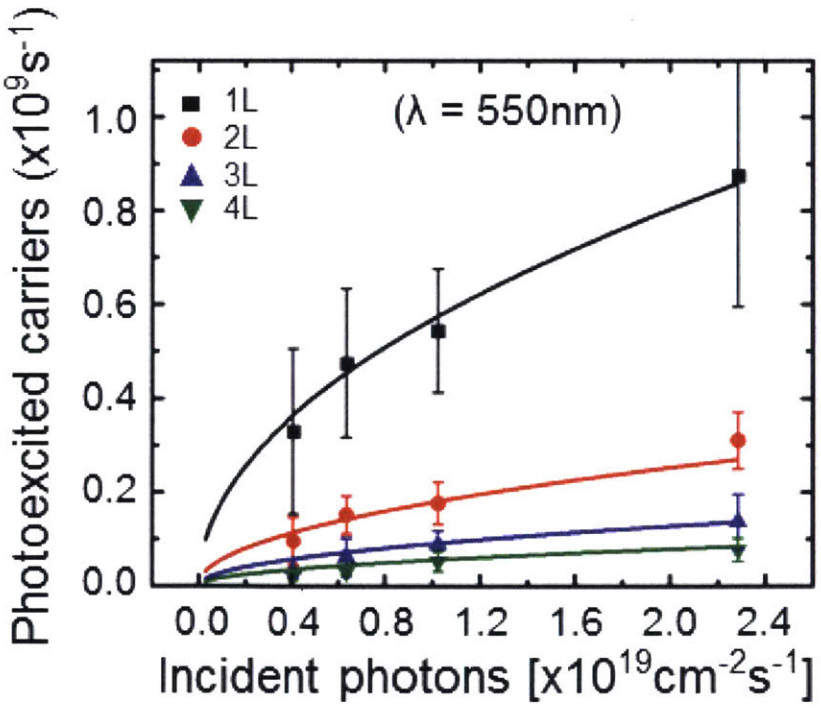

Figure 3-25: Dependence of photoconductivity on incident laser power: A plot of photocurrent as a function of incident laser power density where solid lines are fit to the suggested model.

3.3.7 Spatial Analysis: 2D Fast Fourier Transforms (FFTs)

We performed additional spatial analysis of the topography and current images, as shown in Figure 3-26, for the same MoS_2 flake that was featured in Figure 3-10. Two particular regions of the sample outlined in white squares are analyzed further: one indicating a region of bare ITO, and the other a region where a thin flake of MoS_2 is covering the ITO substrate. The topographic images in both regions (Figures 3-26 (c) and 5(e)) are quite similar, with the grains or terraces of the ITO showing through the atomically thin MoS_2. The 2D fast Fourier transforms (FFTs) of these topographic images (Figures 3-26 (g) and 5(i)) are also quite similar, with most of the intensity focused in an approximately round region in the middle, indicating anisotropic features in the original images. However, the FFT of the ITO-only current image (Figure 3-26 (h)) has more intensity along the vertical direction, suggesting inhomogeneity in the horizontal direction, and the FFT of the ITO+MoS_2 current image has significantly higher intensity in the vertical direction. While there is good spatial correlation between the current and the topography for ITO alone, suggesting the currents are closely associated with the grains in the ITO, there is much less correlation in the ITO+MoS_2 case. We attribute these observations of inhomogeneity in the horizontal scan lines in Figure 3-26 (f) to intermittent or imperfect contact between the MoS_2 flake and the rough ITO substrate. There is enough contact between them for the topography of the ITO to show through the atomically thin layer, but small shifts or movements between the tip, MoS_2 flake, and ITO can lead to fluctuations in the current. Because the MoS_2 sheet is so thin, we also attribute these fluctuations to crinkling of the sheet as the tip moves across in contact mode imaging.

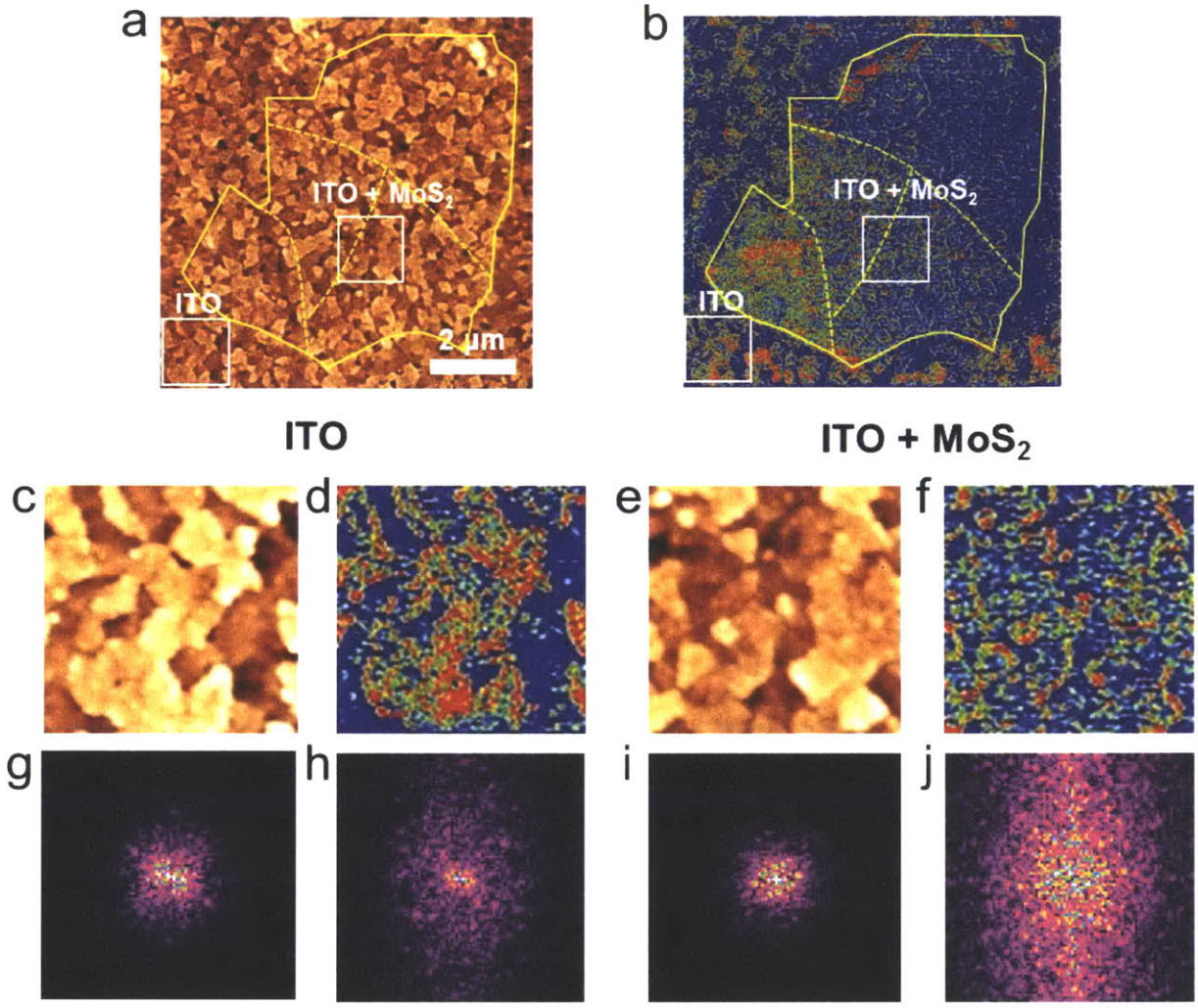

Figure 3-26: Spatial analysis of topography and current images. (a) Topographic height AFM image of the MoS_2 flake shown in Figure 3-10. (b) Current image of the same flake, at sample bias of 1.2 V. The regions in squares marked ITO and ITO+MoS_2 are regions of bare ITO and ITO covered by the MoS_2 flake, respectively. The ITO-only region is enlarged in (c)-(d) and the ITO+MoS_2 region in (e)-(f). The topographic images (c) and (e) appear quite similar. The current image (d) shows spatial correlation with the grains or terraces in (c), but the current image (f) shows less clear correlation with (e), and has more inhomogeneity in current. (g)-(j) 2D fast Fourier transforms (FFTs) of the images in (c)-(f). The FFT patterns of the topographic images (g) and (i) are quite similar, and show a relatively isotropic distribution of features. The FFT patterns of the current images (i) and (j) show differences: the FFT of ITO+MoS_2 has a lot more intensity in the vertical direction, suggesting increased inhomogeneity in the horizontal direction of the current image, corresponding to the fast scan

direction. We attribute the current inhomogeneity to small amounts of crinkling in the MoS_2 flake under the tip as it scans across the surface, resulting in more variable electrical contact.

3.4 Conclusion

In conclusion, we have studied the layer number dependent dark and photocurrent behavior at the nanometer scale junction between ultrathin MoS_2 nanosheets and metal (PtIr) using C- and PCS-AFM measurements. We measure rectifying diode characteristics, revealing that the carrier transport at the junction is successfully explained by the FN-tunneling model and thermionic emission assisted by tunneling in the forward and reverse sample bias regimes, respectively. Extracted barrier heights are lower by about 0.3 eV than those predicted by the traditional metal-semiconductor contact model possibly due to partial Fermi level pinning by the formation of an interfacial dipole and gap states, and an effective tunneling barrier scales linearly with MoS_2 layer number. An outstanding photoresponse was observed in 1L MoS_2 due to its ultrathin energy barrier at the junction with the metal. Interestingly, the photoresponse as a function of increasing layer number displays the competing effects of photoexcitation efficiency dropping as the bandgap decreases and changes to indirect, and the light absorption increasing. The photoresponse symmetry in 1L and asymmetry in 2, 3, and 4L as a function of bias polarity further corroborates the picture of subtle contributions from both the thermal emission and field-effect tunneling to photocurrent transport. The sublinear power dependence of photocurrent is observed, suggesting the possible presence of trap states at the MoS_2–metal junction. Based on the fundamental understanding of the layer number dependence of electronic and optoelectronic behavior at the nanoscale MoS_2–metal junction that we have achieved in this work, the selection of the metal and controlling the MoS_2 layer number will enable a wide range of electrical property modulation that will be beneficial for future device applications.

4. Layer Number Dependence of MoS_2 Photoconductivity Using Photocurrent Spectral Atomic Force Microscopic

4.1 Introduction

The significant interest and research effort devoted to discovering two-dimensional (2D) crystals beyond graphene have resulted in substantial progress in the fundamental understanding of transition metal dichalcogenides (TMDCs) with important implications for the design of future nanoelectronic components.[3, 59] Many TMDCs possess unique electronic and optical properties including permanent band gaps as well as transitions from indirect to direct characteristic originating from 2D quantum confinement. These properties have motivated their exploration as active materials for a broad range of electronic[36, 37, 87-89] and optoelectronic[35, 38-41, 90, 91] applications. Materials for such applications require the development of versatile junctions such as 2D/metal[92-94] or 2D/2D Schottky[95-97] and, in particular, p-n junctions.[98-100] Traditional doping methods such as dopant diffusion and ion-implantation used for conventional bulk semiconductors are not generally suitable for atomically thin 2D layers due to unavoidable crystal damage, so significant effort has been focused on achieving vertical van der Waals p-n heterostructures of dissimilar TMDCs of n- and p-types.[99, 101, 102] While the vertical heterostructure exhibits both characteristic rectifying behavior and photovoltaic response, the transfer process used to form a vertical p-n junction is insufficiently robust because it introduces unwanted trap states, lattice mismatch, and spatial inhomogeneity. Recently, a promising alternative route in the form of a monolayer in-plane p-n junction was developed *via* a two-step epitaxial growth of p-type WSe_2 and n-type MoS_2. By removing the laborious and unreliable transfer process of vertical heterojunctions and significantly improving the interface quality, the in-plane heterojunction shows tremendous promise for the realization of TMDC monolayer components in future nanoelectronics.[103] Although this seamless WSe_2-MoS_2 lateral heterojunction crystal showed clear rectifying behavior, photoresponse, and photovoltaic effects, many questions about the

spatial dependence of nanoscale local electrical and optoelectronic properties—not only throughout the homogeneous crystals but at the lateral junction regions—remain unaddressed.

In this section, we answer these important questions using conductive and photocurrent spectral atomic force microscopy (C-AFM and PCS-AFM) measurements to obtain the spatially resolved transverse electrical properties of the monolayer WSe_2-MoS_2 lateral p-n heterostructures both in the dark and under laser illumination. In Chapter 3, we have previously demonstrated that C- and PCS-AFM are versatile tools to conveniently and efficiently interrogate layer-dependent electronic and optoelectronic characteristics in a MoS_2 crystal containing regions of different thicknesses, enabling direct characterization and comparison of the different layer regions without the complexities associated with fabricating and testing of different individual field-effect transistor devices.[104] By performing current imaging using a PtIr-coated conductive tip on an ultrathin nanosheet that includes homogeneous crystals of WSe_2 and MoS_2, and a lateral junction region in between, we can form many thousands of WSe_2/MoS_2/the junction–metal contact points during imaging and directly compare their local properties at the same time under identical experimental conditions with the nanoscale spatial resolution. Therefore, in this work, we study for the first time spatial dependence of electronic and optoelectronic characteristics of a monolayer WSe_2-MoS_2 lateral heterostructure *via* current imaging of the nanosheets that can fit within a single AFM image in both forward and reverse bias regimes using the C- and PCS-AFM.

By taking consecutive current images while changing bias voltages, we observe a clear diode characteristic that is in agreement with our prior observations in which carrier transport at the nanoscale interface between the nanosheets and metal tip is dominated by tunneling events.[96] WSe_2 and MoS_2 exhibit an opposite trend due to their dissimilar doping types that lead to a uniquely shaped Schottky barrier at the interface with the metal tip. The lateral junction shows a comparatively lower conductivity than the homogeneous regions which can be attributed to the fact that the band edge energies change over the depletion region, consequently increasing the effective barrier height. In addition, we investigate the spatially resolved photoresponse of the heterostructure, which shows a noticeable dependence on the voltage applied through the tip. By changing the polarity and magnitude of the applied voltage, the photoresponse pixels in part of the heterostructure were selectively switched on

and off, demonstrating a hyper-resolution switchable photodiode array. This experimental technique should aid in the realization of novel optoelectronic devices for regioselective photodetection and imaging with high resolution. Overall, the insight into the charge carrier transport mechanisms in the heterostructure provides critical information to design and further engineer electronic and optoelectronic devices based on atomically thin quantum confined 2D lateral heterojunctions at the nanoscale level.

4.2 Experimental Methods

In order to study carrier transport in the dark, a monolayer lateral WSe_2-MoS_2 heterostructure was synthesized on *c*-plane sapphire substrates by sequential chemical vapor deposition (CVD) of WSe_2 and MoS_2, followed by transfer onto a conductive indium tin oxide (ITO)-coated glass substrate.[103, 105, 106]

The C-AFM and PCS-AFM measurements were conducted using PtIr-coated conductive probes in contact imaging mode. During the measurements, the conductive tip is held at ground while the bias voltage was applied to the ITO substrate as the other electrode. Throughout this chapter, we refer to forward (reverse) bias when the ITO electrode is positively (negatively) biased relative to the grounded conductive tip.

4.2.1 Synthesis of WSe_2-MoS_2 Lateral Heterostructures

Single crystalline WSe_2 monolayer was grown on c-plane sapphire substrates by chemical vapor deposition. The WO_3 power (0.6 g) was placed in a quartz boat located at heating zone center of the furnace. The Se power was placed in a separate quartz boat at the upper stream side of the furnace and the temperature was maintained at 260 °C during the reaction. The sapphire substrate was put at the downstream side, just next to WO_3 powders. The gas flow was brought by an Ar/H_2 flow (Ar = 90 sccm, H_2 = 6 sccm), and the chamber pressure was controlled at 20 Torr. The center heating zone was heated to 925 °C and kept for 15min for synthesis. Then, the furnace was naturally cooled down to room temperature. The WSe_2 sample was then put into a separate furnace for the 2nd step MoS_2 growth. The setup for

MoS_2 synthesis is that for WSe_2, where the WSe_2 sample was put at the downstream side and the distance between sample and MoO_3 powders was 9 cm for best Mo and S sources ratio to have WSe_2/MoS_2 heterojunction. The gas flow was brought by an Ar flow (70 sccm), and the chamber pressure was controlled at 40 Torr. The center zone of furnace and S source were heated to 755 °C and 190 °C and hold 15 min for synthesis, and then naturally cooled down to room temperature.

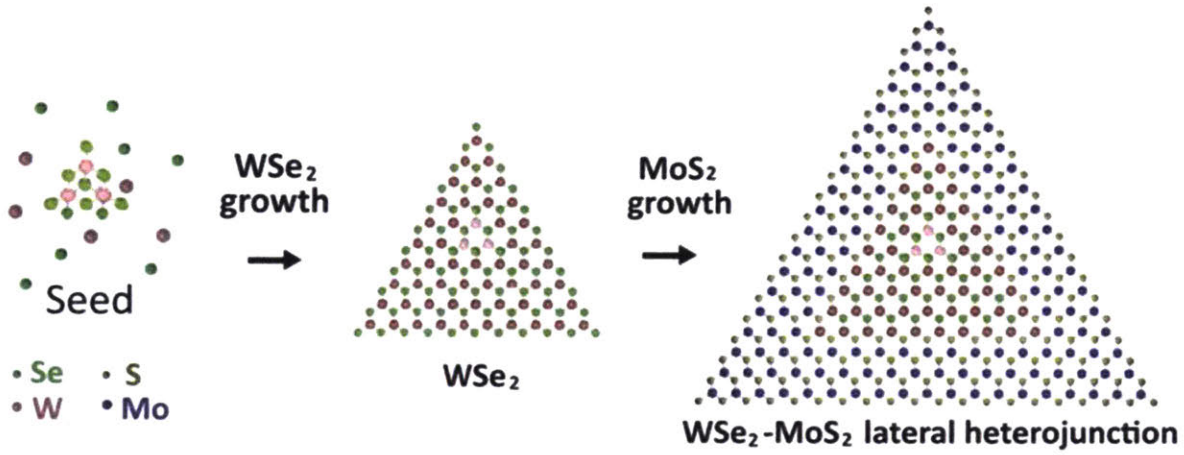

Figure 4-1: Schematic illustration of a sequential synthesis of a monolayer WSe_2-MoS_2 lateral heterostructure. Single crystalline WSe_2 monolayer growth WO_3 power as a precursor is performed first, which is followed by MoS_2 growth in a separate furnace using a MoO_3 precursor. Image from Ref[103]

Prior to transfer of the synthesized crystals, the ITO/glass substrates were cleaned by sonication in acetone, then isopropanol, and blown dry by ultrapure nitrogen. The WSe_2-MoS_2 heterojunction was spin-coated by a poly (methyl methacrylate) (PMMA) (950 PMMA A4, Micro Chem) and then the PMMA/sample/sapphire was dipped in a 6M HF solution to etch the interface between the sapphire and sample. PMMA/sample was lifted from the etching solution and diluted in DI water, and then transferred onto ITO/glass. Finally, the PMMA layer was removed after dipping in acetone and isopropanol.

4.2.2 Characterization of WSe_2-MoS_2 Lateral Heterostructures

The crystals were first identified by optical contrast and then their identity and thickness were verified using Raman and photoluminescence (PL) spectroscopy. An optical image and

the AFM topography of the transferred lateral heterostructure are shown in Figure 4-2 (a) and (b), respectively, where the in-plane junction in the triangular nanosheet is difficult to identify. For better visualization, a lateral force microscopy (LFM) image of the nanosheet was taken (Figure 4-2 (c)), which allows for the overall crystal shape and the lateral junction that distinguishes a region of WSe_2 from that of MoS_2 to be clearly seen.

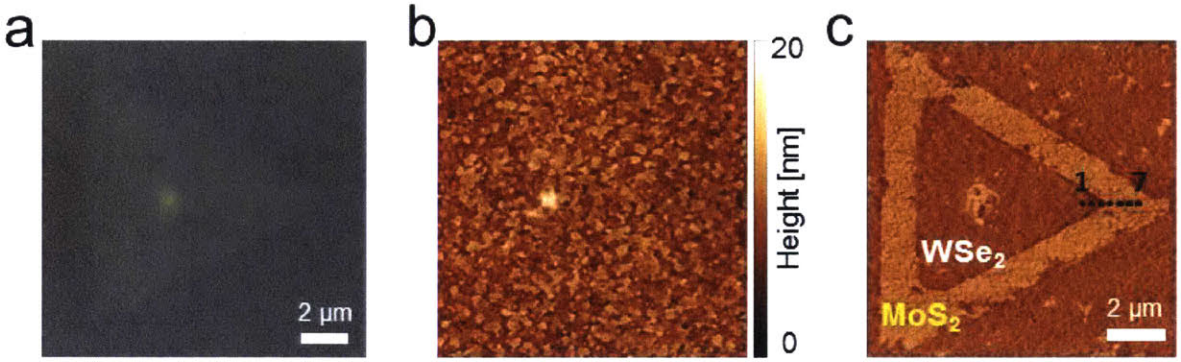

Figure 4-2: Characterization of a WSe_2-MoS_2 in-plane heterostructure. (a) Optical microscope image of a WSe_2-MoS_2 heterostructure crystal on ITO/glass substrate. (b) AFM topographic image of the sample featured in (a) that does not show a clear shape of the flake due to the roughness of the underlying ITO substrate. (c) Lateral force microscopy (LFM) image that shows the heterostructure crystal shape, including the distinct WSe_2 and MoS_2 regions. We note that the LFM contrast allows for the regions of different crystal composition to be clearly distinguished.

Raman spectroscopy and PL measurements were conducted to identify the number of layers based on the frequency of the signature Raman peaks and the difference (Δ) between them: the in-plane vibrational E_{2g} and the out-of-plane vibrational A_{1g} peaks, as reported by C. Lee *et al.*[60] Raman and PL measurements were performed on a Horiba Jobin Yvon LabRAM HR800 system with 532 nm laser excitation whose output power was reduced using neutral density filters to prevent damaging the crystal. The Raman peaks were fit to Lorentzian functions, while the PL was fit to Gaussian functions.

Prominent peaks of WSe_2 at 250 cm^{-1} and 260 cm^{-1} (Figure 4-3(a)), assigned to $E_{2g}{}^1$ and A_{1g} modes,[106] and the two signature Raman peaks of MoS_2 in Figure 4-3(b)—the $E_{2g}{}^1$ and A_{1g}

peaks with the frequency difference (Δ) of 19.6 cm^{-1}—confirm that the flake is comprised of a monolayer WSe_2 crystal surrounded by a monolayer MoS_2 crystal.[60]

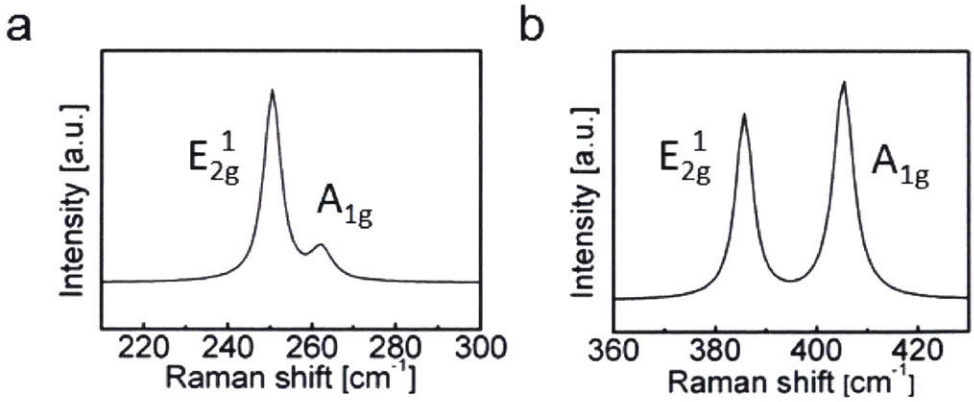

Figure 4-3: Characterization of a WSe_2-MoS_2 in-plane heterostructure. Representative Raman spectra taken at each homogeneous crystal region of (a) WSe_2 and (b) MoS_2.

The monolayer nature of the crystal is further confirmed by strong photoluminescence (PL) signals collected from the locations marked in Figure 4-2 (c), as shown in Figure 4-4.

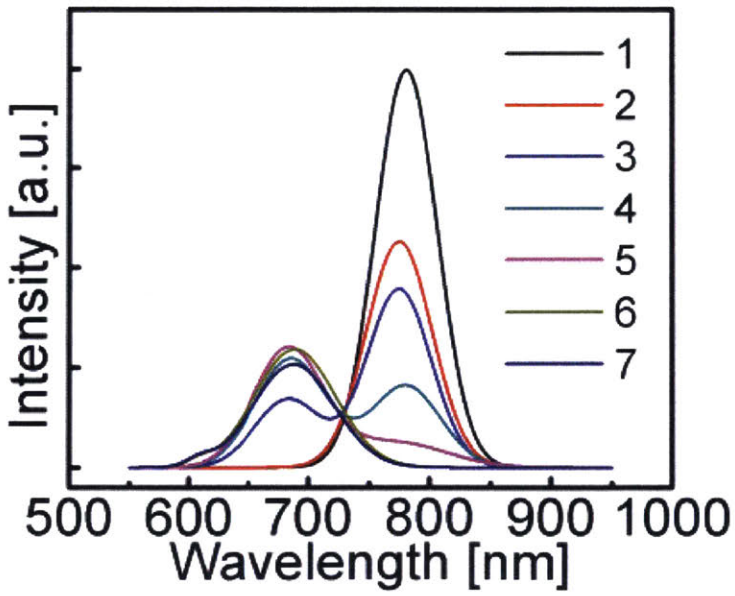

Figure 4-4: Representative photoluminescence spectra collected from the locations along the dashed line marked in Figure 4-2 (c).

4.2.3 C-AFM/ PCS-AFM Measurements

The C-AFM and PCS-AFM measurements were conducted on an Asylum MFP-3D system in ambient conditions, as illustrated in Figure 4-5. Conductive imaging used the ORCA conductive module from Asylum and PtIr-coated probes from Bruker. Current and topographic images were obtained simultaneously so that topography and local currents can be directly compared. Most AFM images were 512×512 pixels. For PCS-AFM, the instrument is mounted on an inverted optical microscope (Zeiss) with a 50X objective to focus light through the glass substrate at the tip-sample junction. The illumination source was a supercontinuum laser (SuperK Extreme from NKT Photonics), filtered by bandpass filters (FWHM = 10nm; Thorlabs, Inc.) to illuminate the sample at a selected wavelength. AFM images were analyzed and plotted using the Gwyddion software package,[61] which was also used to calculate the 2D fast Fourier transforms and root mean square (RMS) roughness values.

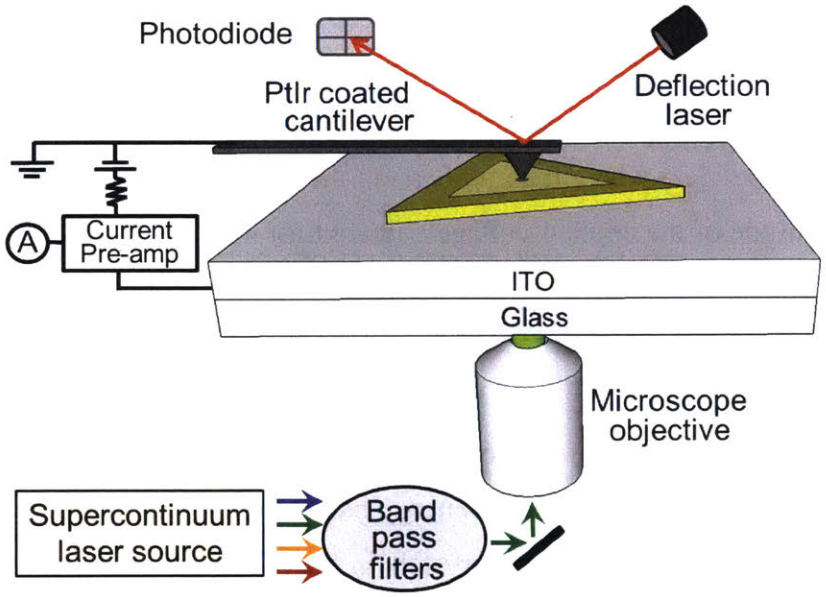

Figure 4-5: Schematic illustration of the photoconductive spectral atomic force microscope (PCS-AFM) instrument and WSe_2-MoS_2 heterostructure crystal.

4.3 Experimental Results

4.3.1 Carrier Transport in the Dark

Previously, we have shown that extracting averaged current–voltage (I–V) characteristics from a series of C-AFM images with varying applied voltages is superior over taking I–V curves at fixed positions, in that it generates not only more accurate and reliable I–V curves but additional information about spatial inhomogeneity in local charge distributions, local defects, sample edges, and local tip-sample interactions.[104] Thus, throughout this work we record the current through the C-AFM tip while imaging and varying the applied sample bias. Because the monolayer WSe_2-MoS_2 crystal is comprised of regions of homogeneous WSe_2, MoS_2, and the lateral junction in between that can fit within a single AFM image, we can directly compare electrical properties of regions obtained under identical experimental conditions.

In order to study the spatial dependence of local I–V characteristics of the heterostructure at its nanoscale junction with the conductive metal tip, a sequence of images were obtained at varying values of the applied bias voltage, as shown in Figures 4-6 (a)-(f) (forward bias) and 4-6 (g)-(o) (reverse bias) where the numbers on the top right side of each image indicate the sign and magnitude of the applied voltages. In contrast to the bare ITO surface showing high conductivity, the nanosheet introduces additional resistance against current flow, resulting in noticeable nonlinear behaviour as a function of applied voltage. In the forward bias regime, the current increases noticeably in the MoS_2 region while an almost no current increase is detected in the WSe_2 region; the opposite trend is observed in the reverse bias regime. This response suggests the formation of an energy barrier at the nanoscale junction between the metal tip and the semiconducting 2D crystals in both forward and reverse bias regimes. We note that there is some small degree of spatial inhomogeneity that may result from variations in local barrier heights arising from impurities, defects, and fluctuations in tip-sample contact. However, the possibilities of tip degradation affecting the current measurements can be excluded, as we have shown in our previous report by stable force-distance curves obtained throughout the series of measurements.[104]

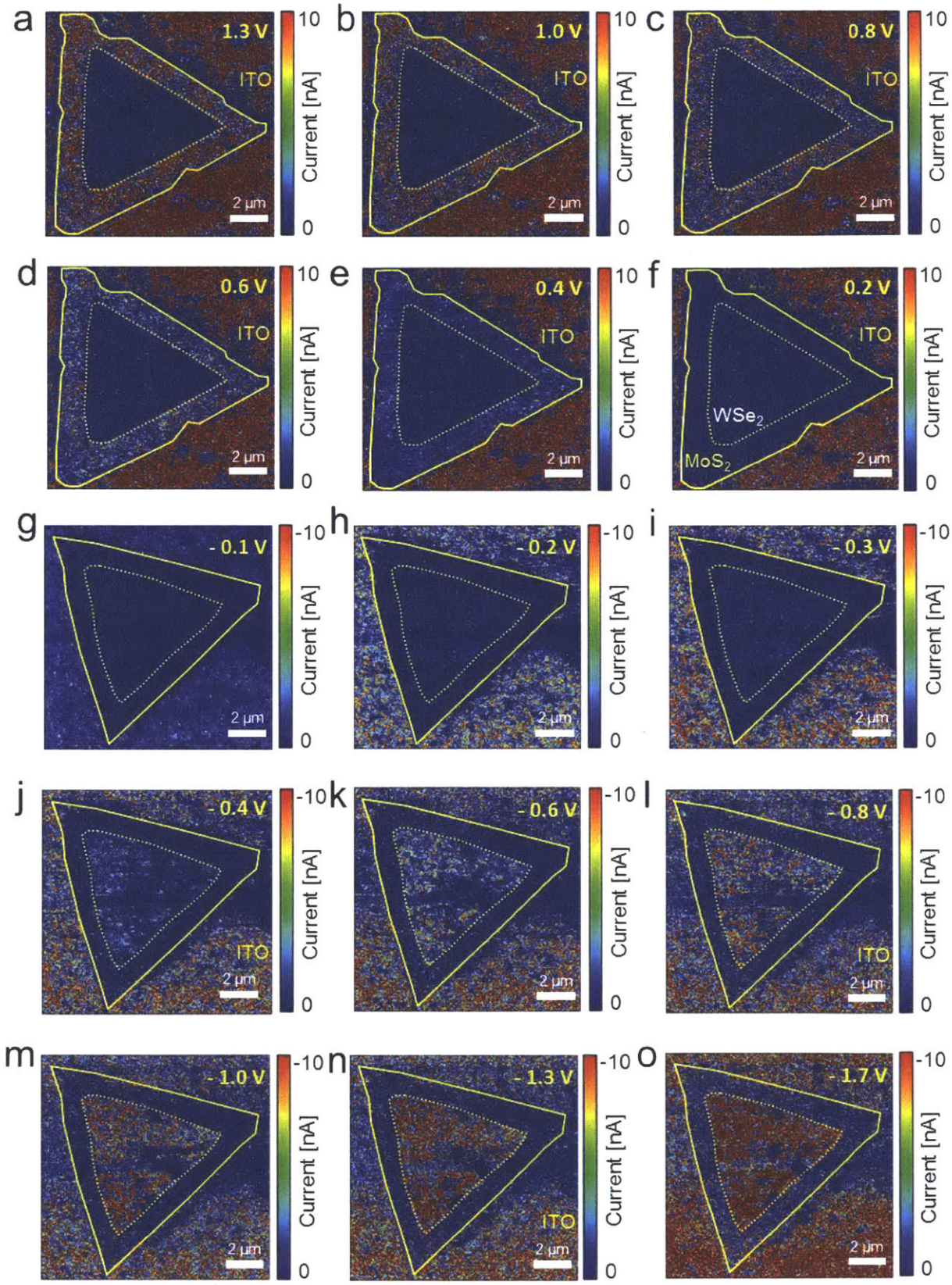
a
1.3 V
ITO
2 µm
10
Current [nA]
0
b
1.0 V
ITO
2 µm
10
Current [nA]
0
c
0.8 V
ITO
2 µm
10
Current [nA]
0
d
0.6 V
ITO
2 µm
10
Current [nA]
0
e
0.4 V
ITO
2 µm
10
Current [nA]
0
f
0.2 V
ITO
WSe2
MoS2
2 µm
10
Current [nA]
0
g
- 0.1 V
2 µm
-10
Current [nA]
0
h
- 0.2 V
2 µm
-10
Current [nA]
0
i
- 0.3 V
2 µm
-10
Current [nA]
0
j
- 0.4 V
ITO
2 µm
-10
Current [nA]
0
k
- 0.6 V
2 µm
-10
Current [nA]
0
l
- 0.8 V
ITO
2 µm
-10
Current [nA]
0
m
- 1.0 V
2 µm
-10
Current [nA]
0
n
- 1.3 V
ITO
2 µm
-10
Current [nA]
0
o
- 1.7 V
2 µm
-10
Current [nA]
0

Figure 4-6: Dark carrier transport as function of sample bias. Current maps generated by conductive AFM measurements in the dark under applied sample bias voltages of (a) 1.3 V, (b) 1.0 V, (c) 0.8 V, (d) 0.6 V, (e) 0.4 V, (f) 0.2 V, (g) -0.1 V, (h) -0.2 V, (i) -0.3 V, (j) -0.4 V, (k) -0.6 V, (l) -0.8 V, (m) -1.0 V, (n) -1.3 V, and (o) -1.7 V. Noticeable current enhancement with the applied voltage is observed in the reverse and forward bias regime for WSe_2 and MoS_2, respectively.

We then obtained *I–V* curves by averaging the current values from each voltage image at particular region of the sample: the homogeneous MoS_2 crystal, the homogeneous WSe_2 crystal, and a junction region near the boundary of the two compositions. Since earlier scanning Kelvin probe microscopy (SKPM) measurements on the heterostructure revealed that the depletion width across the lateral junction is ~320 nm,[103] current values for the junction were extracted from pixels that are within ~120 nm of the boundary towards homogeneous crystals of MoS_2 and WSe_2. The junction boundary is determined from the lateral force image (Figure 4-2 (c)) in which the border line can be identified clearly due to the difference in force fields the metal tip experiences when scanning over the crystal regions of WSe_2 and MoS_2. Figure 4-7 shows the averaged *I–V* curves from the homogeneous WSe_2 and MoS_2 crystals, as well as both WSe_2 and MoS_2 sides of the junction in between them, where the error bars indicate the standard deviations from all the pixels within the current images at each given voltage. The green triangles, black squares, blue triangles and red indicate data points acquired from each of the WSe_2, MoS_2, and lateral junction regions of WSe_2 and MoS_2, respectively, under identical experimental conditions. Because we average over many thousands of data points for each voltage, a reliable *I–V* curve can be obtained.

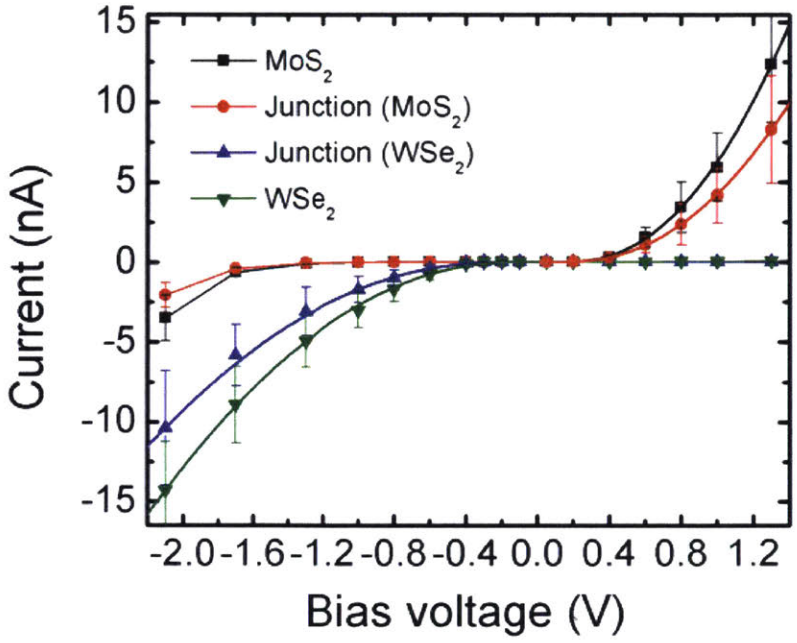

Figure 4-7: Averaged *I-V* data extracted from the homogeneous and lateral junction regions of WSe_2 and MoS_2, where a slightly lower conductivity is recorded in the junction areas than their respective homogeneous regions.

The *I–V* curves in Figure 4-7 show nearly insulating behavior at low bias voltages and abrupt nonlinear increases in current at high bias voltage in both the reverse and forward bias regimes. This is in good agreement with our prior finding that the nanojunction between atomically thin 2D layers and the metal tip gives rise to the characteristic rectifying carrier transport behavior due to the formation of the junction energy barrier, which is impacted by both barrier height and width.[104] This is well explained by Fowler-Nordheim (FN) tunneling model that is widely adopted as a model for describing charge carriers tunneling from the Fermi level of a metal to an adjacent material through a junction barrier.[79] Even though charge carriers experience the resistance of an atomically thin layer of almost the same thickness (~0.7 nm), *I–V* curves obtained from WSe_2 and MoS_2 show an entirely different trend: the conductivity of WSe_2 increases exponentially as reverse bias voltage increases without noticeable current recorded in the forward range, whereas the opposite is the case for MoS_2. This corroborates the interpretation of the carrier transport mechanism proposed in our previous paper by expanding to new systems.

Schematic illustrations in Figure 4-8 show the band structures of the PtIr/WSe_2 and PtIr/MoS_2 systems under applied biases: forward bias ($V > 0$) is shown on the left and reverse bias ($V < 0$) on the right. When the metal tip is brought into contact with a thin WSe_2 or MoS_2 crystal, the difference between the metal work function and the valence (conduction) band edge of WSe_2 (MoS_2), based on the Schottky-Mott theory,[78] causes a Schottky barrier to form at the interface. Because of the p-type nature of WSe_2, when it is in contact with the PtIr tip whose work function is ~5.4 eV, [75] the equilibrium Fermi level locates close to the valence band edge.[107] In the case of n-type MoS_2, partial Fermi level pinning positions the equilibrium energy near the conduction band edge.[80] We ignored the role of the sample/ITO junction in the analysis of the carrier transport in consideration of relative energy barrier height at the tip/sample and sample/ITO interfaces. The ITO substrate used in this work is a heavily n-doped with a work function of $\Phi_{ITO} \sim 4.7$ eV, and the metal tip is coated with PtIr with $\Phi_{PtIr} = 5.4$ eV.[75] Taking the work function of a single layer MoS_2 ($\Phi_{MoS_2,\,1L} \sim 4.7$ eV[4, 40, 59]) into account, barrier height of the MoS_2/ITO junction ($\Phi_{B,MoS_2/ITO} = \Phi_{MoS_2,\,1L} - \Phi_{ITO}$) is substantially smaller than that of the tip/MoS_2 junction ($\Phi_{B,tip/MoS_2} = \Phi_{PtIr} - \Phi_{MoS_2,\,1L}$), which allows for the tip/MoS_2 junction to dominate the transport process. Similarly, given $\Phi_{WSe_2,\,1L} \sim 4.45$ eV,[108] $\Phi_{B,WSe_2/ITO}$ ($\Phi_{WSe_2,\,1L} - \Phi_{ITO}$) is quite smaller when compared to $\Phi_{B,tip/WSe_2}$ ($\Phi_{PtIr} - \Phi_{WSe_2,\,1L}$), causing the transport process to be mainly determined by the tip/WSe_2 junction. Both the electron and the hole currents beyond a certain threshold voltage include two contributions: the tunneling events through the Schottky barrier and thermionic emission current over the top of the energy barrier.

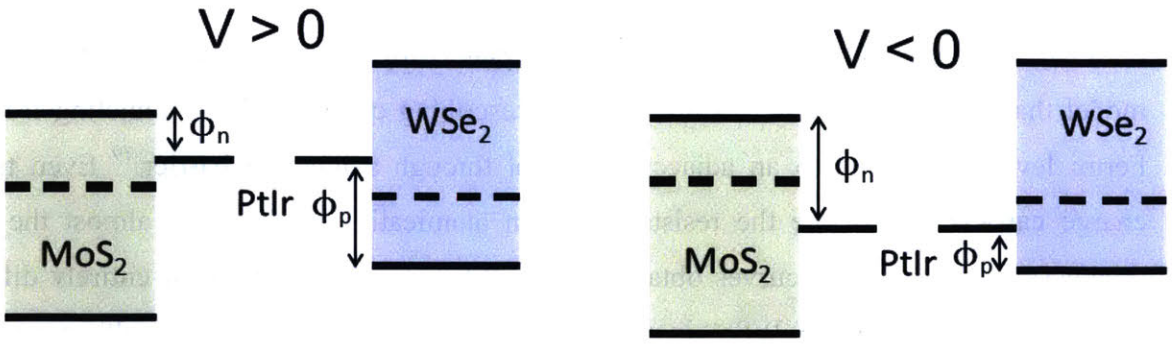

Figure 4-8: A schematic band diagram of a WSe_2/MoS_2–PtIr metal tip junction under forward (left) and reverse (right) sample bias voltages. The formation of a Schottky barrier impacts the carrier transport.

At the junction between WSe_2 and the PtIr metal tip, the Schottky barrier height for hole injection into the valence band of WSe_2 (ϕ_p) is lower than that for electron injection into the conduction band (ϕ_n). In the reverse bias regime, the barrier height and width is reduced with higher applied voltage, resulting in an enhanced probability of field emission tunneling through the barrier. When the forward bias voltage is applied, the likelihood of hole tunneling events is suppressed to its lowest saturation and the thermionic emission contribution becomes increasingly smaller with voltage due to the raised Schottky barrier height, ϕ_p. In contrast, when the interface between MoS_2 and the metal tip is considered (here, ϕ_n is smaller than ϕ_p), the barrier width becomes smaller as higher voltage is imposed, enhancing the tunneling contribution dramatically in the forward bias regime, while more negative voltage constrains the tunneling to its lowest and thermionic emission to further reduced level due to thickened junction barrier and an eventual increase of ϕ_n.

This stark difference of electrical properties between the two single-layered component crystals of the lateral heterostructure highlights a critical role of the nature of the junction barrier on carrier transport behavior through the nanoscale metal-atomically thin 2D crystal interface. In addition, it is notable that the junction regions of both WSe_2 and MoS_2 exhibit lower conductivity than corresponding homogeneous regions throughout the whole voltage range of our measurements. We attribute the origin of this observation to the change in the energy of the conduction and valence band edges over the depletion width of the lateral p-n junction. On the WSe_2 side of the depletion region, the energy of the valence band edge gradually decreases, rendering ϕ_p larger compared to its homogeneous counterpart when in contact with the metal tip. The fact that the subtle change in the electronic properties of the lateral junction region of the sample is detected highlights the sensitivity of the measurements offered by the PCS-AFM instrument, which could be especially beneficial to answer many interesting questions about nanomaterials with complex heterojunctions. Similarly, for the MoS_2 side of the region, because the conduction band energy rises as it comes closer to homogeneous WSe_2, ϕ_n becomes higher hindering electron injection to this region to some extent. This finding of differing junction behavior further corroborates the sensitivity of carrier transport at the nanoscale metal-2D layer interface on the junction barrier characteristics.

In order to extract the barrier heights for electron injection to the conduction band of MoS_2 ($\phi_{n,MoS2}$) and hole injection to the valence band of WSe_2 ($\phi_{p,WSe2}$), following our previous publication,[104] we use the FN tunneling theory, which is widely adopted as a model for describing electrons tunneling from the Fermi level of a metal to an adjacent material through a junction barrier, with the current I described by:[79]

$$I(V) = \frac{A_e q^3 m V^2}{8\pi h \phi_B d^2 m^*} exp\left[\frac{-8\pi\sqrt{2m^*}\phi_B^{3/2} d}{3hqV}\right] \quad (18)$$

where A_e denotes the effective contact area, q the electronic charge, V the applied bias voltage, h Planck's constant, ϕ_B the barrier height, d the distance between the electrodes, and m^* the effective mass. The experimental I–V data in Figure 4-7 are fit to the FN tunneling model in equation (1) (solid black, red, green, and blue lines for MoS_2, MoS_2 junction, WSe_2, and WSe_2 junction, correspondingly). We see that the FN model agrees well with the data and the effective barrier height can be extracted from the fitting to the model to be 0.58, 0.60, 0.62, and 0.65 eV, for $\phi_{n,MoS2}$, $\phi_{n,MoS2}$,junc, $\phi_{p,WSe2}$, and $\phi_{p,WSe2}$,junc, respectively. The extracted $\phi_{n,MoS2}$ in the present work is close to but slightly lower than the value estimated for a micromechanically exfoliated monolayer MoS_2 using the same experimental setup, 0.61 eV.[104] This can be attributed to the fact that the work function of the synthesized and mechanically exfoliated MoS_2 crystals may somewhat differ from each other, and dissimilar ITO substrates could lead to different interactions with the sitting 2D crystals that consequently give rise to changes in the junction properties.

4.3.2 Voltage Selectable Photoresponse

Since this monolayer in-plane p-n heterostructure possesses an enormous potential to play a major role as an active component over a wide variety of future nanoscale optoelectronic devices, we also explore its photoresponse using the PCS-AFM measurements to answer important questions about spatial variation of its local optoelectronic properties. We use the same heterostructure nanosheet that was featured in Figure 4-2 for these optoelectronic measurements in order to directly compare the results to the dark current behavior. The

analysis conducted for dark current can be expanded to interpret strong dependence of photocurrent on the applied voltage. Figures 4-9 show spatially resolved photoresponse maps of the sample, in both forward and reverse voltage regimes. The bias voltages are varied while the illumination is maintained at λ = 550 nm. Current images in dark and light used to generate photoresponse maps are found in Figure 4-10. The photoresponse is defined as the difference between photocurrent (I_L) and dark current (I_D) normalized by illumination power:

$$\text{photoresponse} = \frac{(I_L - I_D)/q}{P_{inc}/h\nu} \tag{19}$$

where q is electronic charge, P_{inc} the incident power, and $h\nu$ the photon energy. These photoresponse maps are generated by subtracting a photocurrent map under illumination from a dark current map, and normalized by the incident laser power at a selected wavelength. It is important to note that the wavelength dependence of photoresponse of MoS_2 detected using this instrument in our prior report[104] shows that the enhanced current under illumination is predominantly due to interband photoexcitation in a 2D material being interrogated rather than absorption or heating effects in the metal tip.

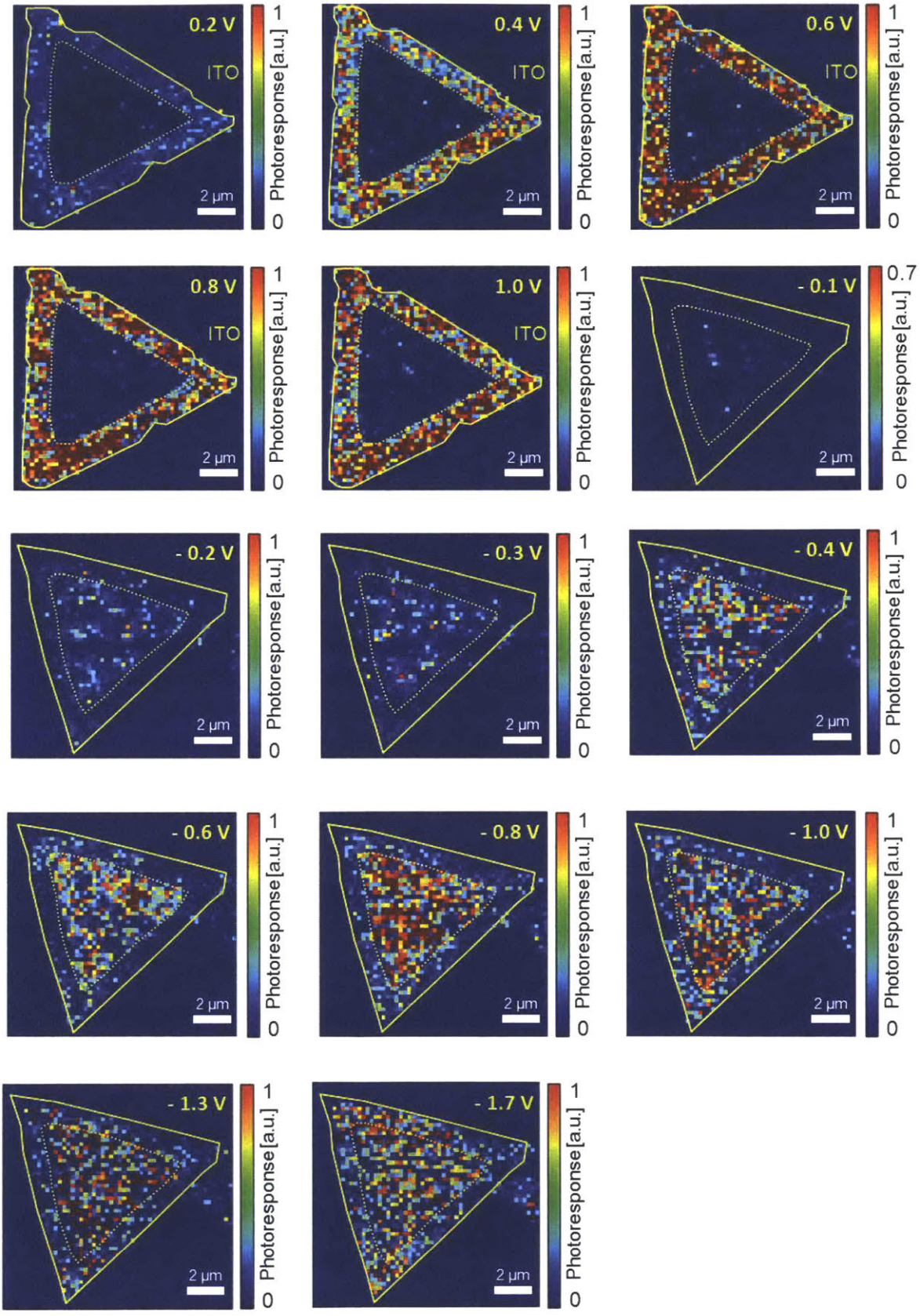
0.2 V
ITO
2 μm
Photoresponse [a.u.]
1
0
0.4 V
ITO
2 μm
Photoresponse [a.u.]
1
0
0.6 V
ITO
2 μm
Photoresponse [a.u.]
1
0
0.8 V
ITO
2 μm
Photoresponse [a.u.]
1
0
1.0 V
ITO
2 μm
Photoresponse [a.u.]
1
0
- 0.1 V
2 μm
Photoresponse [a.u.]
0.7
0
- 0.2 V
2 μm
Photoresponse [a.u.]
1
0
- 0.3 V
2 μm
Photoresponse [a.u.]
1
0
- 0.4 V
2 μm
Photoresponse [a.u.]
1
0
- 0.6 V
2 μm
Photoresponse [a.u.]
1
0
- 0.8 V
2 μm
Photoresponse [a.u.]
1
0
- 1.0 V
2 μm
Photoresponse [a.u.]
1
0
- 1.3 V
2 μm
Photoresponse [a.u.]
1
0
- 1.7 V
2 μm
Photoresponse [a.u.]
1
0

Figure 4-9: Photoresponse as function of sample bias. Photoresponse maps at forward bias voltages of 0.2 V, 0.4 V, 0.6 V, 0.8 V, and 1.0 V, and reverse bias voltages of -0.1 V, -0.2 V, -0.3 V, -0.4 V, -0.6 V, -0.8 V, -1.0 V, -1.3 V, and -1.7 V under illumination of λ = 550 nm.

The following are additional current maps under laser illumination of λ = 550 nm that were used to generate photoresponse maps.

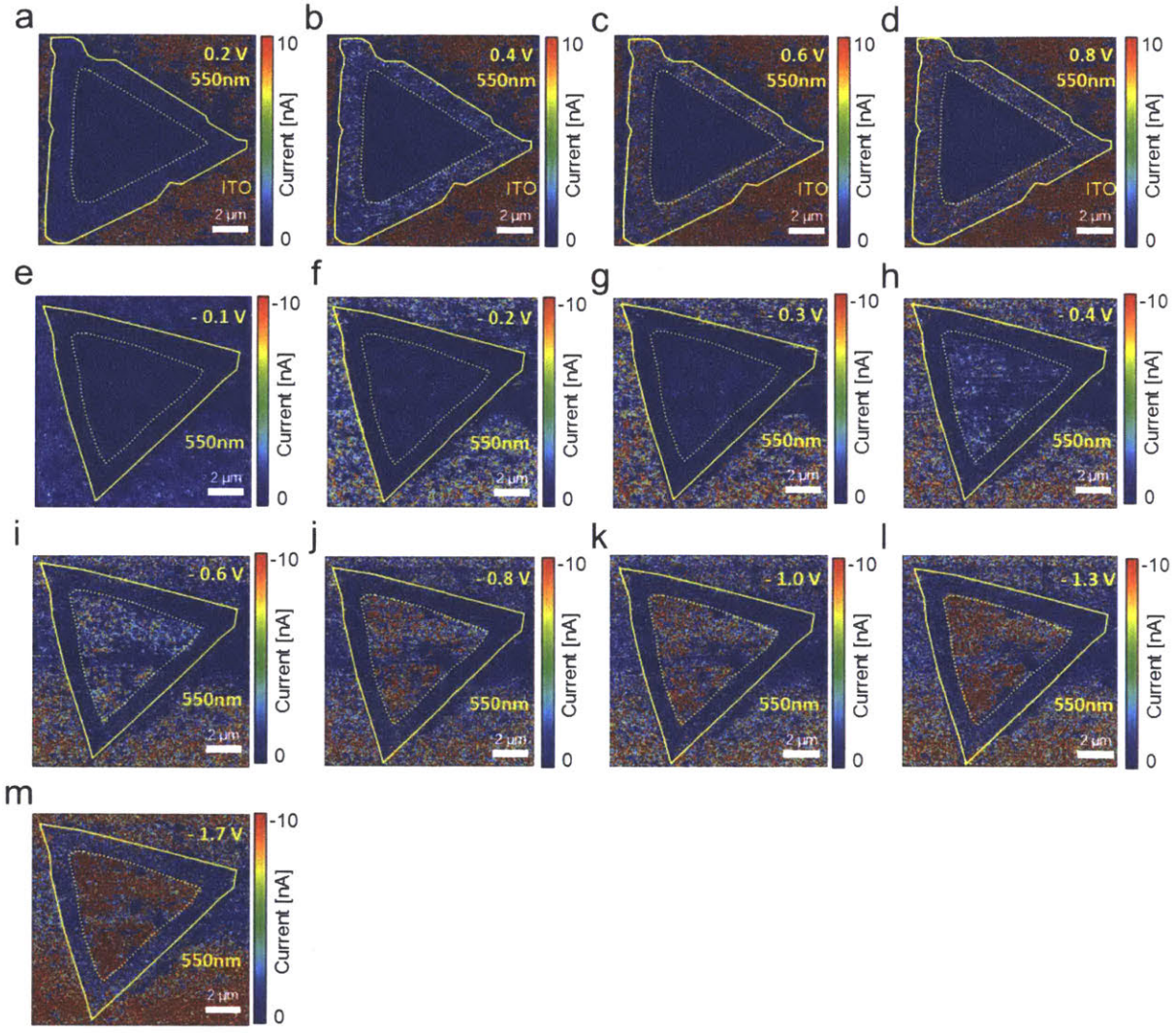

Figure 4-10: C-AFM images under illumination. Current maps generated by PCS-AFM measurements under laser illumination of λ = 550 nm with an applied (a-d) forward and (e-m) reverse bias voltage applied that were used to generate the photoresponse maps.

Recently, Rezk *et al.*[109] have demonstrated the modulation of the photoluminescence of single and odd-numbered multilayered MoS_2 using high frequency sound wave coupling. The piezoelectric effect might have had a slight influence on the photoresponse because we have investigated a single layer heterostructure sample. However, in our prior work,[104] the spectral photoresponse of an MoS_2 crystal that consists of 1L, 2L, 3L and 4L regions showed clear onsets of photoresponse at different wavelengths that coincide with the band gap energy for each thickness—clearly suggesting that the enhanced current upon laser illumination is predominantly due to interband photoexcitation in MoS_2. Additionally, a monotonically decreasing trend of photoresponse from 1L to 4L further corroborates the dominant role of the thickness-dependent band structures and tunneling barriers in the photoexcitation and photocarrier collection processes. If the piezoelectricity played a major role in our experiments, response from the odd-numbered MoS_2 regions (1L and 3L) would have exhibited a distinct trend from that of the even-numbered regions (2L and 4L), which was not observed. Therefore, we believe that the piezoelectricity contribution in our measurements is negligible and can safely be ignored in the analysis. Also, in a recently published study,[110] Miller *et al.* have reported the photodoping effect observed in single- and few-layer MoS_2 where the authors demonstrated that the effect originated from removing physisorbed molecules such as H_2O and O_2 on the surface of MoS_2 which prevented the charge transfer from MoS_2 to the adsorbed molecules, thereby increasing charge carrier density in MoS_2. Thus, the increased charge carrier density (Δn) was observed to be nearly identical regardless of the number of layers at the same laser power. In our previous publication,[104] the photoresponse of MoS_2 first showed a marked decrease with the layer number from 1L to 4L but rebounded thereafter. If the photodoping was the determining factor in our experimental process, the photoresponse should have been monotonically decreased with the layer number due to the more unfavorable carrier transport through the junction, which is clearly not the case. In addition, our unique experimental conditions—where the tip contacts the top surface of the sample and the laser is illuminated from the bottom of the sample—render the photodoping process less viable. For these reasons, we ruled out the photodoping effect in analyzing the observed photoresponse data.

In the photoresponse maps (Figure 4-9), while a small level of spatial irregularities is observed due to local variability of electrical properties of the junction with the metal tip. Pixels within the boundaries of an each homogeneous crystal region in general show reasonably constant photoresponse intensities over the entire sample area, demonstrating stability and reliability of our measurements. Under small magnitude applied sample voltages both WSe_2 and MoS_2 generate a very small degree photoresponse. But interestingly, when we apply a larger magnitude voltage in the forward bias regime, the pixels in the MoS_2 region clearly turn on while those in the WSe_2 region remain dark. Moreover, by applying the opposite polarity and large magnitude bias voltage, the MoS_2 pixels can be switched off while turning the WSe_2 pixels on. The degree of this photoresponse switching—a relative photoresponse of one region to another—can effectively be modulated by the magnitude of the applied sample. That is, by utilizing this experimental approach, a nanoscale high-resolution array of switchable photodiode pixels can be realized.

The photoresponse as a function of voltage was plotted by taking the average photoresponse over each of the homogeneous and junction regions, as shown in Figure 4-11, where error bars indicate the standard deviation. We note that the photoresponse in forward and reverse bias regimes exhibits obvious barrier asymmetry for both WSe_2 and MoS_2 and shows a nonlinear increasing trend in all regions as the bias voltage is raised. In the previous chapter we showed that major factors influencing the photoresponse detected by the PCS-AFM system are light absorption, photoexcited carrier separation, and carrier collection efficiencies.[104] Since we explore the heterostructure crystal of uniform thickness (monolayer), the pixels in the same region should have the almost same absorption efficiency—given the absorption coefficients are similar at 550 nm illumination[111]—thereby making the light absorption factor negligible in the interpretation of the bias-dependent photoresponse trend of each region, as compared to the other two contributions. The importance the carrier collection efficiency contribution (effective transport of photoexcited carriers through the nanoscale metal-2D layer junction to be collected by the metal tip) to the overall photoresponse becomes evident when comparing photoresponse values of WSe_2 and MoS_2 acquired with high bias voltages applied in the reverse and forward range, respectively. Under these high drive bias voltages, there is enough external driving force to effectively separate photoexcited charge carriers such that the effectiveness of exciton dissociation

becomes insignificant, allowing for the carrier collection events to dominate the process. We observe that the photoresponse of WSe_2 under this condition in the reverse range is lower than that of MoS_2 in the forward regime, which is in accordance with the dark current trend shown in Figure 4-7 in which absolute current values are smaller in WSe_2 than MoS_2 for equal absolute sample bias voltages. The fact that WSe_2 (MoS_2) generates a very low level of the response throughout the forward (reverse) regime can also be ascribed to the reduced carrier collection efficiency because of the increased effective junction barrier. Although it may be possible that small contributions to this difference may originate from different absorption coefficients of the two for a chosen laser wavelength,[112] the overall trend is mostly determined by the transport characteristic.

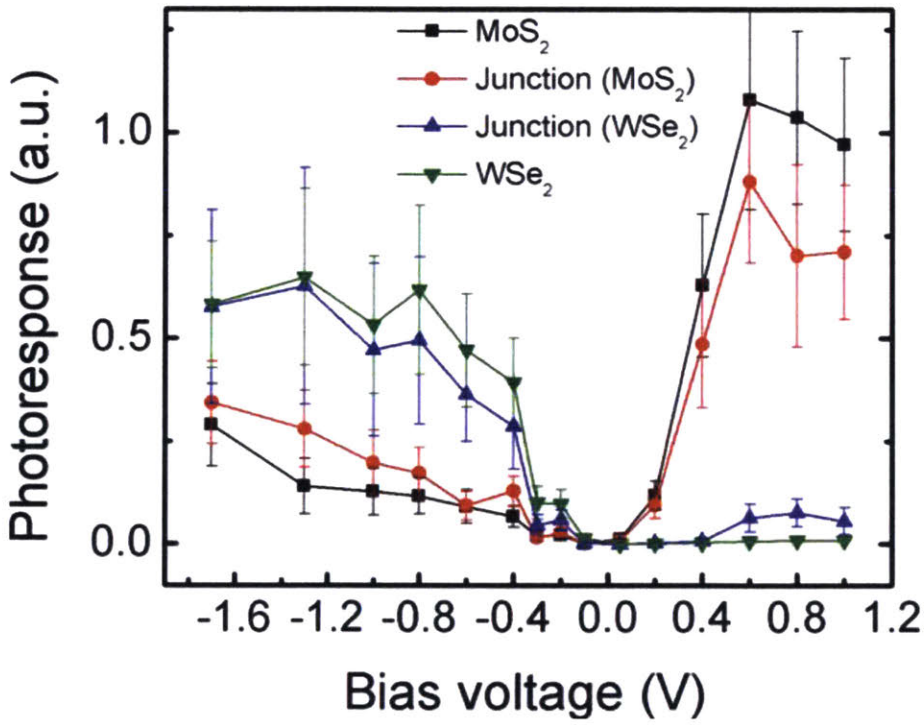

Figure 4-11: Photoresponse as function of sample bias. Plot of photoresponse versus voltage with the error bars indicating standard deviations. We observe significant barrier asymmetry for all regions. Photoresponse of WSe_2 (MoS_2) in the junction part is lower (higher) compared with the homogeneous region in the reverse bias regime, whereas the opposite is the case in the forward voltage regime.

The photoresponse in both WSe_2 and MoS_2 rises sharply in a nearly linear fashion—in the reverse and forward regime, respectively—as the absolute sample voltage is raised until around 0.8 V, owing to the increasingly improved carrier transport and a larger amount of energy available for carrier separation, and becomes relatively flat without showing notable increase afterwards. It can be because the 0.8 V of drive voltage provides enough energy to separate and collect most of the photoexcited charge carriers. In forward (reverse) bias for WSe_2 (MoS_2), however, photoexcited carriers face a barrier at the junction with the metal tip that needs to be thermally overcome or tunneled through to be detected, and the barrier that remains in the voltage range of our experiment can lead to the observed forward-reverse asymmetry. In the junction region of both WSe_2 and MoS_2, the response shows a dissimilar behavior under forward and reverse bias voltages: lower (higher) in the reverse regime but higher (lower) under the forward bias for WSe_2 (MoS_2) in comparison with its homogeneous counterpart. This result suggests that the overall photocurrent is almost entirely determined by the carrier transport process—which is mainly influenced by change in the band edge energy in the depletion region—in one bias voltage regime, while the built-in electric field enhancement at the lateral p-n junction can give rise to an additional contribution to photocurrent when the bias polarity is flipped. This understanding of photocurrent generation from a WSe_2-MoS_2 lateral heterostructure will provide useful insight into developing a high-resolution array of nanoscale photodetector units with an optimized photoresponse ratio between component pixels by the selection of the specific polarity and magnitude of voltage to achieve for targeted purposes, which can be further tuned by modulating illumination laser wavelengths as well as the layer number of component materials.

4.3.3 Consideration of Photocarrier Dynamics

In the previous chapter we explained the sublinear illumination power dependence of photocurrent by a kinetic model that accounts for the rapid exciton-exciton annihilation (EEA)[86] in atomically thin MoS_2 crystals. In the model, the exciton density is expressed with loss terms by the EEA and exciton dissociation, and a generation term which is dependent on

the laser power and the layer thickness. Since residence time of the metal tip on each pixel while scanning is on the order of ~ 10^{-3} s, which is substantially longer than an effective lifetime for excitons in a single layer MoS_2, the system is considered to have reached the steady-state and the EEA rate constant (k_1) and the free carrier generation rate (dissociation of exciton, k_2) for a monolayer MoS_2 are extracted as $k_1(MoS_2) = 4.3 \times 10^{-2} cm^2 s^{-1}$ and $k_2(MoS_2) = 3.3 \times 10^{-1} s^{-1}$. By adopting these constants and assuming that the ratio of k_1 to k_2 for WSe_2 is the same as for MoS_2 in consideration of the similar exciton binding energy,[113] the ratio of the averaged photocurrent in MoS_2 to that in WSe_2 recorded under a 0.6 V magnitude of voltage at 550 nm—the same experimental condition as the prior report—yields $k_1(WSe_2) = 9.5 \times 10^{-3} cm^2 s^{-1}$ and $k_2(WSe_2) = 7.3 \times 10^{-2} s^{-1}$. Here, the extinction coefficient at 550 nm is set to be $\varepsilon_{MoS_2}/\varepsilon_{WSe_2} \sim 1.2$.[111]

4.3.4 Spatial Analysis: 2D FFT

We conducted spatial analysis of the AFM topography and current images in order to clarify the role of the ITO substrate on current measurements. Figure 4-12 shows topographic (a, c, and e) and current (b, d, and f) images simultaneously obtained with an applied sample bias of 0.7 V. The effect of the underlying substrate was investigated in detail by further comparing regions of the substrate with and without a MoS_2 crystal sitting on top, as indicated in the panels 4a and b. The 2D fast Fourier transforms (FFTs) were performed on the bare substrate and substrate+MoS_2 regions of the topographic (4-12 (g) and (i)) and current images (4-12 (h) and (j)). It is observed that the intensity of both of the FFTs of the topography is mostly concentrated in the center region; but that of the substrate-only region in the current image exhibits a concentric but dispersed feature, and a more dispersed along with increased intensity along the vertical direction is observed in the substrate+MoS_2 region. These results reveal that there exists some degree of spatial correlation between the topography and current of the bare substrate, but the correlation weakens with the introduction of an atomically thin nanosheet. We attribute these findings to imperfect contact between the nanosheets, the substrate, and the metal tip, which can be aggravated because of the fast tip movement. More fluctuations observed in the substrate+MoS_2 region of the current image can originate from the nature of the measurements: the charge carriers have to

physically flow from the substrate through the nanosheets to the metal tip, which makes the current more sensitive to irregularities or small changes in the contact qualities between the components in contact mode imaging.

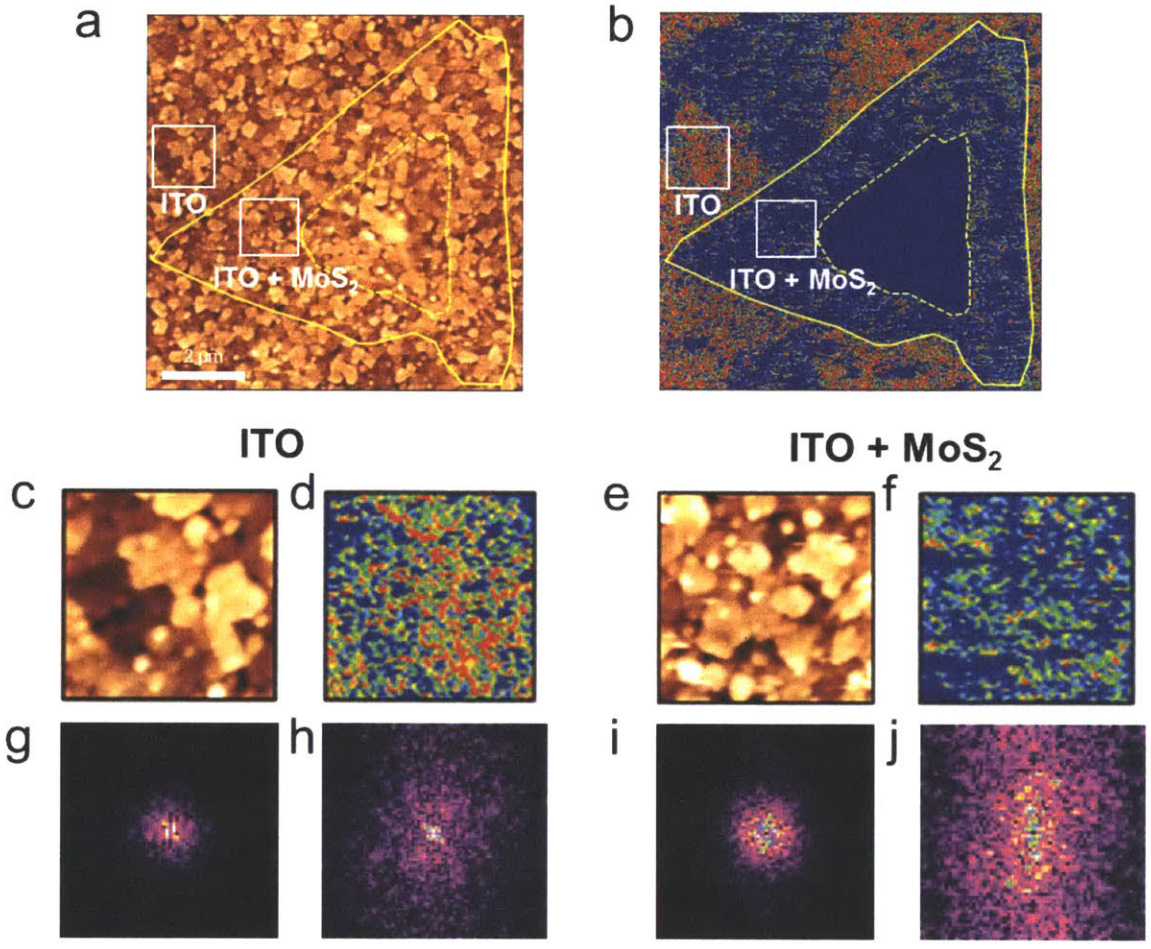

Figure 4-12: Spatial analysis of topography and current images. (a) Topographic height AFM image of a WSe_2-MoS_2 nanosheet. (b) A simultaneously obtained current image at sample bias of 0.7 V. The regions in squares marked ITO and ITO+MoS_2 are regions of bare ITO and ITO covered by the MoS_2 region of the flake, respectively. The ITO-only region is enlarged in (c)-(d) and the ITO+MoS_2 region in (e)-(f). The current image (d) shows spatial correlation with the grains or terraces in (c), but the current image (f) shows less clear correlation with (e), and has more inhomogeneity in current. (g)-(j) 2D fast Fourier transforms (FFTs) of the images in (c)-(f). The FFT patterns of the topographic images (g) and (i) are quite similar, and show a relatively isotropic distribution of features at low spatial frequencies. The FFT patterns of the current images (h) and (j) show differences: the FFT of ITO+MoS_2 has a lot more intensity in the vertical direction, suggesting increased inhomogeneity in the horizontal direction of the current image, corresponding to the fast scan direction. We attribute the

current inhomogeneity to small amounts of crinkling in the nanosheet under the tip as it scans across the surface, resulting in more variable electrical contact.

4.4 Conclusion

In conclusion, we utilized the C- and PCS-AFM measurements to thoroughly investigate current transport mechanisms and photoresponse of a monolayer lateral WSe_2-MoS_2 heterostructure at its nanoscale junctions with the conductive metal tip. We found that the carrier transport is determined by the characteristics of the junction barrier, which can be explained by the FN-tunneling model assisted by thermionic emission. WSe_2 and MoS_2 show the opposite trend due to the different junction barrier properties while relatively lower conductivity is recorded in the lateral junction region because of the energy change in the valence and conduction band edges. A prominent voltage-dependent photoresponse was observed in both WSe_2 and MoS_2 in the reverse and forward sample bias regime, respectively. Notably, by modulating the polarity and magnitude of the applied voltage, the photoresponse pixels in a portion of the heterostructure crystal was observed to be selectively switched on and off, allowing for a high-resolution array of the switchable photodiode pixels to be demonstrated. This experimental technique shed light on the realization of future optoelectronic nanoscale devices for regioselective photodetection and imaging. By performing the comparative 2D Fourier analysis of topography and current images, it is revealed that high spatial frequency inhomogeneities in substrate/MoS_2 (or WSe_2) contact exceed the frequencies imposed by the underlying substrates. The fundamental insight into the local electronic and optoelectronic behavior of a WSe_2-MoS_2 lateral heterostructure at the nanoscale resolution that we have achieved in this work is not limited to this specific material and will greatly aid in the design and further advancement of future nanoelectronic devices based on various types of monolayer lateral heterostructures in general.

5. Understanding and Engineering of Interfaces between 2D Materials

*Partly adapted with permission from Shih, CJ., Wang, QH., **Son, Y.** et al. ACS Nano 2014, 8 (6), 5790-5798. Copyright 2014 American Chemical Society*

5.1 Introduction

Since a monolayer graphene was successfully isolated by the micromechanical exfoliation technique,[1] various of other 2D materials—including hBN and TMDCs that possess distinct properties from graphene—have been tested extensively for a broad range of nanoelectronic and optoelectronic applications. Although recent developments of nanoelectronics using these two-dimensional (2D) materials[114, 115] have demonstrated potential towards further miniaturization beyond Moore's law,[46] as well as a high-mobility solution in the emerging fields of large-area, flexible, and low-cost electronics,[115, 116] homogeneous devices consisting of only one of the 2D materials have shown their limitations due to intrinsic material properties: Graphene itself is a semimetal with zero band gap with an ultrahigh carrier mobility,[12, 117, 118] providing superior current drive under low voltage bias while barely allowing for a low level of off-current values; On the other hand, MoS_2 (2D semiconductor material) possesses an indirect band gap (of 1.2 eV as a multilayer and a direct band gap of 1.8 eV as a monolayer)[44, 77] that has enabled digital electronic components[46-49, 119-124] and circuits[115] on top, but MoS_2 solely may not be suitable for high-performance digital applications due to its relatively heavier electronic mass and low carrier mobility (~ 1 - 50 cm^2/Vs).[125, 126] Thus, it is ideal to develop a material or structure that combines desirable properties of each 2D material, for example, the high mobility of graphene and the band gap of MoS_2. As one of the possible solutions in this quest, it was suggested that dissimilar 2D materials could be stacked together vertically, in which graphene was stacked on top of hBN crystals.[127] Since then, integrating dissimilar 2D materials into a vertical 2D heterostructure that exhibits entirely new properties beyond that of the component 2D crystals has emerged as an active area of research, exploring various combinations in any sequences. Thus, in this chapter, we explore two different vertical heterostacks—graphene/MoS_2 and black

phosphorus/MoS2. We first study in detail underlying physics at their interface using conductive AFM, Raman spectroscopy, and photoluminescence measurements, which reveal evidence of charge transfer and junction barrier formation. Then we take advantage of the junction properties to develop new types of vertical heterojunction devices that show advanced characteristics over devices made out of each component material.

5.2 Experimental Results

5.2.1 Charge Transfer and Photoluminescence at MoS_2-graphene Junctions

In order to study electron transfer and PL in MoS_2-graphene heterostructures without applying transverse electric fields, we fabricated the stacked atomic layers by the micromechanical exfoliation of MoS_2 crystals onto a SiO_2 substrate, followed by transferring a piece of monolayer, CVD-synthesized graphene onto the surface. An optical microscope image and topographical sketch of a representative graphene-coated MoS_2 crystal are shown in Figures 5-1 (a) and (b), respectively. The regions associated with monolayer (1), trilayer (3), and bulk MoS_2 are identified using Raman spectroscopy and labeled in Figure 5-1 (b). It is noteworthy that there is a tear formed unintentionally in graphene during the transfer process, allowing us to compare the behavior of MoS_2 with and without interacting with graphene. First, c-AFM is used to characterize the MoS_2-graphene heterostructure using a diamond-coated tip in contact mode (see Figure 5-1 (d)).[61] In the heterostructure considered here, since graphene is basically coated on the entire surface, the two-terminal measurement essentially provides local information about the relative conductivity of graphene in contact with different materials, including MoS_2 and SiO_2. Figures 5-1 (c) and (d) show the height and current profiles for the heterostructure, respectively. It is observed that graphene becomes less conductive when in contact with MoS_2, and there is no obvious dependence on the thickness of MoS_2. Since the interactions between graphene and MoS_2 are van-der-Waals like,[128] it is believed that the electronic structure of graphene is not significantly influenced by the underlying MoS_2. Therefore, the reduction in the conductivity of graphene implies that the Fermi level position, E_F, for graphene lying on MoS_2 is closer to the Dirac point, E_{Dirac},

than that on SiO_2, such that the density of states around the Fermi level is significantly reduced due to the cone-shaped band structure of graphene (see Figure 5-1 (d)).[129]

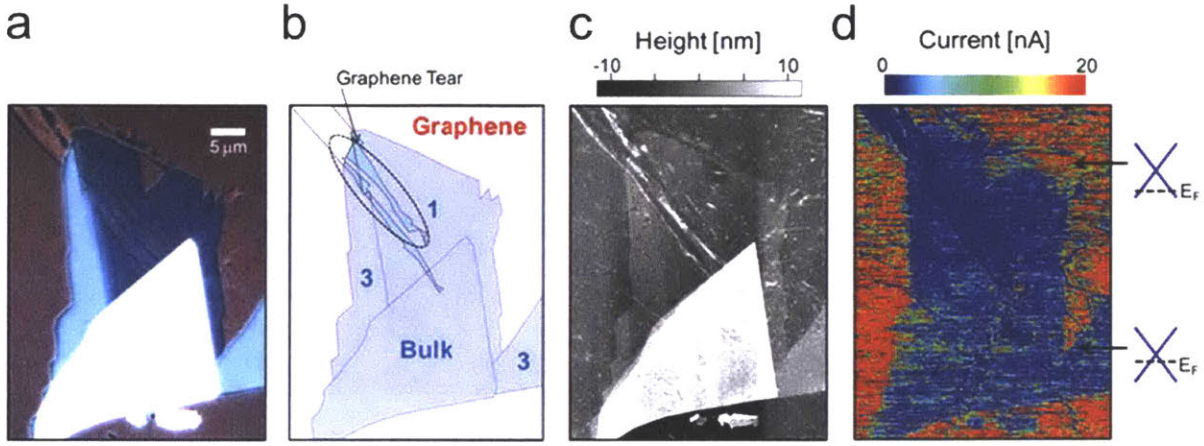

Figure 5-1: (a) Optical microscope image, and (b) topographical diagram for a CVD graphene-coated MoS_2 single crystal. The regions associated with monolayer (1), trilayer (3), and bulk MoS_2 are identified using Raman spectroscopy and labeled. (c) AFM topographical height and (d) current profiles using our c-AFM system (V_{Sample} = 0.5 V). The Fermi level positions of graphene associated with the regions lying on SiO_2(top) and MoS_2 (bottom) are also shown.

To further justify the Fermi level hypothesis, Raman spectroscopy was used to characterize the MoS_2-graphene heterostructure. Raman spectroscopy has demonstrated its versatility in 2D materials research.[114, 130] Here, in particular, since the Raman spectrum for graphene is very sensitive to the doping level,[131, 132] it allows us to resolve the Fermi level position locally. Accordingly, thousands of Raman spectra were taken to cover the entire sample. All prominent peaks were fitted with Lorentzian functions to extract peak position (ω), full width at half maximum (FWHM), and integrated intensity (I). The Raman spectrum for monolayer graphene consists of two prominent peaks, the G and $2D$ peaks, positioned at around 1580 cm^{-1} and 2640 cm^{-1}, respectively.[133] For each spectrum, the doping carrier density (n) and the Fermi level position relative to the Dirac point ($E_{Dirac} - E_F$) of graphene are calculated based on the position of the G and $2D$ peaks.[131] Specifically, the G peak position upshifts monotonically by increasing the doping level in graphene ($|E_{Dirac} - E_F| > 0$), while 2D peak position upshifts when p-doping (($E_{Dirac} - E_F$) < 0) and downshifts when n-doping (($E_{Dirac} - E_F$) < 0).[131] Following the empirical trajectories,[131] the obtained spectroscopic parameters allow us to quantify the Fermi level position, as well as the carrier density, n, locally.

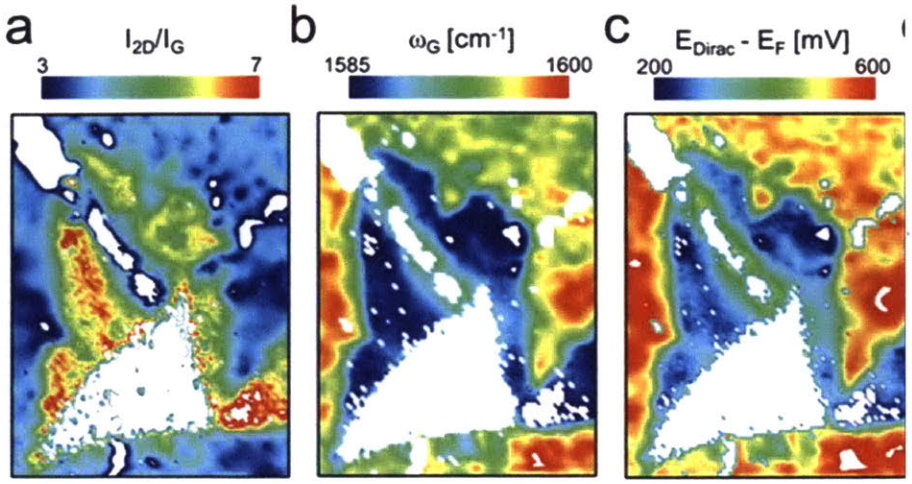

Figure 5-2: Spatial Raman maps for (a) I_{2D}/I_G, (b) ω_G, and (c) the calculated ($E_{\text{Dirac}} - E_{\text{F}}$) for the MoS_2–graphene heterostructure considered.

Figures 5-2 (a-c) show the spatial Raman maps of I_{2D}/I_G, ω_G, and the calculated ($E_{\text{Dirac}} - E_{\text{F}}$) of graphene, respectively. We notice that the two important peaks of graphene, however, become obscure on thick (> 3 layer) MoS_2 flakes, because of the broadening PL response and reduced light transmittance of thick MoS_2 flakes. For all the spectra of graphene, the 2D peak can be described by a single Lorentzian function with FWHM of 26 – 28 cm^{-1}, suggesting that the graphene is monolayer.[130] The average positions of the *G* and *2D* peaks for the graphene on SiO_2 (ϖ_G = 1593 cm^{-1} and ϖ_{2D} = 2648 cm^{-1}), as well as their intensity ratio (I_{2D}/I_G = 4), indicate that graphene is heavily hole-doped with a carrier density n = -2 x 10^{13}, corresponding to ($E_{\text{Dirac}} - E_{\text{F}}$) = 550 mV. On the other hand, the spectroscopic parameters for graphene in contact with MoS_2 (ϖ_G ~ 1586 cm^{-1}, ϖ_{2D} = 2644 cm^{-1}, and I_{2D}/I_G = 6) suggest that graphene is hole-doped with n = -1 x 10^{13}, corresponding to ($E_{\text{Dirac}} - E_{\text{F}}$) = 250 mV. It appears that additional electrons are transferred from MoS_2 to graphene such that graphene is "counter-doped" by the underlying MoS_2 flake, or in other words, that MoS_2 is hole-doped by graphene. The upshift of Fermi level position in graphene, as well as its independence on layer number of MoS_2, confirms our finding in the c-AFM characterization (see Figure 5-1(d)).

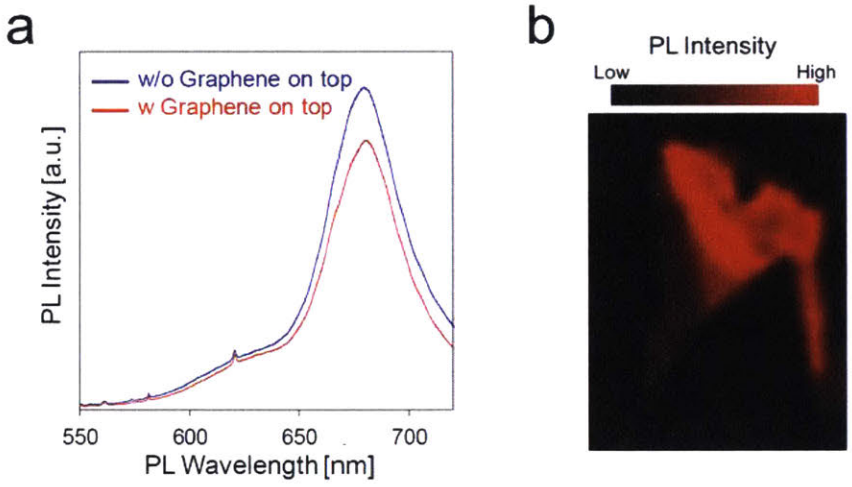

Figure 5-3: (a) Representative PL spectra for the regions of mnonolayer MoS2 with (red) and without (blue) graphene on top. (b) Spatial PL intensity map for the MoS_2–graphene heterostructure considered.

Monolayer MoS_2 is a semiconductor with a direct band gap of ~ 1.8 eV, which is optically active in the visible light range, generating strong photoluminescence (PL).[44] Since PL essentially describes the process of light emission after the absorption of photons, the quantum yield for the recombination of the hot carriers across the band gap plays an important role. A representative PL spectrum for monolayer MoS_2 under a green light excitation (λ = 532 nm) is shown in Figure 5-3 (a), and the PL intensity for each spectrum is calculated by integrating the emitted PL counts with respect to the wavelength from 532 to 720 nm. Figure 5-3 (b) shows the spatial map of PL intensity. As expected, due to the transition from indirect to direct band gap, the PL intensity in monolayer MoS_2 is much higher than that in trilayer and bulk MoS_2. For the region of monolayer MoS_2, since there is a tear formed in graphene (see Figure 5-1 (b)), we can quantify the effect of graphene on the change of PL in monolayer MoS_2, as shown in Figure 5-3 (b). We found that the integrated PL intensity, as well as the maximum intensity (at ~680 nm, corresponding to photon energy of ~1.82 eV), is considerably quenched by 20% when in contact with graphene. Apparently, the observed changes in PL intensity are not caused by the change of E_F in MoS_2, since the change in the carrier density in MoS_2 (Δn ~ -1 x 10^{13} cm^{-2}) is only associated with a downshift of Fermi level energy $\Delta E_F = \pi\hbar^2 \Delta n / m_e \sim -70\text{meV}$, where $m_e \sim 0.35 m_0$ is the

effective electron mass in MoS_2, and this shift is negligible compared to the dominant photon energy (~ 1.82 eV).[32] Considering the fact that graphene is about 98% transparent to visible light,[134] one possible mechanism for the observed quenching is the exciton splitting by the built-in potential formed between monolayer MoS_2 and monolayer graphene.[135] Specifically, exciton splitting occurs by injecting the photogenerated electrons from the conduction band of MoS_2 to graphene,[136] while the photogenerated holes in the valence band of MoS_2 cannot diffuse to graphene due to the built-in potential formed in the heterojunction.[135] Therefore, the recombination events, as well as the resulting photoluminescence, are significantly reduced.

5.2.2 Potential of BP-MoS_2 vdW Heterostructures

Motivated by the discovery of an isolated, stable monolayer graphene,[9] two-dimensional (2D) layered materials have generated significant research interest for new electronic and optical devices, suggesting their potential as candidate materials in future nanoelectronic applications.[3, 36, 37, 39, 90, 137, 138] Because they are necessarily atomically thin or of unit cell thickness, 2D layered materials may provide solutions to flexible, transparent electronics without the need for laborious and sophisticated device fabrication steps to achieve thin, high-performing channel regions required for conventional semiconducting materials. Besides graphene, the 2D materials that have been investigated most extensively to date are semiconducting transition metal dichalcogenides (TMDCs) such as MoS_2, $MoSe_2$, WS_2, and WSe_2.[2, 3] TMDCs are attractive because they can often be processed so as to demonstrate direct, permanent band gaps that graphene generally lacks. They also possess electronic and optical properties that are highly dependent upon the number of layers when in their few-layer (FL) forms due to quantum confinement.[5, 29, 104] The band gap transitions from indirect to direct when in the form of a single-layered crystal, rendering semiconducting TMDCs more intriguing for many optoelectronic applications.[44] There is still significant interest in new 2D materials with unique combinations of properties.[101, 103, 112, 139] Recently isolated 2D crystals of black phosphorus (BP)[140], the most stable allotrope of phosphorus at room temperature, has generated interest and excitement in the context of 2D materials due to several unique properties.[141] Similar to graphene and TMDCs, individual layers of

phosphorus are held together by van der Waals (vdW) interactions in the vertical direction. However, phosphorus atoms in each layer are bonded by sp^3 hybridization with neighboring atoms, resulting in a puckered honeycomb lattice structure[14] and in-plane anisotropy in its electronic and optical properties.[21, 142-144] Potential applications include plasmonic devices,[145] phonon transport engineering which could not have been possible with other 2D materials.[21, 146-148] However, BP and phosphorene exhibit air instability, undergoing considerable degradation upon exposure to oxygen or water, which requires a proper protection scheme to take full advantage of its superior intrinsic properties.[24, 149] In this work, we develop BP or bilayer (2L) phosphorene-MoS_2 vertical vdW heterostructure FETs as a solution to the air-degradation problem, while enhancing the photoresponses of devices and maintaining the conductivity of BP or 2L phosphorene crystals in the dark.

The hole mobility of BP devices can exceed 1,000 $cm^2 V^{-1} s^{-2}$ at 300 K but passivation is needed to prevent scattering defects from diminishing this property. Similarly, current on-off ratios in the range of 10^2-10^4 have been observed, and may be important for devices constituting high-speed logic circuits.[17, 19, 20] The optical band gap of a given BP system can be engineered over a wide range to accommodate the spectrum of incident electromagnetic energy by controlling its number of layers, also providing a material advantage.[15] While band gaps of most of TMDCs are greater than 1 eV,[3] first principles calculations showed that band gap of BP is expected to vary from ~ 1.5-2.0 eV in its single layer form down to around 0.3 eV when the crystal thickness is around 4 nm (~ 8 layers) or thicker, bridging the energy gap between graphene and TMDCs, making the material suitable for near- and mid-infrared applications such as optical telecommunications.[15] What makes this feature more intriguing is the fact that the direct band gap character is maintained regardless of its thickness—TMDCs show the direct gap character only in their monolayer form—which most of optoelectronic applications find valuable.[15] Also, whereas field-effect transistors (FETs) based on MoS_2 and WS_2 show monotonic n-type transport characteristics due to the strong Fermi-level pinning near the conduction band edge,[80, 150] recent studies have demonstrated that FL BP exhibits a noticeable p-type characteristic, thereby allowing it to be used as a p-type building block in vdW p-n heterostructures.[102] However, despite all of these advantages, BP has its critical drawback in that it is unstable in air, undergoing considerable degradation

upon exposure to oxygen or water, which requires a proper protection scheme to take full advantage of its superior intrinsic properties.[24, 149]

In this work, we introduce and develop BP-MoS_2 vertical vdW heterostructure FETs to provide a solution to the BP's air-degradation while enhancing photoresponse of the device and maintaining the dark conductivity of BP crystals. Toward this end, we first study the effectiveness of a FL MoS_2 as a vdW passivation layer under an ambient environment for an extended period of time and an elevated temperature, as well as photoluminescence (PL) at the heterojunction. When brought into contact with MoS_2, the PL intensity of bilayer (2L) phosphorene is observed to be quenched by about 29% compared to that of the BP alone, likely indicating the existence of a built-in electric field at the BP-MoS_2 junction which help dissociate photo-induced electron-hole (e-h) pairs. MoS_2-passivated FL BP crystals survived at least 3 weeks of air-exposure and 2 hours of annealing at 350 K in an argon environment, while exposed bare BP crystals are severely damaged and mostly disappeared. We then fabricate FET devices by depositing source and drain metal electrodes on both the exposed and MoS_2-passivated regions of the same BP flake for direct comparisions. In the dark, hole transport of a 2L-BP channel is barely impacted by the MoS_2-passivation layer on top while electron transport is obviously improved; the influence of the MoS_2 layer on the transport characteristic becomes less significant as the thickness of BP increases. Under illumination (λ = 600 nm), in general, higher photoconductivity is detected in the MoS_2-passivated regions than the exposed BP, with photoresponse enhancement due to the MoS_2 passivation is measured to be 78 % in the 2L device when V_g = 0 V. These results suggest that vdW passivation using thin MoS_2 films adds another strategic route toward air-protected BP-based nanoelectronics with improved photoconductivity. This work can be further expanded by introducing different TMDCs other than MoS_2 to fine-tune the band alignment with BP for specific target applications, which should aid in the development of air-stable high performing BP-based optoelectronic devices.

5.2.3 Photoluminescence at a BP-MoS_2 Heterointerface

BP-MoS_2 vertical heterostructures were constructed by conducting dry-transfer of thin MoS_2 films—whose shape was predefined in stripes—onto BP flakes which were micromechanically exfoliated on a 100 nm thermally grown SiO_2 on a highly doped Si wafer in an N_2-filled glovebox with O_2 concentration less than 0.5 p.p.m. Large-area trilayer MoS_2 films were grown by chemical vapor deposition (CVD) process using solid S and $MoCl_5$ as precursors on a Sapphire substrate in a vacuum tube furnace.[151] The thickness of the MoS_2 films was verified by Raman spectroscopy and AFM height measurements. Then, standard ultraviolet lithography was utilized to define stripes on the MoS_2 film, which was followed by removal of exposed areas of MoS_2 in oxygen plasma generated by an electron cyclotron resonance (ECR) reactive plasma etch system. The shape-defined MoS_2 films were then peeled off from the substrate following the surface-energy-assisted method introduced by Gurarslan *et al.*[152] In order to avoid water exposure to BP crystals, the peeled-off MoS_2 film was placed on a PDMS support, which followed by a baking at 80-90°C in vacuum for 2 hr to remove water residues and then the MoS_2/PS/PDMS assembly is brought in to a N_2-filled glove box. BP flakes were micromechanically exfoliated on a 100 nm thermally grown SiO_2 on a highly doped Si wafer in the glove box. The MoS_2/PS/PDMS stack was put on top of the exfoliated BP flakes and was baked at 120°C for 30 min to facilitate intimate adhesion as well as to spread the polymer layers to remove wrinkles that could have formed during the transfer process. Finally, the assembly was immersed in toluene to remove the PS/PDMS stack. This way, BP crystals become partially covered by MoS_2 stripes—allowing for direct comparison between exposed and MoS_2-passivated regions on the same BP flake—without exposure to air or water.

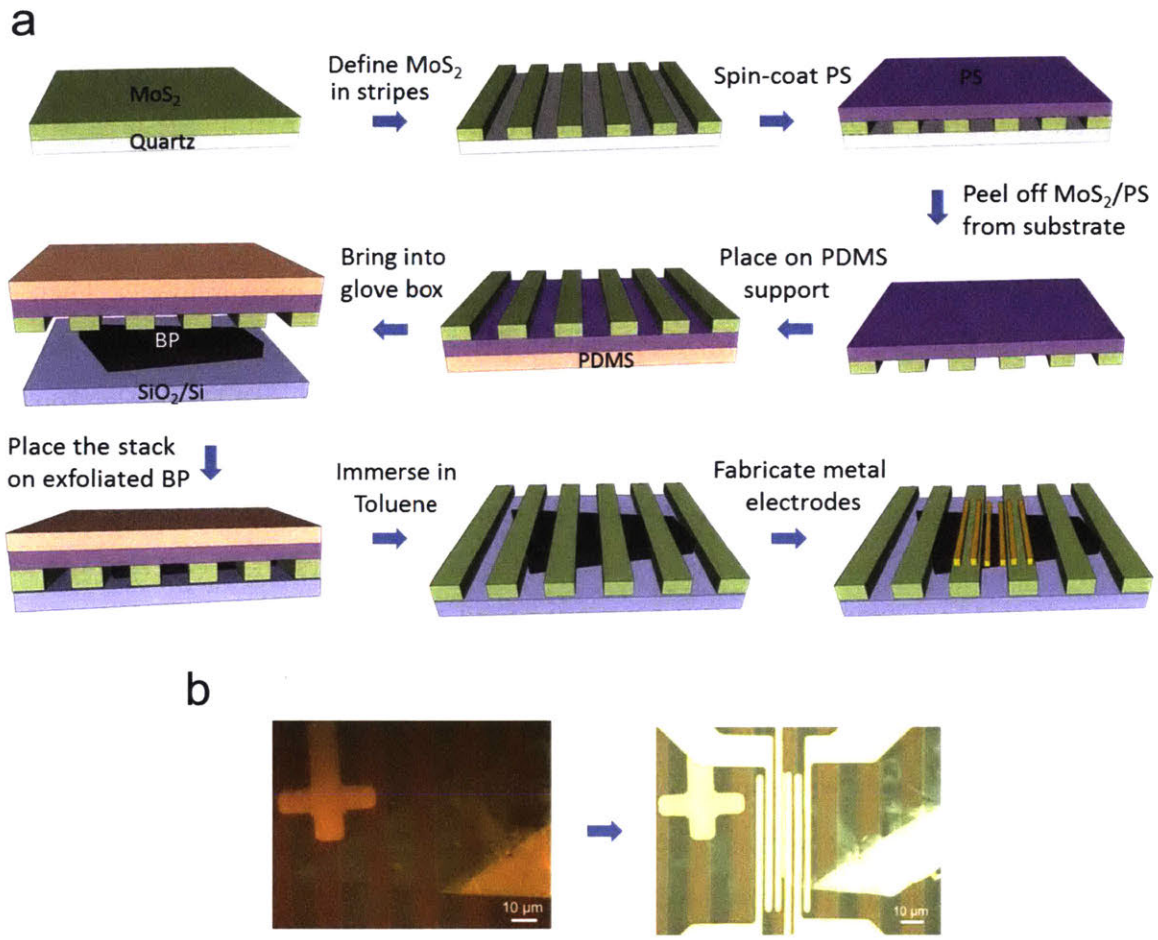

Figure 5-4: (a) Schematic illustration of BP-MoS_2 vertical heterostructure fabrication process. (b) Optical images taken after the dry transfer of MoS_2 (left), and metal electrodes deposition (right).

A fabricated 2L BP-MoS_2 heterostructure was first identified by optical contrast, and then its layer number was verified using atomic force microscopy (AFM), and Raman spectroscopy—Figure 5-5 (b), (c), and (d), respectively. The upper panel of Figure 5-5 (d) shows a representative Raman spectrum of the BP-only area where the three signature Raman peaks of BP, attributing to the A_g^1, B_{2g}, and A_g^2 phonon modes, are prominently observed. And it is clearly observed that in the BP-MoS_2 region shows corresponding Raman peaks of both BP and MoS_2 with the peak positions barely shifted from that of each

homogenous crystal, corroborating successful fabrication of the heterostructure without impacting on the vibration modes of the component layers, as shown in the bottom panel.

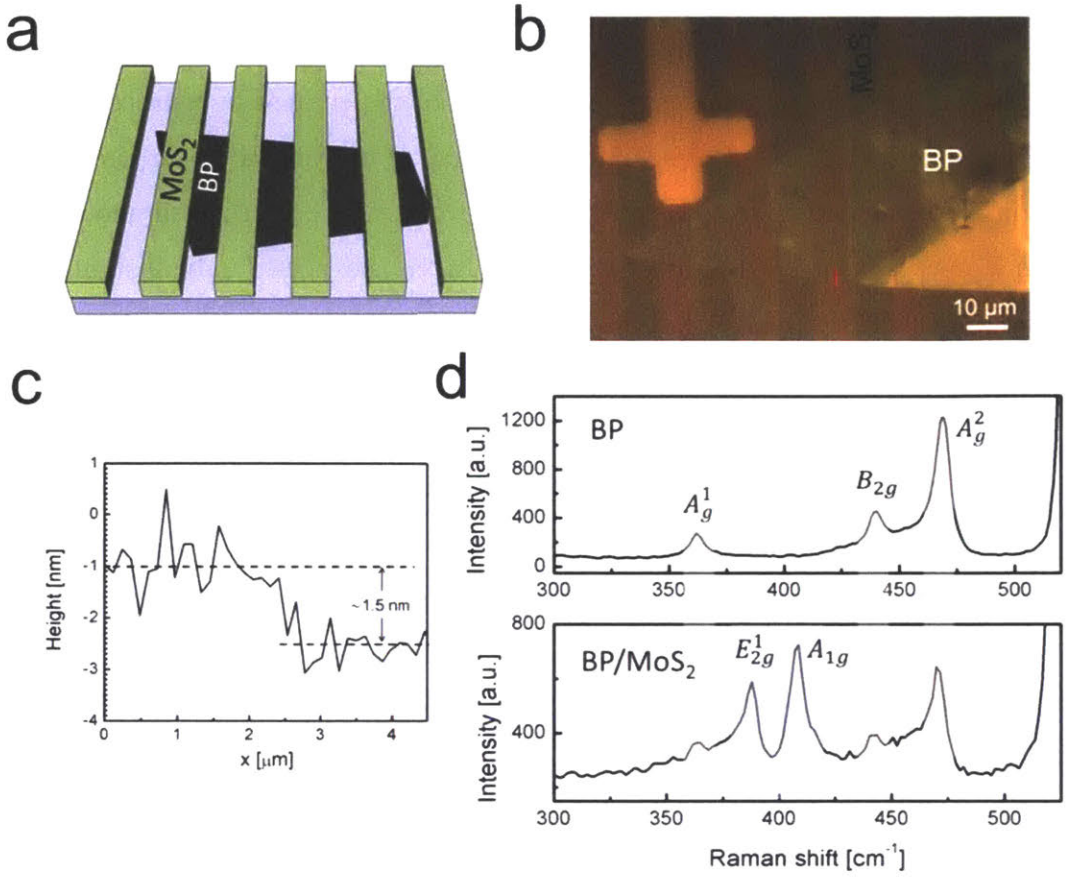

Figure 5-5: (a) Schematic illustration of the BP-MoS_2 heterostructure on a SiO_2 (100nm)/Si substrate where trilayer MoS_2 stripes cover portions of the underlying BP flake, resulting in MoS_2-passivated and exposed regions on the same BP flake. (b) Optical microscope image of a BP-MoS_2 heterostructure, where BP is bilayer. (c) AFM height profile of the 2L BP crystal taken along the red line marked in (b). (d) Representative Raman spectra taken on the exposed (top) and MoS_2-passivated (bottom) BP regions.

The AFM height profile obtained along the red line marked in Figure 5-5 (b) indicates the thickness of the BP flake is ~ 1.5 nm which is slightly larger than the theoretical value of ~ 1.2 nm for a 2L BP. This has commonly been seen in measuring thickness of other 2D materials using the AFM, and it might have been worsened in the case of BP by partial oxidation and water molecules adsorbed on the surface as the AFM measurements were conducted in ambient conditions after all the electrical measurements were completed.[153] Bilayer nature of the BP crystal was further confirmed by representative PL spectra shown in

Figure 5-6 taken under a green laser excitation (λ = 532 nm), where a strong PL signal at around 940 nm (1.32 eV) due to its direct gap character irrespective of its layer number.[154] Notably, when the BP is brought into contact with MoS_2, its maximum PL intensity is considerably quenched by about 29% and the peak position is blue-shifted by ~ 10 nm. One possible route for the quenching is reabsorption of the emitted light from BP by the MoS_2 passivation layer. Considering the optical band gap of trilayer (3L) MoS_2 is ~1.4 eV[5] as well as its indirect gap nature, the probability of the events where the emitted photons from the 2L BP with an energy of 1.32 eV are absorbed by MoS_2 is expected to be insignificant. Another plausible mechanism for the observed quenching is the exciton dissociation by the built-in electric field formed at the BP-MoS_2 interface. As illustrated in the inset in Figure 5-6 a type-II band alignment forms at the heterointerface in which a valence band offset is larger than the counterpart of the conduction band. Because the exciton binding energy of 2L BP crystals sitting on a SiO_2 substrate is calculated to be 0.25 eV,[23] these noticeable band offsets promote exciton dissociation events, thereby resulting in considerably reduced recombination events. The shift in the PL maximum peak position upon contacting MoS_2 may be due to the possibility that increased thickness in the heterostructure gives rise to the reduced quantum confinement effect, affecting its electronic band structures.

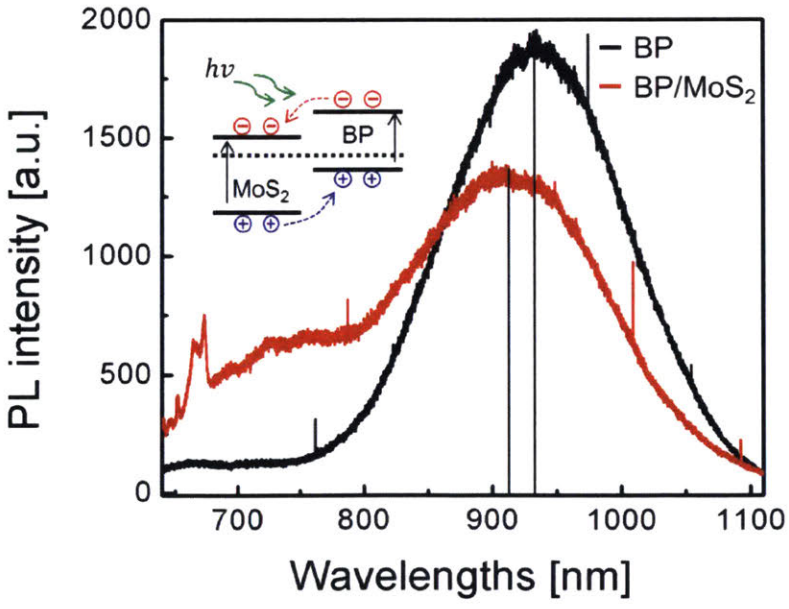

Figure 5-6: Representative PL spectra of the exposed (black) and MoS_2-passivated (red) BP. The inset illustrates a band alignment at the heterointerface.

5.2.4 MoS_2 as a Van der Waals Passivation Layer

To test the effectiveness of CVD MoS_2 as a protection layer we characterized the BP-MoS2 heterostructures using an optical microscope and Raman spectroscopy as the samples are left under exposure to air or an elevated temperature (350°C). It has been reported that BP crystals quickly degrade in ambient conditions within a few days, which is likely due to irreversible conversion of BP in to PO_x by ambient adsorbates.[24] The left, center, and right panels of Figure 5-7 show optical microscopic images of a few-layer BP flake which is partially covered by 3L CVD MoS_2 upon the completion of the heterostructure fabrication, after 1 and 3 weeks of exposure in air, respectively.

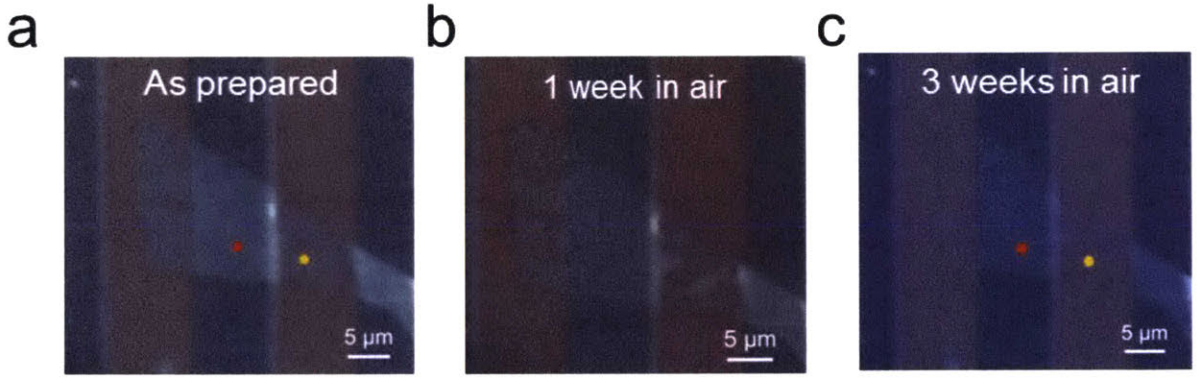

Figure 5-7: Optical images of a BP-MoS_2 heterostacks acquired upon fabrication (a), after 1 (b) and 3 weeks of exposure to air (c).

In a week (Figure 5-7 (b)), portions of the exposed BP region have undergone severe deterioration while the MoS_2-passivated area remains almost intact. After 3 weeks of air-exposure, as shown in Figure 5-7 (c), most of the exposed BP is etched away barely leaving traces of BP crystals to be identified, whereas no noticeable change is observed in the MoS_2-capped BP. To further confirm this observation, Raman spectroscopy measurements were taken on both the exposed and passivated locations of the BP flake (Figure 5-8). In the upper panel, MoS_2-protected BP clearly shows its signature peaks—A_g^1, B_{2g}, and A_g^2 peaks—even after 3 weeks of air-exposure although the peak intensity of BP peaks decreased a little when compared to that of MoS_2, which is stable enough to withstand this level of ambient conditions over an extended period of time. Also, the spectra of the capping MoS_2 before and

after the exposure are almost identical, in both peak shift as well as intensity, excluding a possibility of reactions at the BP-MoS_2 interface. On the other hand, the Raman spectra acquired at the exposed BP area after 3-week-exposure to air shows no discernable peaks associated with BP crystals, corroborating the observation under an optical microscope.

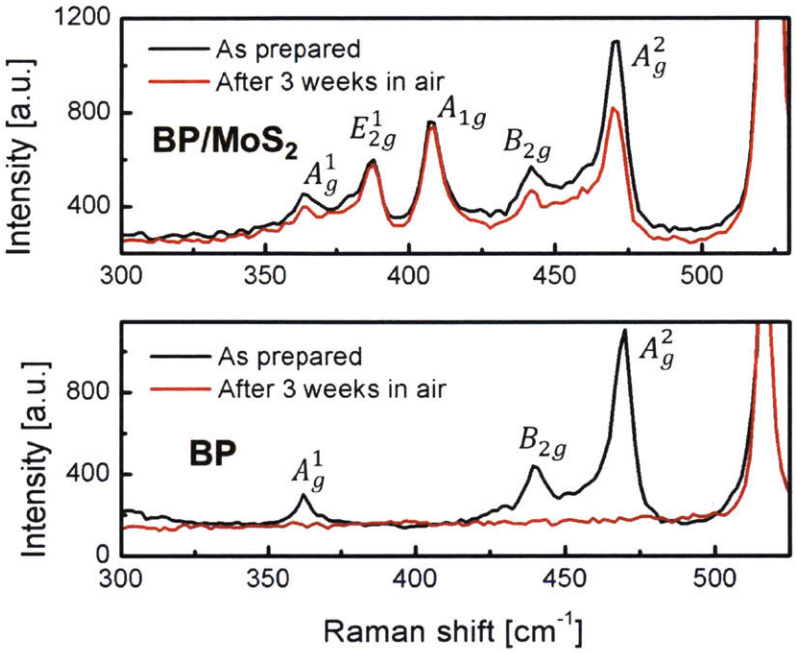

Figure 5-8: Representative Raman spectra taken at exposed (bottom) and MoS_2-passivated BP (top) upon preparation and in 3 weeks in air.

In addition, the thermal stability of a few-layer BP passivated by a 3L CVD MoS_2 has been tested at 350°C under an Ar envirionment for 2 hours, as provided in Figure 5-9 (a) where the left and right panels present optical images of the BP-MoS_2 heterostructure before and after the annealing, respectively. Similar to the air-stability case, the exposed BP crystal has mostly disappeared after the annealing while the MoS_2-capped ones can still be observed by optical contrast. Again, Raman analysis was conducted at both the exposed and passivated locations to verify the quality of the BP crystal upon annealing. Raman spectra shown in Figure 5-9 (b) show that BP underneath the MoS_2 layer has survived the annealing condition, with somewhat reduced peak intensity, while the exposed area has almost completely been etched away. Therefore, a thin CVD MoS_2 film could be considered as an ultrathin, effective

passivation layer to protect few-layer thin BP crystals from an ambient and an elevated temperature conditions over an extended period of time.

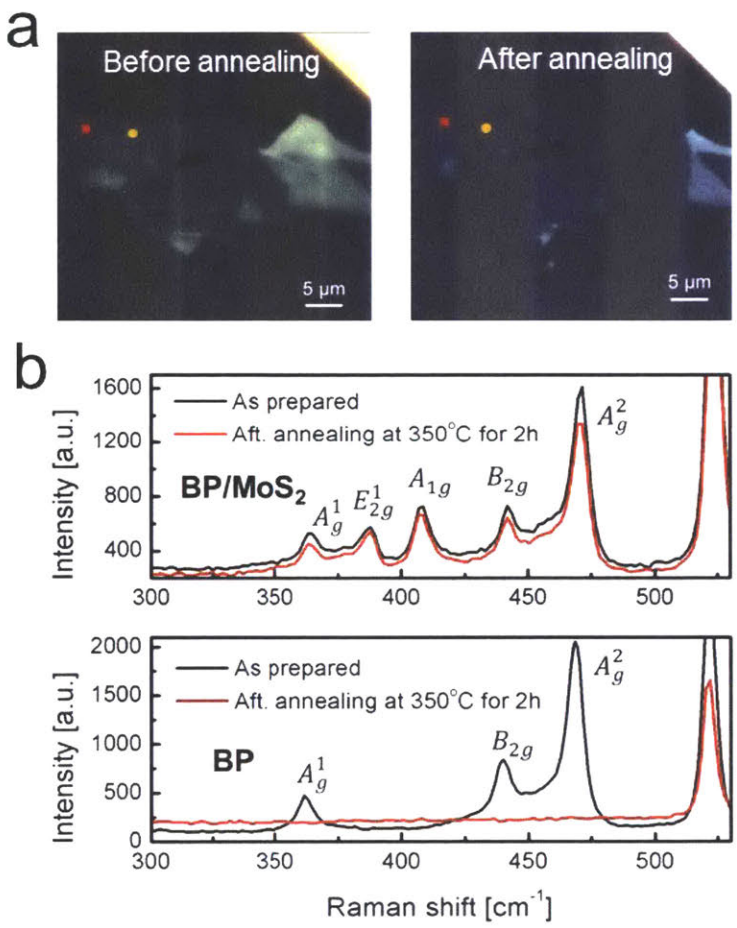

Figure 5-9: (a) Optical images of a BP-MoS_2 heterostacks acquired upon fabrication (left) and after annealing under Ar environment at 350°C for 2 hours (right). (b) Representative Raman spectra taken at exposed (bottom) and MoS_2-passivated BP (top) upon preparation and the annealing.

5.2.5 Transport Characteristics of BP-MoS_2 Heterostructure-Based FETs

FET devices based on the BP-MoS_2 heterostructures were fabricated to investigate the influence of the MoS_2 passivation layer on the electrical characteristics of the underlying BP crystals. Figure 5-10 shows a schematic illustration (top) and an optical image (bottom) of the heterostructure device where the source and drain electrodes are located on both the BP-

only and BP-MoS_2 regions on the same BP flake. After fabricated inside the glove box, on top of 100 nm SiO_2 on highly doped a Si wafer which was used as a global back gate, the heterostructures were transported for further metal electrodes deposition in an N_2-filled container to minimize air-exposure. Then, the source and drain metal electrodes with a channel length of 1.5 μm were patterned on both the exposed and MoS_2-passivated areas of a target BP flake using ultraviolet photolithography, followed by the deposition of Ti (20 nm) / Au (60 nm) as the contact metal *via* electron beam evaporation. This way, we were able to fabricate exposed and MoS_2-passivated BP FET devices on the same BP flake, allowing for direct comparisons.

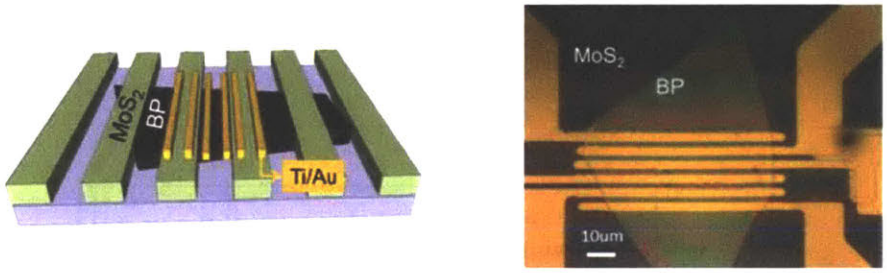

Figure 5-10: Schematic illustration of the FET devices (left) and an optical image of the 13 nm device (right).

In order to explore the effect of BP thickness on device performance, 4 different FETs out of 1.5 (2L), 5, 13 and 20 nm-thick BP flakes were fabricated with the thickness of the MoS_2 passivation layer kept constant at 3L. The AFM measurements to verify the thickness of the samples were performed in tapping mode after the electrical testing has been completed to avoid crystal degradation by air-exposure as well as possible physical damage during the imaging. The electrical measurements of the devices were carried out in an ambient environment at room temperature.

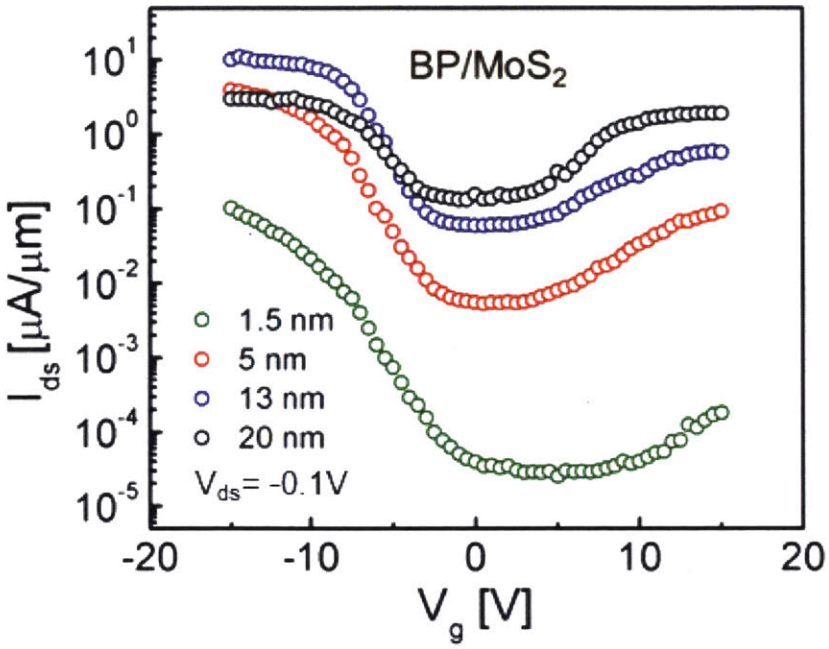

Figure 5-11: Transfer characteristics (at V_{ds} = -0.1 V) of the MoS_2-passivated BP channels of varying thicknesses—1.5 (2L), 5, 13, and 20 nm.

In Figure 5-11, transfer characteristics of the BP-MoS_2 channels with different BP thicknesses are plotted at constant source-drain voltage, V_{ds} = -0.1 V. In general, p-type transport characteristics (i.e. on-current increases prominently as the gate voltage (V_g) sweeps towards negative voltage) were observed, consistent with previous reports of BP FETs,[31, 32, 43] indicating that the metal electrodes interact with the BP channel through the thin MoS_2 passivation layer and the Fermi level gets pinned closer to the valence band of the BP. The transport within the channel is largely determined by the bottom BP channels rather than the top MoS_2 layer. This behavior is more prominent in devices based on thinner BP flakes while electron transport becomes important when BP thickness reaches 20 nm (black circles in Figure 5-11), showing a near ambipolar behavior. Also, there exists an obvious trend that the minimum off-current monotonically increases whereas the on-off current ratio (I_{on}/I_{off}) decreases as BP thickness increases—about 5×10^3 and 3×10^1 for the 2L and 20 nm devices, correspondingly (which is an underestimation of the intrinsic value of the devices given the curves do not reach the saturation within the range of voltage sweep used in this work). This can be explained by the combination of a significant change in the band gap of BP with the layer number and a consequent Schottky barrier height change at the interface

with the metal electrodes, which will be discussed in more detail below. The maximum on-current, however, does not exhibit the monotonic upward trend and even decreases as the BP thickness increases from 13 to 20 nm, which could be explained by the interplay between charge screening and interlayer coupling that can be used to estimate current distribution throughout the individual layers of a 2D layered channel region.[44, 45] The field-effect mobility of the BP-MoS_2 regions is calculated based on the method of transconductance.[46] Specifically, the transport transconductance, g_m, is given by:

$$\mu = \frac{L}{W \times C_{ox} \times V_{ds}} \left| \left(\frac{\partial I_{ds}}{\partial V_g} \right) \right|_{V_{ds}} \tag{20}$$

where L and W correspond to the effective channel length and width between drain and source electrodes, respectively. C_{ox} is the capacitance of the gate oxide, I_{ds} the drain-source current, V_{ds} the drain-source voltage, and V_g the back-gate voltage. The estimated field-effect hole mobility values (μ) are: 0.5, 15.7, 50.6, and 14.7 $cm^2V^{-1}s^{-1}$ for 1.5 (2L), 5, 13, and 20 nm devices, respectively. These are comparatively lower than previously reported hole mobility predictions for exposed[17] and AlO_x-encapsulated[24] BP devices, which could be due to increased scattering events from additional defect, trap and impurity states at the BP-MoS_2 interface added during the imperfect dry transfer of MoS_2 thin films.

More detailed results of the 2L device are provided in Figure 5-12 where direct comparisons between the BP-only, BP-MoS_2, and MoS_2-only channels can be made.

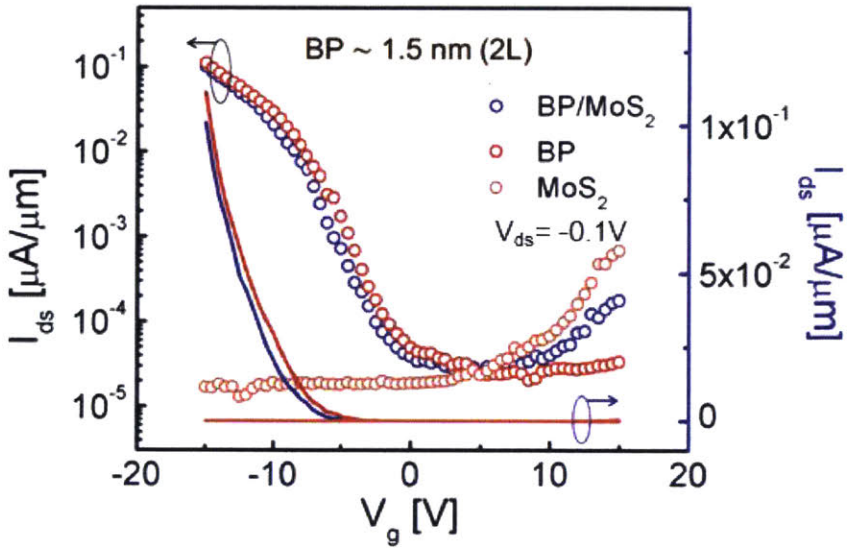

Figure 5-12: Detailed transport characteristics of the 2L device where red, blue, and orange circles indicate I_{ds}-V_g traces for the BP-only, BP-MoS_2, and MoS_2-only regions, respectively.

Firstly, the BP-only channel (red circles) exhibits an obvious p-type characteristic with a negligible level of electron transport recorded under a positively applied V_g up to 15 V. In contrast, the MoS_2-only channel (orange circles) shows an n-type behavior with no discernable hole transport, but with maximum I_{ds} of only ~ 7×10^{-4} μA/μm which is around a hundred times lower than that of the BP-only and with a I_{on}/I_{off} of mere ~ 50. The much lower conductance of the MoS_2 channel than the BP channel even with one more layer available for charge carrier transport could be in part attributed to the heavier effective mass in MoS_2 and the low crystal quality of the CVD-grown MoS_2 film, which is a common trade-off for large area 2D films grown by the CVD process. In the BP-MoS_2 region (blue circles), under a negative back gate voltage, the current trace is very close to that of the BP-only channel with only a little decrease in the current level, implying that a FL-thin MoS_2 passivation layer does not add noticeable impedance and the tunneling barrier in the vertical direction is relatively insignificant in comparison to the Schottky barrier that forms in the lateral direction toward the channel. However, interestingly, as V_g changes its polarity and sweeps to large positive voltages, the BP-MoS_2 channel begins to show distinct electron transport although its magnitude is slightly lower than the MoS_2-only. Since the carrier transport through the BP and MoS_2 layers can be considered independent in the BP-MoS_2 region,[47] the transport pathways can be simplified using a resistor network schematically illustrated in Figure 5-13, where carrier injection into the BP channel encounters an additional tunneling barrier across the upper MoS_2 passivation layer.

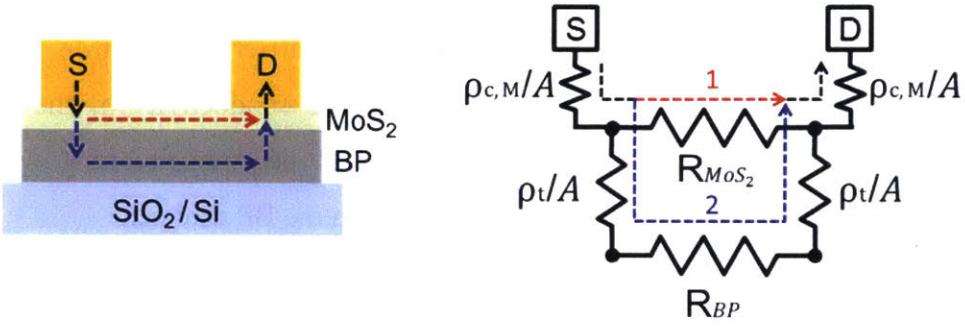

Figure 5-13: A simplified resistor network model that represents carrier transport pathways in the BP-MoS_2 region.

The total device conductivity can be expressed as:

$$\sigma = (2\,\rho_{c,M}/A + R_{ch})^{-1} \tag{21}$$

where,

$$R_{ch}^{-1} = R_{MoS2}^{-1} + (2\,\rho_t/A + R_{BP})^{-1}$$

and $\rho_{c,M}$ is the contact resistivity at the metal electrodes-MoS_2 interface, R_{ch} the channel resistance, ρ_t the vertical tunneling resistivity across the MoS_2 passivation layer, A the electrodes contact area, and R_{MoS2} and R_{BP} the individual MoS_2 and BP channel resistances, respectively.

When negative V_g is applied, $R_{MoS2} \gg R_{BP}$ which leads to $R_{ch} \sim (2\,\rho_t/A + R_{BP})$ and, consequently, $\sigma = \left[2\,(\rho_{c,M} + \rho_t)/A + R_{BP}\right]^{-1}$. Hence, the BP channel dominates the overall carrier transport, as indicated as blue dotted arrow in Figure 5-13, with the MoS_2 acting mainly as an encapsulation layer rather than a conductive channel for charge carrier transport. From the observation that almost the same I_{ds}-V_g characteristics were measured for BP-only and BP-MoS_2 with a large negative applied V_g, it is expected that $\rho_{c,BP} \sim \rho_{c,M} + \rho_t$; but, $\rho_{c,M} + \rho_t$ becomes a bit more important as a smaller magnitude of negative V_g is applied. In the positive V_g regime, R_{MoS2} (R_{BP}) decreases (increases) that carrier transport along the top MoS_2 channel (red dotted passage in Figure 5-13) becomes of significance. For V_g larger than ~5 V, the BP-MoS_2 shows much higher channel conductivity than the BP-only, but still lower when compared to the MoS_2-only. This may also be because of more defects, scattering sites introduced at the heterointerface as well as a lower gating efficiency due to the charge screening by the underlying BP channel. Conceptual understanding of this observation can be aided by the gate-dependent band diagrams, schematically illustrated in Figure 5-14. Under a positive V_g (**i**), the Schottky barrier for electron injection to the conduction band of MoS_2 becomes thin such that the conductivity of the MoS_2 channel increases while hole injection to the valence band of BP becomes favorable when a negative V_g is applied (**ii**), resulting in improved conductivity in the BP channel.

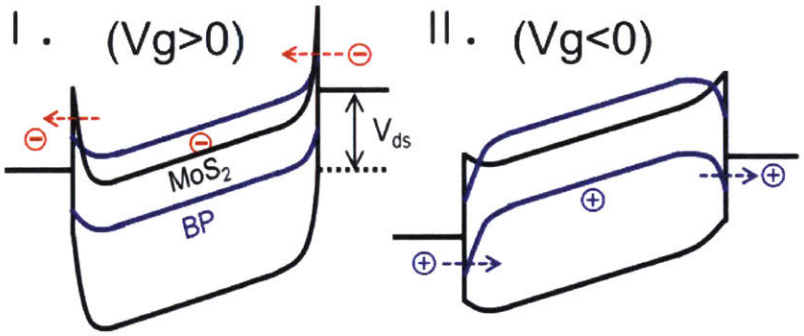

Figure 5-14: Band diagrams under different external conditions: carrier transport in the dark when (i) $Vg > 0$ and (ii) $V_g < 0$

When the thickness of BP flakes is 5 nm or more (see Fig 5-15), because a BP channel has many more layers for current passage than MoS_2, $R_{MoS2} \gg R_{BP}$ over the whole range of V_g so that the current flow is largely determined by the BP channel, causing for BP-MoS_2 regions to show an almost identical I_{ds}-V_g curve to corresponding BP-only regions—slightly lower current values were due to the introduced tunneling resistivity from the MoS_2 passivation and defect, scattering sites added during the heterostructure fabrication process. Thus, our results suggest that thin MoS_2 films can be considered as a candidate passivation layer which in general does not deteriorate transport characteristics of BP FETs while even boosting electron transport when an ultrathin BP flake is used—2L in this study.

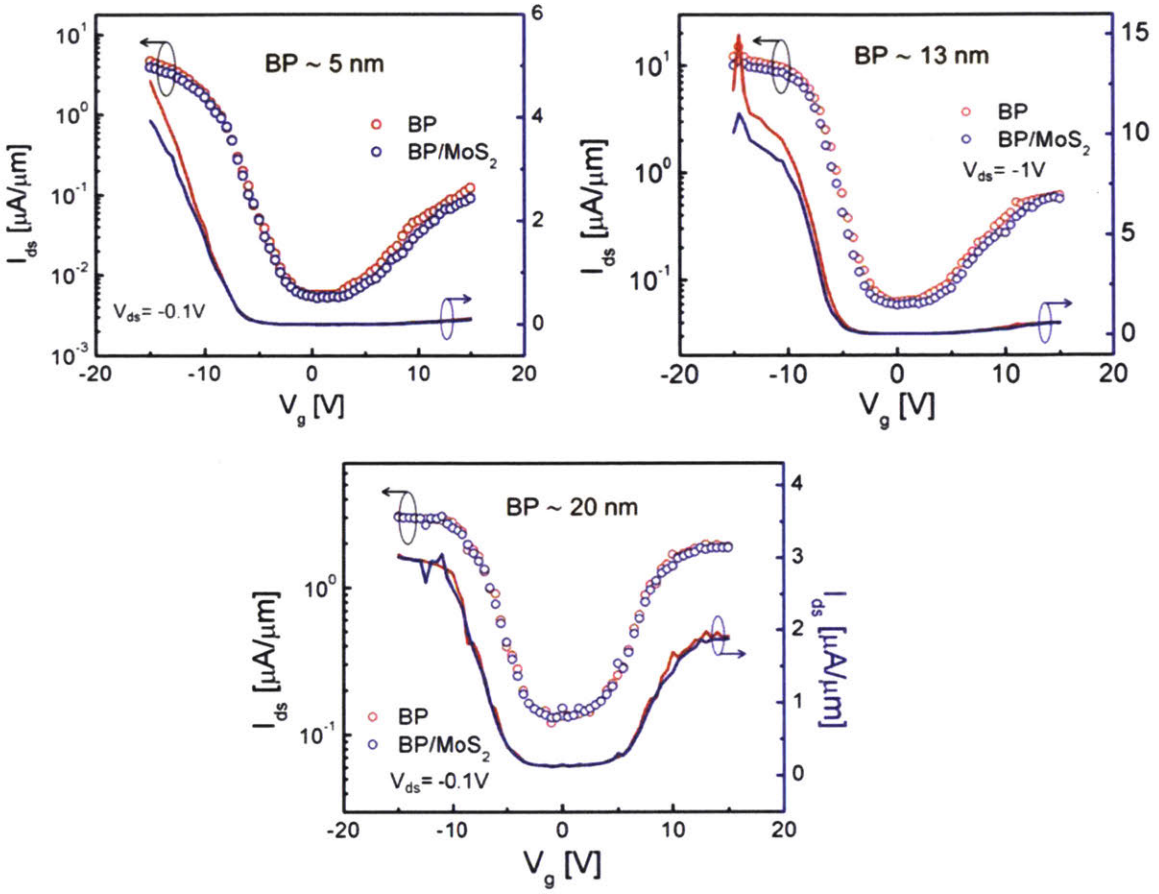

Figure 5-15: Transfer characteristics of the 5, 13, and 20 nm devices where red and blue circles represent the BP-only and BP-MoS_2 regions, respectively.

5.2.6 Photoresponse of BP-MoS_2 Heterostructure-Based FETs

The transfer characteristics are also acquired under laser illumination (λ = 600 nm; 0.01 W/cm^2) to study the impact of the MoS_2 passivation on the photoresponse of the devices. Figures 5-16 show the I_{ds}-V_g characteristics of the devices under illumination as well as in the dark measured at V_{ds} = -0.1 V.

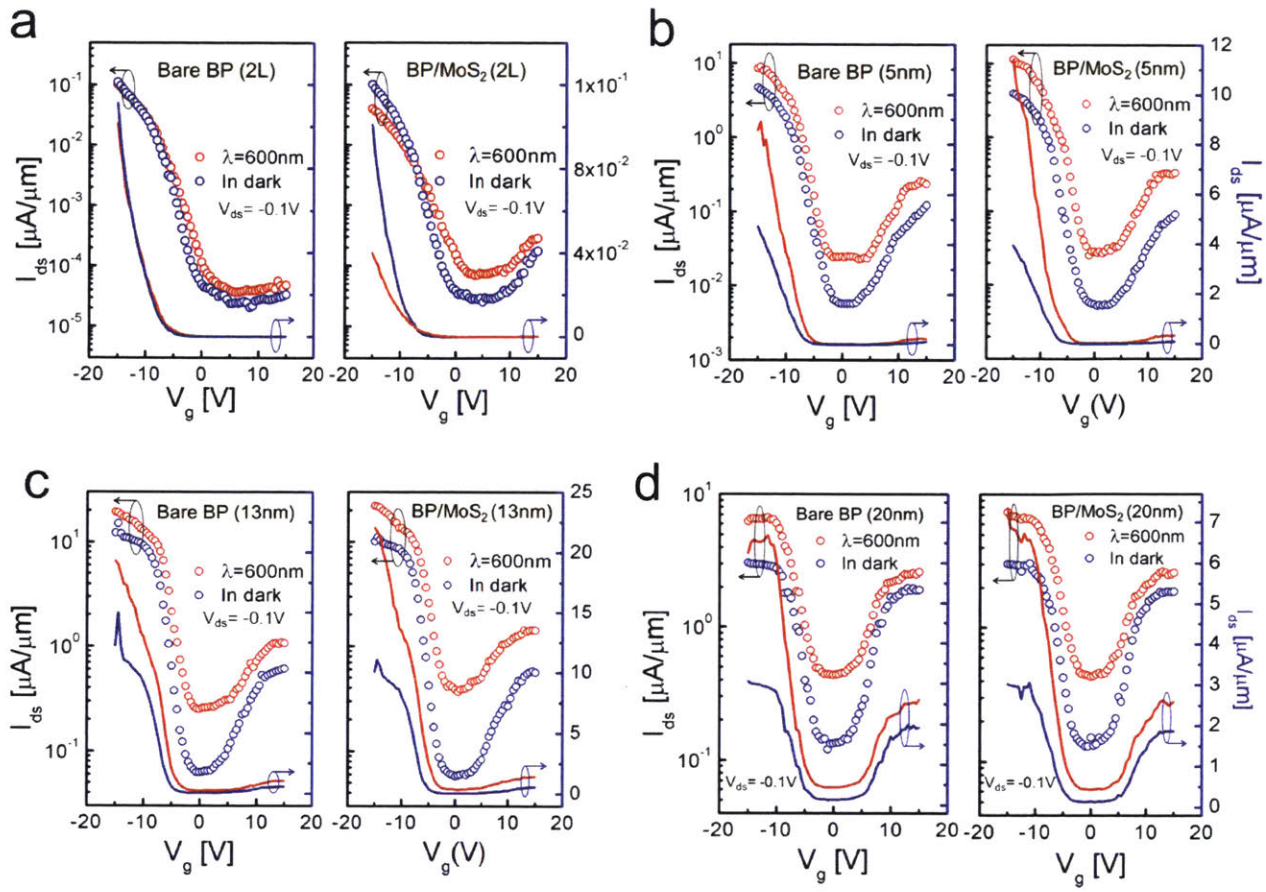

Figure 5-16: Thickness-dependent photoresponse. (a) Electrical characteristics of the BP-only (left) and BP-MoS_2 regions in the 2L device in the dark (blue circles) and under illumination (red circles, λ = 600 nm) with applied V_{ds} = -0.1 V. (b-d) Electrical characterization of the 5, 13, and 20 nm devices under the same measurement conditions as (a).

Interestingly, the BP-only and BP-MoS_2 regions in the 2L BP device showed apparently different responses from each other (Figure 5-16 (a)). In the BP-only region, over most of the gate voltage sweep, a higher current was recorded upon illumination (red line) compared to that obtained in the dark (black line), which can be attributed to increased conductivity due to generated extra charge carriers upon light absorption (photoconductivity). But, this photoconductivity decreases as a V_g sweeps to a larger negative voltage so that even a slightly lower current was observed when V_g < -12 V. This observation becomes more prominent in the BP-MoS_2 region, as presented in the right panel of Figure 5-16 (a). Compared to the BP-only case, the degree of current enhancement is greater in the BP-MoS_2 area in the positive V_g regime as well as with a moderate negative V_g up to about -7 V, at

which the photoconductivity converts into a negative response. With no electrostatic gating (V_g = 0 V), photo-induced current of the BP-only region, $PR_{exp} = I_{L,exp} - I_{D,exp}$, is measured to be 1.3×10^{-2} mA/W while that of the BP-MoS_2 region was 1.3×10^{-2} mA/W and photoresponse enhancement by the MoS_2 passivation layer, ΔPR, to be 78 % where the ΔPR is defined as:

$$\Delta PR(\%) = \frac{PR_{psv} - PR_{exp}}{PR_{exp}} = \frac{(I_{L,psv} - I_{D,psv}) - (I_{L,exp} - I_{D,exp})}{(I_{L,exp} - I_{D,exp})} \times 100$$

where $I_{L(D),psv(exp)}$ is the current measured under illumination (in the dark) at the BP-MoS_2 (BP-only) region.

This increased photoconductivity attributed to MoS_2 suggests improved exciton dissociation efficiency by the built-in electric field at the BP-MoS_2 p-n interface—previously evidenced by the significant PL quenching—which exists throughout the whole active channel area. This provides an additional driving force for separation of photo-generated e-h pairs. Some additional light absorption by the MoS_2 passivation layer may contribute to the photoconductivity by generating additional photo-induced e-h pairs, which can then be separated for electrons (holes) to be injected into the conduction (valence) band of the BP, resulting in increased channel conductivity.

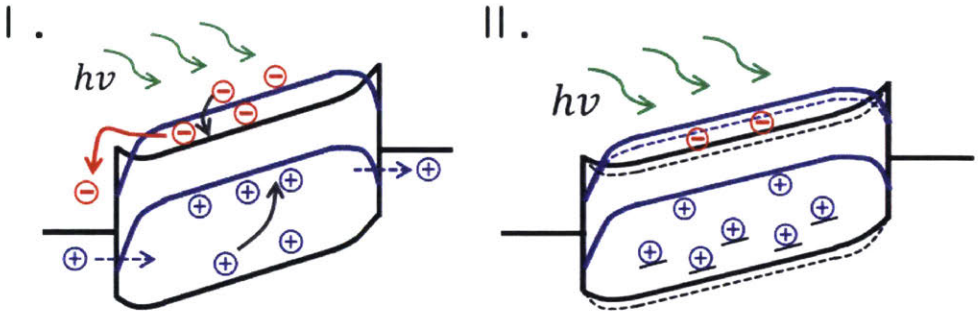

Figure 5-17: Band diagrams under different external conditions: (i) upon illumination with Vg < 0; (ii) conceptual explanation of the observed photo-induced doping effect.

The observed current reduction in the BP-MoS_2 region upon illumination under a large negative V_g may originate from a photo-induced doping effect previously reported in 2D materials.[48] Under light illumination, a portion of the photo-generated charge carriers (holes in this case) are trapped in localized states, as sketched in Figure 5-17 (ii). Then, the trapped holes partially screen a negatively applied V_g which reduces gating efficiency, leading to a horizontal shift of the I_{ds}-V_g characteristic toward a more negative gate voltage. Therefore, the photoresponse in the 2L BP-MoS_2 can be interpreted as the combination of a noticeable increase in photoconductivity as well as the photo-induced doping effect. Figure 5-16 (b) shows the transfer characteristics of the 5 nm devices at the BP-only (left) and BP-MoS_2 (right) regions in the dark and with illumination under the same conditions as the 2L device. Here, higher photoconductivity was observed compared with the 2L device with the recorded PR_{exp} and ΔPR as 2.1 mA/W and 22 %, respectively. That is, the absolute amount of photocurrent generation was bigger and dominates while the photoresponse enhancement due to the MoS_2 passivation layer decreased when no gate voltage was applied (V_g = 0 V). In contrast to the 2L device, the photoconductive effect dominates the process and no noticeable photodoping effect was observed in both BP-only and BP-MoS_2 regions so that PR_{exp} and ΔPR of the device reached 2.5×10^2 mA/W and 71 % at Vg = -11 V. At V_g = 0 V, as the thickness of BP increases, a continued increasing trend in PR_{exp} with 2.1×10^1 and 3.3×10^1 mA/W for the 13 and 20 nm devices, respectively; but, the enhancement by the MoS_2 passivation has decreased to mere 1 % in the 20 nm device. Thus, MoS_2 passivation is shown to have a significant influence on carrier transport by introduction of channels for electron conduction as well as photoresponse in atomically thin FL BP devices. As the nature of BP crystals approaches its bulk form, the MoS_2 functions primarily as a passivation layer and its role as an electron transport/photoresponse enhancer becomes relatively insignificant.

5.3 Conclusion

In conclusion, we developed BP-MoS_2 vertical vdW heterostructure FETs and demonstrated that a FL MoS_2 film can be utilized not only as an effective passivation layer but as a photoresponse booster. When left in an ambient environment a 3L CVD MoS_2 successfully preserved an underlying FL BP crystal up to 3 weeks while exposed portions of the same crystal was completely deteriorated, which is confirmed by Raman analysis. Moreover, the MoS_2 passivation layer provided BP with improved thermal stability such that the MoS_2-passivated regions survived 2 hours of annealing at 350°C in an Ar environment with the exposed parts entirely etched out. When in contact with MoS_2, the PL signal from a 2L BP crystal was quenched by 29% compared to a bare BP crystal possibly due to an internal electric field that forms at the BP-MoS_2 vdW p-n junction, which could help dissociate photo-induced e-h pairs. FET devices fabricated based on BP flakes with varying thicknesses showed an interesting thickness dependent effect of MoS_2 passivation layer on electrical characteristics and photoresponse of the devices. In the dark, electron transport of a 2L-thin BP channel was noticeably enhanced by the MoS_2 passivation layer likely due to an added electron passage, while no significant change was observed in hole transport. This effect became insignificant as the thickness of BP increases so that the I_{ds}-V_g curves from the MoS_2-passivated and exposed areas of the 20 nm device barely deviated from each other. Under illumination of λ = 600 nm, photoconductivity was increased by 78 % in the 2L device (V_g = 0 V) in the MoS_2-passivated region than the BP-only. In addition, a noticeable photo-induced doping effect was observed, which became less significant in the thicker BP devices. Hence, these results demonstrated that the BP-MoS_2 vdW heterostructures could add another strategic route towards air-protected BP-based nanoelectronics with boosted photoconductivity, and introducing different combinations of 2D materials will open up various opportunities allowing for sophisticated engineering of the band alignment for specific target applications.

6. Summary and Future Work

6.1 Thesis Summary

In this thesis, electronic and optoelectronic properties of 2D materials (MoS_2, WSe_2, BP, and graphene) were studied in the context of their layer number dependence, behaviors at the vdW heterointerfaces and the junctions with metals. We started with a brief introduction to 2 D materials in general and their potential as an active material in a wide variety of (opto)electronic device applications. Because of their ever decreasing size dimension down to the nanoscale, many different types of interfaces inevitable in 2D electronic devices—for instance, p-n or Schottky junctions between 2D crystals and metals or dissimilar 2D crystals—play more critical role in determining device performance. Thus, we have conducted thorough investigation into these interfaces by utilizing the PCS-AFM setup as well as fabricating FET devices based on vdW heterointerfaces.

This thesis started off with exploring the layer number dependent electrical characteristics of the MoS_2–metal nanoscale junction using current imaging of MoS_2 nanosheets consisting of regions of varying different thicknesses using the PCS-AFM. The layer number dependence of the effective barrier was measured to be linear by obtaining consecutive current images while changing bias voltages. Then, the layer number dependent spectral photoconductivity of MoS_2 is investigated: the highest response was observed in single layer (1L) region; the photoconductivity decreased with layer number, but increased again between 4L and 10L mainly due to increased light absorption. The photoconductivity also showed strong dependence on the wavelength of the incident light, showing much higher photoenhancement for photon energies beyond the optical bandgap. The photoresponse showed barrier symmetry for 1L but conspicuous asymmetry for 2, 3, and 4L in forward and reverse biases, corroborating a dominant role of the energy barrier on carrier transport at the nanoscale junction.

Then the second part of this thesis studied the spatially resolved transverse electrical properties of the monolayer WSe_2-MoS_2 in-plane p-n heterostructures using the PCS-AFM both in the dark and under laser illumination. Similar to the first part of the thesis, spatial

dependence of electronic and optoelectronic characteristics of the heterostructure sample were conveniently and accurately interrogated under the same experimental conditions without the complexities associated with fabricating and testing of different individual field-effect transistor devices. By performing current imaging using a PtIr-coated conductive tip on an ultrathin flake that includes homogeneous crystals of WSe_2 and MoS_2, and a lateral junction region in between, thousands of nanoscale WSe_2/MoS_2/the junction–metal junctions were made during imaging and direct comparisons between their local properties were made at the same time under identical experimental conditions with the nanoscale spatial resolution.

Finally, new types of 2D vertical heterostructures that simultaneously possess desirable properties of constituent materials were developed, which suggest viable paths for overcoming intrinsic demerits of individual 2D materials from the perspecrtive of the 2D nanoelectronics. Firstly, a MoS_2-graphene vertical heterostructure was fabricated and charge transfer and photoluminescence (PL) at the vdW heterointerface were studied. C-AFM and Raman spectroscopy revealed a significant charge transfer at the vdW junction. The PL intensity of monolayer MoS_2 was significantly quenched after making junctions with a single layered graphene. Then, a black phosphorus (BP)-MoS_2 vertical vdW heterostructure was tested as an ultrathin channel structure in 2D (opto)electronic devices. Optical microscopy, AFM images, and Raman spectroscopy data showed that the MoS_2 thin films can be used as an encapsulation layer, preserving BP crystals from deteriorating in air as well as under an high temperature. The electrical characteristics of FET devices based on the heterostuctures exhibited that the MoS_2 layer has limited influence on carrier transport properties of the BP channel. Under light illumination, higher photoconductivity was observed in the BP-MoS_2 heterostructure region than that of the homogeneous BP region, owing to the built-in electric field at the heterointerface that enhanced the separation of the electron-hole pairs generated by light absorption.

6.2 Future Research Directions

Although many different 2D materials have been interrogated extensively from all sorts of different perspectives, more efficient characterization techniques are required to keep up with the pace with which new 2D materials are discovered; and local characterizations in the nanometer scale have remained challenging. Also, in order to exploit the quantum confinement effect to the fullest in electronic devices developments, accurate measurements capable of capturing subtle differences in electronic properties of 2D materials are required. Throughout this thesis we have heavily used the PCS-AFM which efficiently generated simultaneous current and photocurrent images, since the instrument has many advantages over conventional transistors to study unique features of different 2D materials.

Therefore, addition of more capabilities to the instrument will enable more comprehensive characterization of important properties of pre-assembled devices and candidate materials, which will facilitate understanding and further engineering of new 2D materials. To this end, our ongoing efforts are dedicated to fluorescence imaging and optical excitation profile capabilities. A spectrometer and a single photon detector are being aligned to the emission detection side and a tunable laser filter is being aligned to the excitation side in addition to the current instrumental setup. Once this upgrade is completed the instrument will become a much more powerful tool to interrogate 2D materials that efficiently generate spatially resolved images of morphology, mechanical lateral force, dark current, photocurrent as well as fluorescence and optical excitation profiles in the ranges of from visible to near IR. Once this work is fully functional further steps can be taken to add additional capabilities for carrier lifetime imaging. This would require the alignment of a single photon detector and time-correlated photon counting electronics to detect measure transient fluorescence decays. If successful, tracking of excited state dynamics along with the measurements of other nanoscale physical properties of 2D materials will be possible. The excited state dynamics will be a powerful data set in correlating electrical and optical properties of a material with mechanical and morphological insight gained simultaneously.

7. References

1. Novoselov, K. S.; Geim, A. K.; Morozov, S. V.; Jiang, D.; Zhang, Y.; Dubonos, S. V.; Grigorieva, I. V.; Firsov, A. A. Electric Field Effect in Atomically Thin Carbon Films. *Science* 2004, 306, 666-669.
2. Bhimanapati, G. R.; Lin, Z.; Meunier, V.; Jung, Y.; Cha, J.; Das, S.; Xiao, D.; Son, Y.; Strano, M. S.; Cooper, V. R.; Liang, L.; Louie, S. G.; Ringe, E.; Zhou, W.; Kim, S. S.; Naik, R. R.; Sumpter, B. G.; Terrones, H.; Xia, F.; Wang, Y.; Zhu, J.; Akinwande, D.; Alem, N.; Schuller, J. A.; Schaak, R. E.; Terrones, M.; Robinson, J. A. Recent Advances in Two-Dimensional Materials Beyond Graphene. *ACS Nano* 2015, 9, 11509-11539.
3. Wang, Q. H.; Kalantar-Zadeh, K.; Kis, A.; Coleman, J. N.; Strano, M. S. Electronics and Optoelectronics of Two-Dimensional Transition Metal Dichalcogenides. *Nat. Nanotechnol.* 2012, 7, 699-712.
4. RadisavljevicB; RadenovicA; BrivioJ; GiacomettiV; KisA. Single-Layer Mos2 Transistors. *Nat. Nanotechnol.* 2011, 6, 147-150.
5. Kuc, A.; Zibouche, N.; Heine, T. Influence of Quantum Confinement on the Electronic Structure of the Transition Metal Sulfide TS${}_{2}$. *Phys. Rev. B* 2011, 83, 245213.
6. Splendiani, A.; Sun, L.; Zhang, Y.; Li, T.; Kim, J.; Chim, C.-Y.; Galli, G.; Wang, F. Emerging Photoluminescence in Monolayer Mos2. *Nano. Lett.* 2010, 10, 1271-1275.
7. Mak, K. F.; Lee, C.; Hone, J.; Shan, J.; Heinz, T. F. Atomically Thin ${\Mathrm{Mos}}_{2}$: A New Direct-Gap Semiconductor. *Phys. Rev. Lett.* 2010, 105, 136805.
8. Novoselov, K. S.; Geim, A. K.; Morozov, S. V.; Jiang, D.; Katsnelson, M. I.; Grigorieva, I. V.; Dubonos, S. V.; Firsov, A. A. Two-Dimensional Gas of Massless Dirac Fermions in Graphene. *Nature* 2005, 438, 197-200.
9. Geim, A. K.; Novoselov, K. S. The Rise of Graphene. *Nat. Mater.* 2007, 6, 183-191.
10. Mas-Balleste, R.; Gomez-Navarro, C.; Gomez-Herrero, J.; Zamora, F. 2d Materials: To Graphene and Beyond. *Nanoscale* 2011, 3, 20-30.
11. Ando, T. The Electronic Properties of Graphene and Carbon Nanotubes. *NPG Asia Mater* 2009, 1, 17-21.
12. Bolotin, K. I.; Sikes, K. J.; Jiang, Z.; Klima, M.; Fudenberg, G.; Hone, J.; Kim, P.; Stormer, H. L. Ultrahigh Electron Mobility in Suspended Graphene. *Solid State Comm.* 2008, 146, 351-355.
13. Bridgman, P. W. Two New Modifications of Phosphorus. *J. Amer. Chem. Soc.* 1914, 36, 1344-1363.
14. Ling, X.; Wang, H.; Huang, S.; Xia, F.; Dresselhaus, M. S. The Renaissance of Black Phosphorus. *Proc. Nat. Acad. Sci.* 2015, 112, 4523-4530.
15. Cai, Y.; Zhang, G.; Zhang, Y.-W. Layer-Dependent Band Alignment and Work Function of Few-Layer Phosphorene. *Scientific Reports* 2014, 4, 6677.
16. Li, Y.; Yang, S.; Li, J. Modulation of the Electronic Properties of Ultrathin Black Phosphorus by Strain and Electrical Field. *J. Phys. Chem. C* 2014, 118, 23970-23976.
17. Li, L.; Yu, Y.; Ye, G. J.; Ge, Q.; Ou, X.; Wu, H.; Feng, D.; Chen, X. H.; Zhang, Y. Black Phosphorus Field-Effect Transistors. *Nat. Nanotechnol.* 2014, 9, 372-377.
18. Kim, J. S.; Jeon, P. J.; Lee, J.; Choi, K.; Lee, H. S.; Cho, Y.; Lee, Y. T.; Hwang, D. K.; Im, S. Dual Gate Black Phosphorus Field Effect Transistors on Glass for nor Logic and Organic Light Emitting Diode Switching. *Nano. Lett.* 2015, 15, 5778-5783.
19. Liu, H.; Neal, A. T.; Zhu, Z.; Luo, Z.; Xu, X.; Tománek, D.; Ye, P. D. Phosphorene: An Unexplored 2d Semiconductor with a High Hole Mobility. *ACS Nano* 2014, 8, 4033-4041.
20. Koenig, S. P.; Doganov, R. A.; Schmidt, H.; Castro Neto, A. H.; Özyilmaz, B. Electric Field Effect in Ultrathin Black Phosphorus. *Appl. Phys. Lett.* 2014, 104, 103106.

21. Xia, F.; Wang, H.; Jia, Y. Rediscovering Black Phosphorus as an Anisotropic Layered Material for Optoelectronics and Electronics. *Nat Commun* 2014, 5.
22. Qiao, J.; Kong, X.; Hu, Z.-X.; Yang, F.; Ji, W. High-Mobility Transport Anisotropy and Linear Dichroism in Few-Layer Black Phosphorus. *Nat Commun* 2014, 5.
23. Andres, C.-G.; Leonardo, V.; Elsa, P.; Joshua, O. I.; Narasimha-Acharya, K. L.; Sofya, I. B.; Dirk, J. G.; Michele, B.; Gary, A. S.; Alvarez, J. V.; Henny, W. Z.; Palacios, J. J.; Herre, S. J. v. d. Z. Isolation and Characterization of Few-Layer Black Phosphorus. *2D Materials* 2014, 1, 025001.
24. Wood, J. D.; Wells, S. A.; Jariwala, D.; Chen, K.-S.; Cho, E.; Sangwan, V. K.; Liu, X.; Lauhon, L. J.; Marks, T. J.; Hersam, M. C. Effective Passivation of Exfoliated Black Phosphorus Transistors against Ambient Degradation. *Nano. Lett.* 2014, 14, 6964-6970.
25. Yi, M.; Shen, Z. A Review on Mechanical Exfoliation for the Scalable Production of Graphene. *Journal of Materials Chemistry A* 2015, 3, 11700-11715.
26. Li, X.; Cai, W.; An, J.; Kim, S.; Nah, J.; Yang, D.; Piner, R.; Velamakanni, A.; Jung, I.; Tutuc, E.; Banerjee, S. K.; Colombo, L.; Ruoff, R. S. Large-Area Synthesis of High-Quality and Uniform Graphene Films on Copper Foils. *Science* 2009, 324, 1312-1314.
27. Reina, A.; Jia, X.; Ho, J.; Nezich, D.; Son, H.; Bulovic, V.; Dresselhaus, M. S.; Kong, J. Large Area, Few-Layer Graphene Films on Arbitrary Substrates by Chemical Vapor Deposition. *Nano. Lett.* 2009, 9, 30-35.
28. Yu, Y.; Li, C.; Liu, Y.; Su, L.; Zhang, Y.; Cao, L. Controlled Scalable Synthesis of Uniform, High-Quality Monolayer and Few-Layer Mos2 Films. *Scientific Reports* 2013, 3, 1866.
29. Mattheiss, L. F. Energy Bands for 2h-Nbse2 and 2h-Mos2. *Phys. Rev. Lett.* 1973, 30, 784-787.
30. Mak, K. F.; He, K.; Shan, J.; Heinz, T. F. Control of Valley Polarization in Monolayer Mos2 by Optical Helicity. *Nat. Nanotechnol.* 2012, 7, 494-498.
31. Zeng, H.; Dai, J.; Yao, W.; Xiao, D.; Cui, X. Valley Polarization in Mos2 Monolayers by Optical Pumping. *Nat. Nanotechnol.* 2012, 7, 490-493.
32. Mak, K. F.; He, K.; Lee, C.; Lee, G. H.; Hone, J.; Heinz, T. F.; Shan, J. Tightly Bound Trions in Monolayer Mos2. *Nat. Mater.* 2013, 12, 207-211.
33. Wu, S.; Ross, J. S.; Liu, G.-B.; Aivazian, G.; Jones, A.; Fei, Z.; Zhu, W.; Xiao, D.; Yao, W.; Cobden, D.; Xu, X. Electrical Tuning of Valley Magnetic Moment through Symmetry Control in Bilayer Mos2. *Nat. Phys.* 2013, 9, 149-153.
34. Kim, S.; Konar, A.; Hwang, W.-S.; Lee, J. H.; Lee, J.; Yang, J.; Jung, C.; Kim, H.; Yoo, J.-B.; Choi, J.-Y.; Jin, Y. W.; Lee, S. Y.; Jena, D.; Choi, W.; Kim, K. High-Mobility and Low-Power Thin-Film Transistors Based on Multilayer Mos2 Crystals. *Nat Commun* 2012, 3, 1011.
35. Choi, W.; Cho, M. Y.; Konar, A.; Lee, J. H.; Cha, G.-B.; Hong, S. C.; Kim, S.; Kim, J.; Jena, D.; Joo, J.; Kim, S. High-Detectivity Multilayer Mos2 Phototransistors with Spectral Response from Ultraviolet to Infrared. *Adv. Mater.* 2012, 24, 5832-5836.
36. Radisavljevic, B.; Whitwick, M. B.; Kis, A. Integrated Circuits and Logic Operations Based on Single-Layer Mos2. *ACS Nano* 2011, 5, 9934-9938.
37. Wang, H.; Yu, L.; Lee, Y.-H.; Shi, Y.; Hsu, A.; Chin, M. L.; Li, L.-J.; Dubey, M.; Kong, J.; Palacios, T. Integrated Circuits Based on Bilayer Mos2 Transistors. *Nano. Lett.* 2012, 12, 4674-4680.
38. Lee, H. S.; Min, S.-W.; Chang, Y.-G.; Park, M. K.; Nam, T.; Kim, H.; Kim, J. H.; Ryu, S.; Im, S. Mos2 Nanosheet Phototransistors with Thickness-Modulated Optical Energy Gap. *Nano. Lett.* 2012, 12, 3695-3700.
39. Lopez-Sanchez, O.; Lembke, D.; Kayci, M.; Radenovic, A.; Kis, A. Ultrasensitive Photodetectors Based on Monolayer Mos2. *Nat. Nanotechnol.* 2013, 8, 497-501.
40. Yin, Z.; Li, H.; Li, H.; Jiang, L.; Shi, Y.; Sun, Y.; Lu, G.; Zhang, Q.; Chen, X.; Zhang, H. Single-Layer Mos2 Phototransistors. *ACS Nano* 2011, 6, 74-80.
41. Sundaram, R. S.; Engel, M.; Lombardo, A.; Krupke, R.; Ferrari, A. C.; Avouris, P.; Steiner, M. Electroluminescence in Single Layer Mos2. *Nano. Lett.* 2013, 13, 1416-1421.
42. Cheiwchanchamnangij, T.; Lambrecht, W. R. L. Quasiparticle Band Structure Calculation of Monolayer, Bilayer, and Bulk Mos2. *Phys. Rev. B* 2012, 85, 205302.

43. Kuc, A.; Zibouche, N.; Heine, T. Influence of Quantum Confinement on the Electronic Structure of the Transition Metal Sulfide Ts2. *Phys. Rev. B* 2011, 83, 245213.
44. Mak, K. F.; Lee, C.; Hone, J.; Shan, J.; Heinz, T. F. Atomically Thin Mos2: A New Direct-Gap Semiconductor. *Phys. Rev. Lett.* 2010, 105, 136805.
45. Ayari, A.; Cobas, E.; Ogundadegbe, O.; Fuhrer, M. S. Realization and Electrical Characterization of Ultrathin Crystals of Layered Transition-Metal Dichalcogenides. *J. Appl. Phys.* 2007, 101, 014507.
46. Yoon, Y.; Ganapathi, K.; Salahuddin, S. How Good Can Monolayer Mos2 Transistors Be? *Nano Letters* 2011, 11, 3768-3773.
47. Li, H.; Yin, Z. Y.; He, Q. Y.; Li, H.; Huang, X.; Lu, G.; Fam, D. W. H.; Tok, A. I. Y.; Zhang, Q.; Zhang, H. Fabrication of Single- and Multilayer Mos2 Film-Based Field-Effect Transistors for Sensing No at Room Temperature. *Small* 2012, 8, 63-67.
48. Lee, K.; Kim, H. Y.; Lotya, M.; Coleman, J. N.; Kim, G. T.; Duesberg, G. S. Electrical Characteristics of Molybdenum Disulfide Flakes Produced by Liquid Exfoliation. *Advanced Materials* 2011, 23, 4178-4181.
49. Das, S.; Chen, H.-Y.; Penumatcha, A. V.; Appenzeller, J. High Performance Multilayer Mos2 Transistors with Scandium Contacts. *Nano Letters* 2012, 13, 100-105.
50. Liu, H.; Ye, P. D. Mos2 Dual-Gate Mosfet with Atomic-Layer-Deposited Al2o3 as Top-Gate Dielectric. *Electron Device Letters, IEEE* 2012, 33, 546-548.
51. Qiu, H.; Pan, L.; Yao, Z.; Li, J.; Shi, Y.; Wang, X. Electrical Characterization of Back-Gated Bi-Layer Mos2 Field-Effect Transistors and the Effect of Ambient on Their Performances. *Appl. Phys. Lett.* 2012, 100, 123104.
52. Liu, H.; Neal, A. T.; Ye, P. D. Channel Length Scaling of Mos2 Mosfets. *Acs Nano* 2012, 6, 8563-8569.
53. Jariwala, D.; Sangwan, V. K.; Late, D. J.; Johns, J. E.; Dravid, V. P.; Marks, T. J.; Lauhon, L. J.; Hersam, M. C. Band-Like Transport in High Mobility Unencapsulated Single-Layer Mos2 Transistors. *Appl. Phys. Lett.* 2013, 102, 173107.
54. Shih, C.-J.; Wang, Q. H.; Son, Y.; Jin, Z.; Blankschtein, D.; Strano, M. S. Tuning on–Off Current Ratio and Field-Effect Mobility in a Mos2–Graphene Heterostructure Via Schottky Barrier Modulation. *Acs Nano* 2014.
55. Late, D. J.; Liu, B.; Matte, H. S. S. R.; Dravid, V. P.; Rao, C. N. R. Hysteresis in Single-Layer Mos2 Field Effect Transistors. *Acs Nano* 2012, 6, 5635-5641.
56. Walia, S.; Balendhran, S.; Wang, Y.; Ab Kadir, R.; Sabirin Zoolfakar, A.; Atkin, P.; Zhen Ou, J.; Sriram, S.; Kalantar-zadeh, K.; Bhaskaran, M. Characterization of Metal Contacts for Two-Dimensional Mos2 Nanoflakes. *Appl. Phys. Lett.* 2013, 103, 232105

57. Li, Y.; Xu, C.-Y.; Zhen, L. Surface Potential and Interlayer Screening Effects of Few-Layer Mos2 Nanoflakes. *Appl. Phys. Lett.* 2013, 102, 143110.
58. Wu, C.-C.; Jariwala, D.; Sangwan, V. K.; Marks, T. J.; Hersam, M. C.; Lauhon, L. J. Elucidating the Photoresponse of Ultrathin Mos2 Field-Effect Transistors by Scanning Photocurrent Microscopy. *The Journal of Physical Chemistry Letters* 2013, 4, 2508-2513.
59. Novoselov, K. S.; Jiang, D.; Schedin, F.; Booth, T. J.; Khotkevich, V. V.; Morozov, S. V.; Geim, A. K. Two-Dimensional Atomic Crystals. *Proc. Natl. Acad. Sci. U.S.A.* 2005, 102, 10451-10453.
60. Lee, C.; Yan, H.; Brus, L. E.; Heinz, T. F.; Hone, J.; Ryu, S. Anomalous Lattice Vibrations of Single- and Few-Layer Mos2. *ACS Nano* 2010, 4, 2695-2700.
61. Nečas, D.; Klapetek, P. Gwyddion: An Open-Source Software for Spm Data Analysis. *Centr. Eur. J. Phys.* 2012, 10, 181-188.
62. Cappella, B.; Dietler, G. Force-Distance Curves by Atomic Force Microscopy. *Surf. Sci. Rep.* 1999, 34, 1-104.

63. Frammelsberger, W.; Benstetter, G.; Kiely, J.; Stamp, R. C-Afm-Based Thickness Determination of Thin and Ultra-Thin Sio2 Films by Use of Different Conductive-Coated Probe Tips. *Appl. Surf. Sci.* 2007, 253, 3615-3626.
64. Ruskell, T. G.; Workman, R. K.; Chen, D.; Sarid, D.; Dahl, S.; Gilbert, S. High Resolution Fowler-Nordheim Field Emission Maps of Thin Silicon Oxide Layers. *Appl. Phys. Lett.* 1996, 68, 93.
65. Teichert, C.; Beinik, I. Conductive Atomic-Force Microscopy Investigation of Nanostructures in Microelectronics. In *Scanning Probe Microscopy in Nanoscience and Nanotechnology 2*, Bhushan, B., Ed. Springer Berlin Heidelberg: 2011; pp 691-721.
66. Brandes, E. A.; Brook, G. B. Smithells Metals Reference Book (7th Edition). Elsevier.
67. Castellanos-Gomez, A.; Poot, M.; Steele, G. A.; van der Zant, H. S. J.; Agraït, N.; Rubio-Bollinger, G. Elastic Properties of Freely Suspended Mos2 Nanosheets. *Adv. Mater.* 2012, 24, 772-775.
68. Lovell, M. R.; Khonsari, M. M.; Marangoni, R. D. A Finite Element Analysis of the Frictional Forces between a Cylindrical Bearing Element and Mos2 Coated and Uncoated Surfaces. *Wear* 1996, 194, 60-70.
69. Deb, P.; Kim, H.; Qin, Y.; Lahiji, R.; Oliver, M.; Reifenberger, R.; Sands, T. Gan Nanorod Schottky and P−N Junction Diodes. *Nano. Lett.* 2006, 6, 2893-2898.
70. Xu, D.; Watt, G. D.; Harb, J. N.; Davis, R. C. Electrical Conductivity of Ferritin Proteins by Conductive Afm. *Nano. Lett.* 2005, 5, 571-577.
71. Andolfi, L.; Cannistraro, S. Conductive Atomic Force Microscopy Study of Plastocyanin Molecules Adsorbed on Gold Electrode. *Surf. Sci.* 2005, 598, 68-77.
72. Baldacchini, C.; Cannistraro, S. Conductive Atomic Force Microscopy Investigation of Transverse Current across Metallic and Semiconducting Single-Walled Carbon Nanotubes. *Appl. Phys. Lett.* 2007, 91, 122103.
73. Kivioja, J. M.; Kurppa, K.; Kainlauri, M.; Linder, M. B.; Ahopelto, J. Electrical Transport through Ordered Self-Assembled Protein Monolayer Measured by Constant Force Conductive Atomic Force Microscopy. *Appl. Phys. Lett.* 2009, 94, 183901.
74. Moore, J. C.; Kenny, S. M.; Baird, C. S.; Morkoç, H.; Baski, A. A. Electronic Behavior of the Zn- and O-Polar Zno Surfaces Studied Using Conductive Atomic Force Microscopy. *J. Appl. Phys.* 2009, 105, 116102.
75. Klaua, M.; Ullmann, D.; Barthel, J.; Wulfhekel, W.; Kirschner, J.; Urban, R.; Monchesky, T. L.; Enders, A.; Cochran, J. F.; Heinrich, B. Growth, Structure, Electronic, and Magnetic Properties of Mgo/Fe(001) Bilayers and Fe/Mgo/Fe(001) Trilayers. *Phys. Rev. B* 2001, 64, 134411.
76. Abrams, B. L.; Wilcoxon, J. P. Nanosize Semiconductors for Photooxidation. *Crit. Rev. Solid State Mater. Sci.* 2005, 30, 153-182.
77. Han, S. W.; Kwon, H.; Kim, S. K.; Ryu, S.; Yun, W. S.; Kim, D. H.; Hwang, J. H.; Kang, J. S.; Baik, J.; Shin, H. J.; Hong, S. C. Band-Gap Transition Induced by Interlayer Van Der Waals Interaction in Mos2. *Physical Review B* 2011, 84, 045409.
78. Rhoderick, E. H. Metal-Semiconductor Contacts. *Solid-State and Electron Devices, IEE Proceedings I* 1982, 129, 1.
79. Fowler, R. H.; Nordheim, L. Electron Emission in Intense Electric Fields. *Proc. Roy. Soc. Lond. A* 1928, 119, 173-181.
80. Gong, C.; Colombo, L.; Wallace, R. M.; Cho, K. The Unusual Mechanism of Partial Fermi Level Pinning at Metal–Mos2 Interfaces. *Nano. Lett.* 2014, 14, 1714-1720.
81. Sze, S. M.; Ng, K. K. *Physics of Semiconductor Devices*. 3rd ed.; Wiley-Interscience: Hoboken, N.J., 2007; p x, 815 p.
82. Smit, G. D. J.; Rogge, S.; Klapwijk, T. M. Scaling of Nano-Schottky-Diodes. *Appl. Phys. Lett.* 2002, 81, 3852.
83. Smit, G. D. J.; Rogge, S.; Klapwijk, T. M. Enhanced Tunneling across Nanometer-Scale Metal–Semiconductor Interfaces. *Appl. Phys. Lett.* 2002, 80, 2568.
84. Zhang, W.; Huang, J.-K.; Chen, C.-H.; Chang, Y.-H.; Cheng, Y.-J.; Li, L.-J. High-Gain Phototransistors Based on a Cvd Mos2 Monolayer. *Adv. Mater.* 2013, 25, 3456-3461.

85. Tsai, D.-S.; Liu, K.-K.; Lien, D.-H.; Tsai, M.-L.; Kang, C.-F.; Lin, C.-A.; Li, L.-J.; He, J.-H. Few-Layer Mos2 with High Broadband Photogain and Fast Optical Switching for Use in Harsh Environments. *Acs Nano* 2013, 7, 3905-3911.
86. Sun, D.; Rao, Y.; Reider, G. A.; Chen, G.; You, Y.; Brézin, L.; Harutyunyan, A. R.; Heinz, T. F. Observation of Rapid Exciton–Exciton Annihilation in Monolayer Molybdenum Disulfide. *Nano. Lett.* 2014, 14, 5625-5629.
87. Cui, Y.; Xin, R.; Yu, Z.; Pan, Y.; Ong, Z.-Y.; Wei, X.; Wang, J.; Nan, H.; Ni, Z.; Wu, Y.; Chen, T.; Shi, Y.; Wang, B.; Zhang, G.; Zhang, Y.-W.; Wang, X. High-Performance Monolayer Ws2 Field-Effect Transistors on High-K Dielectrics. *Adv. Mater.* 2015, 27, 5230-5234.
88. Larentis, S.; Fallahazad, B.; Tutuc, E. Field-Effect Transistors and Intrinsic Mobility in Ultra-Thin Mose2 Layers. *Appl. Phys. Lett.* 2012, 101, 223104.
89. Tosun, M.; Chuang, S.; Fang, H.; Sachid, A. B.; Hettick, M.; Lin, Y.; Zeng, Y.; Javey, A. High-Gain Inverters Based on Wse2 Complementary Field-Effect Transistors. *ACS Nano* 2014, 8, 4948-4953.
90. Abderrahmane, A.; Ko, P. J.; Thu, T. V.; Ishizawa, S.; Takamura, T.; Sandhu, A. High Photosensitivity Few-Layered Mose2 Back-Gated Field-Effect Phototransistors. *Nanotechnol.* 2014, 25, 365202.
91. Zhang, W.; Chiu, M.-H.; Chen, C.-H.; Chen, W.; Li, L.-J.; Wee, A. T. S. Role of Metal Contacts in High-Performance Phototransistors Based on Wse2 Monolayers. *ACS Nano* 2014, 8, 8653-8661.
92. Cakr, D.; Sevik, C.; Peeters, F. M. Engineering Electronic Properties of Metal-Mose2 Interfaces Using Self-Assembled Monolayers. *Journal of Materials Chemistry C* 2014, 2, 9842-9849.
93. Das, S.; Chen, H.-Y.; Penumatcha, A. V.; Appenzeller, J. High Performance Multilayer Mos2 Transistors with Scandium Contacts. *Nano. Lett.* 2013, 13, 100-105.
94. Walia, S.; Balendhran, S.; Wang, Y.; Ab Kadir, R.; Sabirin Zoolfakar, A.; Atkin, P.; Zhen Ou, J.; Sriram, S.; Kalantar-zadeh, K.; Bhaskaran, M. Characterization of Metal Contacts for Two-Dimensional Mos2 Nanoflakes. *Appl. Phys. Lett.* 2013, 103, 232105.
95. Sata, Y.; Moriya, R.; Morikawa, S.; Yabuki, N.; Masubuchi, S.; Machida, T. Electric Field Modulation of Schottky Barrier Height in Graphene/Mose2 Van Der Waals Heterointerface. *Appl. Phys. Lett.* 2015, 107, 023109.
96. Shih, C.-J.; Wang, Q. H.; Son, Y.; Jin, Z.; Blankschtein, D.; Strano, M. S. Tuning on–Off Current Ratio and Field-Effect Mobility in a Mos2–Graphene Heterostructure Via Schottky Barrier Modulation. *ACS Nano* 2014, 8, 5790-5798.
97. Tian, H.; Tan, Z.; Wu, C.; Wang, X.; Mohammad, M. A.; Xie, D.; Yang, Y.; Wang, J.; Li, L.-J.; Xu, J.; Ren, T.-L. Novel Field-Effect Schottky Barrier Transistors Based on Graphene-Mos2 Heterojunctions. *Scientific Reports* 2014, 4, 5951.
98. Ross, J. S.; Klement, P.; Jones, A. M.; Ghimire, N. J.; Yan, J.; Mandrus, D. G.; Taniguchi, T.; Watanabe, K.; Kitamura, K.; Yao, W.; Cobden, D. H.; Xu, X. Electrically Tunable Excitonic Light-Emitting Diodes Based on Monolayer Wse2 P-N Junctions. *Nat. Nanotechnol.* 2014, 9, 268-272.
99. Huang, L.; Huo, N.; Li, Y.; Chen, H.; Yang, J.; Wei, Z.; Li, J.; Li, S.-S. Electric-Field Tunable Band Offsets in Black Phosphorus and Mos2 Van Der Waals P-N Heterostructure. *The Journal of Physical Chemistry Letters* 2015, 6, 2483-2488.
100. Zhang, Y. J.; Ye, J. T.; Yomogida, Y.; Takenobu, T.; Iwasa, Y. Formation of a Stable P–N Junction in a Liquid-Gated Mos2 Ambipolar Transistor. *Nano. Lett.* 2013, 13, 3023-3028.
101. Lee, C.-H.; Lee, G.-H.; van der Zande, A. M.; Chen, W.; Li, Y.; Han, M.; Cui, X.; Arefe, G.; Nuckolls, C.; Heinz, T. F.; Guo, J.; Hone, J.; Kim, P. Atomically Thin P–N Junctions with Van Der Waals Heterointerfaces. *Nat. Nanotechnol.* 2014, 9, 676-681.
102. Deng, Y.; Luo, Z.; Conrad, N. J.; Liu, H.; Gong, Y.; Najmaei, S.; Ajayan, P. M.; Lou, J.; Xu, X.; Ye, P. D. Black Phosphorus–Monolayer Mos2 Van Der Waals Heterojunction P–N Diode. *ACS Nano* 2014, 8, 8292-8299.
103. Li, M.-Y.; Shi, Y.; Cheng, C.-C.; Lu, L.-S.; Lin, Y.-C.; Tang, H.-L.; Tsai, M.-L.; Chu, C.-W.; Wei, K.-H.; He, J.-H.; Chang, W.-H.; Suenaga, K.; Li, L.-J. Epitaxial Growth of a Monolayer Wse2-Mos2 Lateral P-N Junction with an Atomically Sharp Interface. *Science* 2015, 349, 524-528.

104. Son, Y.; Wang, Q. H.; Paulson, J. A.; Shih, C.-J.; Rajan, A. G.; Tvrdy, K.; Kim, S.; Alfeeli, B.; Braatz, R. D.; Strano, M. S. Layer Number Dependence of Mos2 Photoconductivity Using Photocurrent Spectral Atomic Force Microscopic Imaging. *ACS Nano* 2015, 9, 2843-2855.
105. Chiu, M.-H.; Zhang, C.; Shiu, H.-W.; Chuu, C.-P.; Chen, C.-H.; Chang, C.-Y. S.; Chen, C.-H.; Chou, M.-Y.; Shih, C.-K.; Li, L.-J. Determination of Band Alignment in the Single-Layer Mos2/Wse2 Heterojunction. *Nat Commun* 2015, 6.
106. Huang, J.-K.; Pu, J.; Hsu, C.-L.; Chiu, M.-H.; Juang, Z.-Y.; Chang, Y.-H.; Chang, W.-H.; Iwasa, Y.; Takenobu, T.; Li, L.-J. Large-Area Synthesis of Highly Crystalline Wse2 Monolayers and Device Applications. *ACS Nano* 2014, 8, 923-930.
107. Inyeal, L.; Servin, R.; Lijun, L.; Dongsuk, L.; Muhammad Atif, K.; Kannan, E. S.; Gil-Ho, K. Non-Degenerate N-Type Doping by Hydrazine Treatment in Metal Work Function Engineered Wse 2 Field-Effect Transistor. *Nanotechnol.* 2015, 26, 455203.
108. Gong, C.; Zhang, H.; Wang, W.; Colombo, L.; Wallace, R. M.; Cho, K. Band Alignment of Two-Dimensional Transition Metal Dichalcogenides: Application in Tunnel Field Effect Transistors. *Appl. Phys. Lett.* 2013, 103, 053513.
109. Rezk, A. R.; Carey, B.; Chrimes, A. F.; Lau, D. W. M.; Gibson, B. C.; Zheng, C.; Fuhrer, M. S.; Yeo, L. Y.; Kalantar-zadeh, K. Acoustically-Driven Trion and Exciton Modulation in Piezoelectric Two-Dimensional Mos2. *Nano. Lett.* 2016, 16, 849-855.
110. Miller, B.; Parzinger, E.; Vernickel, A.; Holleitner, A. W.; Wurstbauer, U. Photogating of Mono- and Few-Layer Mos2. *Appl. Phys. Lett.* 2015, 106, 122103.
111. Liu, H.-L.; Shen, C.-C.; Su, S.-H.; Hsu, C.-L.; Li, M.-Y.; Li, L.-J. Optical Properties of Monolayer Transition Metal Dichalcogenides Probed by Spectroscopic Ellipsometry. *Appl. Phys. Lett.* 2014, 105, 201905.
112. Flöry, N.; Jain, A.; Bharadwaj, P.; Parzefall, M.; Taniguchi, T.; Watanabe, K.; Novotny, L. A Wse2/Mose2 Heterostructure Photovoltaic Device. *Appl. Phys. Lett.* 2015, 107, 123106.
113. Ramasubramaniam, A. Large Excitonic Effects in Monolayers of Molybdenum and Tungsten Dichalcogenides. *Phys. Rev. B* 2012, 86, 115409.
114. Wang, Q. H.; Kalantar-Zadeh, K.; Kis, A.; Coleman, J. N.; Strano, M. S. Electronics and Optoelectronics of Two-Dimensional Transition Metal Dichalcogenides. *Nature Nanotechnology* 2012, 7, 699-712.
115. Wang, H.; Yu, L. L.; Lee, Y. H.; Shi, Y. M.; Hsu, A.; Chin, M. L.; Li, L. J.; Dubey, M.; Kong, J.; Palacios, T. Integrated Circuits Based on Bilayer Mos2 Transistors. *Nano Letters* 2012, 12, 4674-4680.
116. Dimitrakopoulos, C. D.; Mascaro, D. J. Organic Thin-Film Transistors: A Review of Recent Advances. *Ibm Journal of Research and Development* 2001, 45, 11-27.
117. Chen, J. H.; Jang, C.; Xiao, S. D.; Ishigami, M.; Fuhrer, M. S. Intrinsic and Extrinsic Performance Limits of Graphene Devices on Sio2. *Nature Nanotechnology* 2008, 3, 206-209.
118. Dean, C. R.; Young, A. F.; Meric, I.; Lee, C.; Wang, L.; Sorgenfrei, S.; Watanabe, K.; Taniguchi, T.; Kim, P.; Shepard, K. L.; Hone, J. Boron Nitride Substrates for High-Quality Graphene Electronics. *Nature Nanotechnology* 2010, 5, 722-726.
119. Ayari, A.; Cobas, E.; Ogundadegbe, O.; Fuhrer, M. S. Realization and Electrical Characterization of Ultrathin Crystals of Layered Transition-Metal Dichalcogenides. *Journal of Applied Physics* 2007, 101, 014507.
120. Radisavljevic, B.; Radenovic, A.; Brivio, J.; Giacometti, V.; Kis, A. Single-Layer Mos2 Transistors. *Nature Nanotechnology* 2011, 6, 147-150.
121. Kim, S.; Konar, A.; Hwang, W. S.; Lee, J. H.; Lee, J.; Yang, J.; Jung, C.; Kim, H.; Yoo, J. B.; Choi, J. Y.; Jin, Y. W.; Lee, S. Y.; Jena, D.; Choi, W.; Kim, K. High-Mobility and Low-Power Thin-Film Transistors Based on Multilayer Mos2 Crystals. *Nature Communications* 2012, 3, 1011.
122. Yin, Z. Y.; Li, H.; Li, H.; Jiang, L.; Shi, Y. M.; Sun, Y. H.; Lu, G.; Zhang, Q.; Chen, X. D.; Zhang, H. Single-Layer Mos2 Phototransistors. *Acs Nano* 2012, 6, 74-80.
123. Liu, H.; Ye, P. D. D. Mos2 Dual-Gate Mosfet with Atomic-Layer-Deposited Al2o3 as Top-Gate Dielectric. *Ieee Electron Device Letters* 2012, 33, 546-548.

124. Qiu, H.; Pan, L. J.; Yao, Z. N.; Li, J. J.; Shi, Y.; Wang, X. R. Electrical Characterization of Back-Gated Bi-Layer Mos2 Field-Effect Transistors and the Effect of Ambient on Their Performances. *Applied Physics Letters* 2012, 100, 123104.
125. Fuhrer, M. S.; Hone, J. Measurement of Mobility in Dual-Gated Mos2 Transistors. *Nat Nano* 2013, 8, 146-147.
126. Radisavljevic, B.; Kis, A. Mobility Engineering and a Metal-Insulator Transition in Monolayer Mos2. *Nat Mater* 2013, 12, 815-820.
127. Dean, C. R.; Young, A. F.; MericI; LeeC; WangL; SorgenfreiS; WatanabeK; TaniguchiT; KimP; Shepard, K. L.; HoneJ. Boron Nitride Substrates for High-Quality Graphene Electronics. *Nat. Nanotechnol.* 2010, 5, 722-726.
128. Shi, Y.; Zhou, W.; Lu, A.-Y.; Fang, W.; Lee, Y.-H.; Hsu, A. L.; Kim, S. M.; Kim, K. K.; Yang, H. Y.; Li, L.-J.; Idrobo, J.-C.; Kong, J. Van Der Waals Epitaxy of Mos2 Layers Using Graphene as Growth Templates. *Nano Letters* 2012, 12, 2784-2791.
129. Geim, A. K.; Novoselov, K. S. The Rise of Graphene. *Nature Materials* 2007, 6, 183-191.
130. Malard, L. M.; Pimenta, M. A.; Dresselhaus, G.; Dresselhaus, M. S. Raman Spectroscopy in Graphene. *Physics Reports-Review Section of Physics Letters* 2009, 473, 51-87.
131. Das, A.; Pisana, S.; Chakraborty, B.; Piscanec, S.; Saha, S. K.; Waghmare, U. V.; Novoselov, K. S.; Krishnamurthy, H. R.; Geim, A. K.; Ferrari, A. C.; Sood, A. K. Monitoring Dopants by Raman Scattering in an Electrochemically Top-Gated Graphene Transistor. *Nature Nanotechnology* 2008, 3, 210-215.
132. Wang, Q. H.; Jin, Z.; Kim, K. K.; Hilmer, A. J.; Paulus, G. L. C.; Shih, C. J.; Ham, M. H.; Sanchez-Yamagishi, J. D.; Watanabe, K.; Taniguchi, T.; Kong, J.; Jarillo-Herrero, P.; Strano, M. S. Understanding and Controlling the Substrate Effect on Graphene Electron-Transfer Chemistry Via Reactivity Imprint Lithography. *Nature Chemistry* 2012, 4, 724-732.
133. Ferrari, A. C.; Meyer, J. C.; Scardaci, V.; Casiraghi, C.; Lazzeri, M.; Mauri, F.; Piscanec, S.; Jiang, D.; Novoselov, K. S.; Roth, S.; Geim, A. K. Raman Spectrum of Graphene and Graphene Layers. *Physical Review Letters* 2006, 97, 187401.
134. Nair, R. R.; Blake, P.; Grigorenko, A. N.; Novoselov, K. S.; Booth, T. J.; Stauber, T.; Peres, N. M. R.; Geim, A. K. Fine Structure Constant Defines Visual Transparency of Graphene. *Science* 2008, 320, 1308.
135. Bernardi, M.; Palummo, M.; Grossman, J. C. Extraordinary Sunlight Absorption and One Nanometer Thick Photovoltaics Using Two-Dimensional Monolayer Materials. *Nano Letters* 2013, 13, 3664-3670.
136. Zhang, W.; Chuu, C.-P.; Huang, J.-K.; Chen, C.-H.; Tsai, M.-L.; Chang, Y.-H.; Liang, C.-T.; Chen, Y.-Z.; Chueh, Y.-L.; He, J.-H.; Chou, M.-Y.; Li, L.-J. Ultrahigh-Gain Photodetectors Based on Atomically Thin Graphene-Mos2 Heterostructures. *Sci. Rep.* 2014, 4.
137. Liu, W.; Cao, W.; Kang, J.; Banerjee, K. High-Performance Field-Effect-Transistors on Monolayer-Wse2. *ECS Transactions* 2013, 58, 281-285.
138. Son, Y.; Li, M.-Y.; Cheng, C.-C.; Wei, K.-H.; Liu, P.; Wang, Q. H.; Li, L.-J.; Strano, M. S. Observation of Switchable Photoresponse of a Monolayer Wse2–Mos2 Lateral Heterostructure Via Photocurrent Spectral Atomic Force Microscopic Imaging. *Nano. Lett.* 2016.
139. Gao, G.; Gao, W.; Cannuccia, E.; Taha-Tijerina, J.; Balicas, L.; Mathkar, A.; Narayanan, T. N.; Liu, Z.; Gupta, B. K.; Peng, J.; Yin, Y.; Rubio, A.; Ajayan, P. M. Artificially Stacked Atomic Layers: Toward New Van Der Waals Solids. *Nano. Lett.* 2012, 12, 3518-3525.
140. Castellanos-Gomez, A. Black Phosphorus: Narrow Gap, Wide Applications. *The Journal of Physical Chemistry Letters* 2015, 6, 4280-4291.
141. Nishii, T.; Maruyama, Y.; Inabe, T.; Shirotani, I. Proceedings of the International Conference of Science and Technology of Synthetic Metals Synthesis and Characterization of Black Phosphorus Intercalation Compounds. *Synthetic Metals* 1987, 18, 559-564.

142. Ribeiro, H. B.; Pimenta, M. A.; de Matos, C. J. S.; Moreira, R. L.; Rodin, A. S.; Zapata, J. D.; de Souza, E. A. T.; Castro Neto, A. H. Unusual Angular Dependence of the Raman Response in Black Phosphorus. *ACS Nano* 2015, 9, 4270-4276.
143. Wang, X.; Jones, A. M.; Seyler, K. L.; Tran, V.; Jia, Y.; Zhao, H.; Wang, H.; Yang, L.; Xu, X.; Xia, F. Highly Anisotropic and Robust Excitons in Monolayer Black Phosphorus. *Nat. Nanotechnol.* 2015, 10, 517-521.
144. Ge, S.; Li, C.; Zhang, Z.; Zhang, C.; Zhang, Y.; Qiu, J.; Wang, Q.; Liu, J.; Jia, S.; Feng, J.; Sun, D. Dynamical Evolution of Anisotropic Response in Black Phosphorus under Ultrafast Photoexcitation. *Nano. Lett.* 2015, 15, 4650-4656.
145. Low, T.; Roldán, R.; Wang, H.; Xia, F.; Avouris, P.; Moreno, L. M.; Guinea, F. Plasmons and Screening in Monolayer and Multilayer Black Phosphorus. *Phys. Rev. Lett.* 2014, 113, 106802.
146. Luo, Z.; Maassen, J.; Deng, Y.; Du, Y.; Garrelts, R. P.; Lundstrom, M. S.; Ye, P. D.; Xu, X. Anisotropic in-Plane Thermal Conductivity Observed in Few-Layer Black Phosphorus. *Nat Commun* 2015, 6.
147. Engel, M.; Steiner, M.; Avouris, P. Black Phosphorus Photodetector for Multispectral, High-Resolution Imaging. *Nano. Lett.* 2014, 14, 6414-6417.
148. Li, P.; Appelbaum, I. Electrons and Holes in Phosphorene. *Phys. Rev. B* 2014, 90, 115439.
149. Ziletti, A.; Carvalho, A.; Campbell, D. K.; Coker, D. F.; Castro Neto, A. H. Oxygen Defects in Phosphorene. *Phys. Rev. Lett.* 2015, 114, 046801.
150. Liu, D.; Guo, Y.; Fang, L.; Robertson, J. Sulfur Vacancies in Monolayer Mos2 and Its Electrical Contacts. *Appl. Phys. Lett.* 2013, 103, 183113.
151. Yu, Y.; Li, C.; Liu, Y.; Su, L.; Zhang, Y.; Cao, L. Controlled Scalable Synthesis of Uniform, High-Quality Monolayer and Few-Layer Mos2 Films. *Sci. Rep.* 2013, 3.
152. Gurarslan, A.; Yu, Y.; Su, L.; Yu, Y.; Suarez, F.; Yao, S.; Zhu, Y.; Ozturk, M.; Zhang, Y.; Cao, L. Surface-Energy-Assisted Perfect Transfer of Centimeter-Scale Monolayer and Few-Layer Mos2 Films onto Arbitrary Substrates. *ACS Nano* 2014, 8, 11522-11528.
153. Nemes-Incze, P.; Osváth, Z.; Kamarás, K.; Biró, L. P. Anomalies in Thickness Measurements of Graphene and Few Layer Graphite Crystals by Tapping Mode Atomic Force Microscopy. *Carbon* 2008, 46, 1435-1442.
154. Zhang, S.; Yang, J.; Xu, R.; Wang, F.; Li, W.; Ghufran, M.; Zhang, Y.-W.; Yu, Z.; Zhang, G.; Qin, Q.; Lu, Y. Extraordinary Photoluminescence and Strong Temperature/Angle-Dependent Raman Responses in Few-Layer Phosphorene. *ACS Nano* 2014, 8, 9590-9596.
155. Das, S.; Zhang, W.; Demarteau, M.; Hoffmann, A.; Dubey, M.; Roelofs, A. Tunable Transport Gap in Phosphorene. *Nano. Lett.* 2014, 14, 5733-5739.
156. Das, S.; Appenzeller, J. Where Does the Current Flow in Two-Dimensional Layered Systems? *Nano. Lett.* 2013, 13, 3396-3402.
157. Schwierz, F. Graphene Transistors. *Nature Nanotechnology* 2010, 5, 487-496.
158. JuL; Velasco Jr, J.; HuangE; KahnS; NosigliaC; Tsai, H.-Z.; YangW; TaniguchiT; WatanabeK; ZhangY; ZhangG; CrommieM; ZettlA; WangF. Photoinduced Doping in Heterostructures of Graphene and Boron Nitride. *Nat. Nanotechnol.* 2014, 9, 348-352.